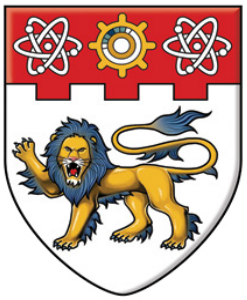

NANYANG TECHNOLOGICAL UNIVERSITY

GNSS Signal Tracking under Weak Signal or High Dynamic Environment

Yang Rong

School of Electrical and Electronic Engineering

2016

GNSS Signal Tracking under Weak Signal or High Dynamic Environment

Yang Rong

School of Electrical and Electronic Engineering

A Thesis Submitted to the Nanyang Technological University in Fulfilment of the Requirements for the Degree of Doctor of Philosophy

Supervised by

Assoc. Prof. LING Keck Voon

2016

Acknowledgments

I would like to express my gratitude to those who have inspired, encouraged, and supported me during my Ph.D study.

Firstly, I would express my deepest gratitude to my supervisor Associate Professor Ling Keck Voon and co-supervisor Associate Professor Poh Eng Kee for their patient guidance and consistent support throughout my research work. Their profound knowledge, solid research skills, patience, and enthusiasm have significant impacts on my research. I am truly grateful to have the opportunity to complete this interesting research work under the guidance of Prof Ling and Prof Poh.

Secondly, I am extremely thankful to Professor Yu Morton of Colorado State University, who has a long-lasting influence on both my research and my personal development. She shares her knowledge, wisdom, and experience with me on my Ph.D study. Without her valuable guidance and kind encouragement, it would be much more difficult for me to finish this academic journey.

Thirdly, I would like to acknowledge my former supervisor, Professor Qin Honglei of Beihang University. I gained my interest in GNSS from a project Prof. Qin guided me during my graduate years, and he alerted and advised me this opportunity to come to Nanyang Technological University.

In addition, my sincere gratitude to Associate Professor Low Kay Soon in Satellite Research Center who offered me the scholarship and allowed me to attend his group meeting. It is a wonderful experience to have so many technical discussions with his team in the meeting. Also, I would like to thank the staff and students in INFINITUS and Satellite Research Center of Nanyang Technological University who have helped me both in study and life in Singapore, including Dr Jin Tian (Beihang University),

Dr Cong Li (Beihang University), Dr Zhu Yunlong (Beihang University), Dr Zhao Yun (Beihang University), Dr Chen Le (Shanghai Jiao Tong University), Dr He Xin, Dr Wu Lin (Huazhong University of Science and Technology), Dr Li Xiang(Huazhong University of Science and Technology), Ms Huang Jiajia, Ms Zhao Ming, Ms Sun Meng, Ms Gao Yumeng, Mr Wang Yang, Mr Liu Yunxiang, Mr Luo Sheng, Mr Zhang Heng, Mr Li Beibei, Mr Wang Wei, Mr Wang Guoming, Mr Hu Hao, Mr Kang Binyin, and Mr Han Bo. Please accept my apology for missing someone out.

Furthermore, a lot of 'Thank You' should be said to my friends, who have given me support and encouragement whenever I needed. The past few years with you have been greatly enjoyable and colorful. They are: Ms Zhou Chi, Ms Zou Yulan, Ms Li Xinyan, Ms Wu Dan, Ms Yu Mengting, Ms Cui Jingjing, Mr Zhou Dexiang, Mr Cheng Tengpeng, Mr Yin Le, Mr Zhang Liangqi, Ms Li Junting, Ms Liu Li, Mr Fang Zhejun, Ms Xiong Siyang, Ms Li Ping, Ms Qi Wenliang, Ms Yang Liwei, Mr Xu Dongyang, Mr Zhu Yanqing, and Mr Wang Yiran.

Most of all, I am grateful to my parents and my grandma, who always support me with their best wishes in my life. Their strong will and optimism encourage me to pursue my dream in academic area. I would not be able to complete my Ph.D degree without their support.

I dedicate this dissertation to the memory of my dearest grandpa, who provided me his unparalleled love throughout his life. I learnt how to be a kind and responsible person from him. I am grateful for his love and kindness forever. I will always remember him in my heart.

Contents

[1]Part of the materials in Chapter 2 are taken from "R. Yang, KV Ling, and EK Poh, *Optimal combination of coherent and non-coherent acquisition of weak GNSS signals*, Pacific PNT, Honolulu, Hawaii, April 2015" and "R. Yang, KV Ling, and EK Poh, *NCO Models for Tracking Loop Design in GNSS Software Receiver*, IEEE/ION PLANS, Monterey, California, May 2014"

[2]Chapter 3 is the phase tracking loop part of our papers "R. Yang, KV Ling, EK Poh, and Y.Morton, *Generalized GNSS Signal Carrier Tracking: Part I: Modelling and Analysis*, accepted by IEEE Transactions on Aerospace and Electronic Systems, January 2017. " and "R. Yang, Y.Morton, KV Ling, and EK Poh, *Generalized GNSS Signal Carrier Tracking: Part II: Optimization and Implementation*, accepted by IEEE Transactions on Aerospace and Electronic Systems, January 2017."

[3]Chapter 4 is the frequency tracking loop part of our papers "R. Yang, KV Ling, EK Poh, and Y.Morton, *Generalized GNSS Signal Carrier Tracking: Part I: Modelling and Analysis*, accepted by IEEE Transactions on Aerospace and Electronic Systems, January 2017. " and "R. Yang, Y.Morton, KV Ling, and EK Poh, *Generalized GNSS Signal Carrier Tracking: Part II: Optimization and*

Implementation, accepted by IEEE Transactions on Aerospace and Electronic Systems, January 2017."

[4]Chapter 5 is simulation part of our paper "R. Yang, Y.Morton, KV Ling, and EK Poh, *Generalized GNSS Signal Carrier Tracking: Part II: Optimization and Implementation*, accepted by IEEE Transactions on Aerospace and Electronic Systems, January 2017"

Summary

There is a growing need to continue operating the Global Navigation Satellite Systems (GNSS) receivers under increasingly challenging and stressful conditions, where signal experiences deep fading, blockage, or high platform dynamics. As the most fragile component of the GNSS receiver, the carrier tracking loop must achieve improved tracking capability. The subject of GNSS tracking loop design has been well studied. This thesis takes the control system design perspective, presents tracking loop design as a state feedback/state estimator framework, sheds insight on frequency domain analysis, derives optimal parameters for carrier tracking loop design, and proposes adaptive tracking solutions for challenging environment.

Two generalized carrier tracking loops, namely, the generalized phase tracking loop and the generalized frequency tracking loop, are studied using this state space framework.

For the generalized phase tracking loop design, three approaches, i.e., proportional integral filter (PIF), Wiener filter (WF), and Kalman filter (KF), are presented in an unified manner from the state feedback/state estimator framework. With the state space framework, analytical equations characterizing the carrier phase tracking loop performance are derived. These equations relate the phase tracking error variance and dynamic stress phase error to the filter design parameters, such as integration time and noise equivalent bandwidth, as well as other parameters, such as thermal noise, oscillator noise, and receiver platform dynamics. From these equations, filter design parameters are optimized under various operating scenarios, such as weak signal or high dynamics. More specifically, the tracking sensitivities of the generalized phase tracking loop with these designs are obtained. Building on this analysis, an

adaptive phase tracking scheme with time-varying integration time or loop bandwidth is proposed.

A similar approach is applied to frequency tracking loop design. The PIF design is mapped to the state space structure through the equivalent closed-loop transfer function. Traditional KF-based frequency tracking loop design assumes white Gaussian noise. However, the frequency error measurement noise is non-white and so analytical equations for the frequency tracking error variance and dynamic stress frequency error are derived, taking into account the non-white noise characteristic. Frequency tracking error variance is used to evaluate the frequency tracking loop performance under the effects of thermal noise, oscillator noise, and platform dynamics. Using these analytical equations, optimal loop parameters are obtained, and the frequency tracking sensitivity is characterized. Based on these theoretical analysis, an adaptive frequency tracking scheme with loop bandwidth is proposed.

Simulation results demonstrate the effectiveness of the proposed adaptive generalized carrier phase/frequency tracking architecture and verify the theoretical prediction.

List of Tables

List of Figures

List of Abbreviations

GNSS	Global Navigation Satellite System
GPS	Global Positioning System
UAV	Unmanned Aerial Vehicle
RF	Radio Frequency
IF	Intermediate Frequency
CDMA	Code division multiple access
BPSK	Binary Phase Shift Keying
EKF	Extended Kalman Filter
MHE	Moving Horizon Estimation
PIF	Proportional Integral Filter
WF	Wiener Filter
KF	Kalman Filter
DLL	Delay Lock Loop
PLL	Phase Lock Loop
FLL	Frequency Lock Loop
VDLL	Vector Delay Lock Loop
VPLL	Vector Phase Lock Loop
VFLL	Vector Frequency Lock Loop
VDFLL	Vector Delay and Frequency Lock Loop
RAIM	Receiver Autonomous Integrity Monitoring
POL	Phase Open Loop
LOS	Line-of-sight
C/A	Coarse/Acquisition

PRN	Pseudo Random Number
DTFT	Discrete Time Fourier Transform
FFT	Fast Fourier transform
IFFT	Inverse Fast Fourier transform
C/N_0	Carrier to Noise Ratio
VCO	Voltage Controlled Oscillator
NCO	Numerically Controlled Oscillator
PSD	Power Spectral Density
DARE	Discrete-time Algebraic Riccati Equation
MLE	Maximum Likelihood Estimation
MMSE	Minimum Mean Squared Error
TCXO	Temperature Compensated Oscillator
OCXO	Oven Compensated Oscillator
LQO	Low Quality Oscillator
HQO	High Quality Oscillator

List of Symbols

Throughout this thesis, bold letters denote vectors and matrices; lower case letters denote the time domain variables and parameters.

τ_k	C/A code delay of the received signal.
φ_k	Initial fractional phase in rad of the received signal.
ω_k	Carrier frequency in rad/s of the received signal.
$\dot{\omega}_k$	Carrier frequency rate in rad/s^2 of the received signal.
$\hat{\tau}_k$	C/A code delay estimation of the local signal.
$\hat{\varphi}_k$	Initial fractional phase estimation of the local signal.
$\hat{\omega}_k$	Carrier frequency estimation of the local signal
$\hat{\dot{\omega}}_k$	Carrier frequency rate estimation of the local signal
T	Coherent integration time in millisecond.
B_n	Tracking loop noise equivalent bandwidth.
w_n	Tracking loop natural frequency.
BN	Phase tracking loop noise equivalent bandwidth.
w_p	Phase tracking loop natural frequency.
BW	Frequency tracking loop noise equivalent bandwidth.
w_f	Frequency tracking loop natural frequency.
$\mathbf{x}$	$n \times 1$ state vector.
$\hat{\mathbf{x}}$	State vector estimation.
$\mathbf{x}^{\mathrm{T}}$	The transpose of vector $\mathbf{x}$.
$\mathbf{A}$	$n \times n$ system transition matrix.
$\mathbf{H}$	$m \times n$ measurement matrix.
$\mathbf{Q}$	$n \times n$ system noise covariance matrix.

$\mathbf{R}$	$m \times m$ measurement noise covariance matrix.
$\mathbf{B}$	$n \times m$ controller operating matrix.
$\mathbf{K}$	$n \times m$ state feedback gain matrix.
$\mathbf{L}$	$n \times m$ state estimator gain matrix.
$\mathbf{P}$	$n \times n$ tracking error covariance matrix.
$\mathbf{A}_P$	System transition matrix in phase tracking loop.
$\mathbf{H}_P$	Measurement matrix in phase tracking loop.
$\mathbf{Q}_P$	System noise covariance matrix in phase tracking loop.
$\mathbf{L}_{PIF}$	Proportional integral filter gain matrix in phase tracking loop.
$\mathbf{L}_{WF}$	Wiener filter gain matrix in phase tracking loop.
$\mathbf{L}_{KF}$	Kalman filter gain matrix in phase tracking loop.
$\mathbf{A}_F$	System transition matrix in frequency tracking loop.
$\mathbf{H}_F$	Measurement matrix in frequency tracking loop.
$\mathbf{Q}_F$	System noise covariance matrix in frequency tracking loop.
$\mathbf{p}_{\bar{\theta}}$	The average phase error variance in phase tracking loop.
$\mathbf{e}_{\bar{\theta}}$	The steady-state dynamic stress phase error in phase tracking loop.
$\mathbf{p}_{\bar{\omega}}$	The average frequency error variance in frequency tracking loop.
$\mathbf{e}_{\bar{\omega}}$	The steady-state dynamic stress frequency error in frequency tracking loop.
σ_{PLL}	1-sigma phase jitter.
σ_{FLL}	1-sigma frequency jitter.

Chapter 1

Introduction

The Global Navigation Satellite Systems (GNSS) commonly include the Global Positioning System (GPS), GLONASS, GALILEO, and Beidou systems. Round-the-clock convenience and global coverage of GNSS has fueled many applications. GNSS receivers are widely equipped in cars, airplanes, and cellphones to provide high accuracy

Table 1.1: Attenuation of different building material [1, 2]

Material	Signal attenuation (dB)
Glass	1-4
Tinted Glass	10
Wood	2-9
Roofing tiles/Bricks	5-31
Concrete	12-43
Reinforced concrete	29-33

location and high precision time synchronization in outdoor or unblocked environment for civilian positioning application. However, in urban areas, forest and indoor environment, GNSS signals are severely attenuated. Table 1.1 [1, 2] presents some indicative attenuation values at the GPS L1 frequency band for some of the most common building materials, where the attenuation can be as much as 30dB. In this case it is impractical for normal GNSS receivers to provide trustworthy positioning solutions. In addition, the receivers also face great challenges in tracking GNSS signals subject to harsh dynamic, such as unmanned aerial vehicles (UAVs), aeronautic/astronautic

aircrafts, where the signal experiences abrupt, random Doppler offsets [3]. These challenging and stressful operating conditions motivates the continuous improvement in receiver's flexibility, sensitivity, and robustness.

1.1 Motivation and Objectives

Section 2.4 surveyed various receiver tracking technologies, such as scalar tracking, vector tracking, and open loop tracking that are commonly used in GNSS receivers. Although the vector tracking and the open loop tracking are more capable, robust, and stable in dealing with high attenuation and high dynamic signals than the scalar carrier tracking loop, these advanced tracking algorithms are very complex for real-time implementations. Thus, a designer may wonder whether it is sufficient to just use the scalar carrier tracking loop design for such demanding application.

When reviewing the traditional carrier tracking loop design, it has been found that three filter design methods, i.e., proportional integral filter (PIF), Wiener filter (WF), and Kalman filter (KF), are most frequently used and investigated. The filter parameters in PIF are selected based on desired tracking loop bandwidth and damping ratio. They are independent of the signal model, therefore, PIF can be considered as a model-free approach. While the filter parameters in WF and KF are determined by the input signal characteristics, they are related to the signal model and can be considered a model-based approach. One may wonder:

> *Is it possible to unify these different designs within a general theoretical framework?*

If yes, the designer could formulate a unified performance objective to compare and optimize these different designs within a general theoretical framework. As it will be elaborated in Chapter 3, under some specific scenarios, the PIF, WF, and KF can be made equivalent. Furthermore, greater performance improvement can be realized through model accuracy rather than the design methods.

In the existing literature, the typical signal model for carrier tracking loop design incorporates the effects of platform dynamics, oscillator noise, and thermal noise. For

model-free design, generally, two main parameters, namely, the filter order and the corresponding coefficients, can be adjusted in carrier tracking loop design. The filter order determines the system's capability in tracking signal dynamics, and the filter coefficients determine the system's tracking accuracy. For example, adjusting the filter coefficients, which changes the damping ratio and noise equivalent bandwidth in a second order PIF, can effectively reduce the influence of thermal noise and oscillator noise in the front-end, but it cannot mitigate the impact of severe fading. Integration time is also an important factor in realizing a discrete time implementation. In the case of weak signal, the integration time in the carrier tracking loop needs to be increased to improve signal detectability. This strategy, however, runs counter to the requirement of tracking high platform dynamics. Besides, as integration time increases, the oscillator noise effect will accumulate which also degrades the carrier tracking performance. These effects are seldom holistically considered in the existing carrier tracking loop designs. In [4], the optimization of integration time selection for a KF-based design was investigated to improve the tracking sensitivity of low dynamic signals. Both the receiver oscillator noise and the thermal noise effects were taken into consideration. However, the analysis did not consider highly dynamic signal fluctuations or receivers equipped with low quality oscillators. Similarly, WF- and PIF-based tracking loops also need to balance these effects in loop designs so as to achieve better tracking performance. Then the challenges for the designer become:

> *What are the optimal design parameters, such as integration time or bandwidth, to balance the effects of platform dynamics, oscillator noise, and thermal noise?*
>
> *What is the tracking limit when the signal is weak and highly dynamic?*

Reference [5] also shows that a well-designed frequency tracking loop will outperform a well-designed phase tracking loop due to rapid phase variation under weak signal and highly dynamic conditions. However, the tracking accuracy of the former is worse than the latter. Hence, we need to investigate

> *In real implementation, how to analyze and use FLL to trade off tracking accuracy against tracking robustness?*

In response to these issues, this thesis attempts to analyse, in detail, the generalized carrier phase and frequency tracking loop designs under diverse operating conditions, such as weak signal or highly dynamic signal environments. We adopt a state space model to characterize the carrier tracking loops for different signal strength, platform dynamics, and receiver oscillator quality. To illustrate the theory, we use the most basic signal and numerically controlled oscillator (NCO) model, and cast the design problem in the state space framework so as to leverage the state space design control techniques to design and optimize the carrier tracking loop parameters. Using this generalized tracking loop architecture, both the phase tracking and frequency tracking can be unified, evaluated, and compared within a common framework. Adopting the minimum mean square error (MMSE) performance criterion, we investigate the optimal solutions and theoretical tracking limits for the phase and frequency tracking loop designs under diverse operating conditions. The state space framework enables in-depth comparative analysis of phase and frequency tracking loop design and optimization.

1.2 Thesis Contributions

The contributions of this thesis are:

1.2.1 State space design framework for carrier tracking loop:

We cast the carrier tracking loop design into a state space design framework and adopted a state feedback/state estimator perspective. Two generalized carrier tracking loops, namely, the generalized phase tracking loop and the generalized frequency tracking loop, are studied using this state space design approach. While this approach has been taken in the KF-based carrier tracking loop design in the past, this thesis gives a control system theoretic perspective and supplements the frequency domain analysis that is typically found in GNSS related literature. Using this generalized tracking loop architecture, we are able to unify the PIF, WF, and KF design methods for phase tracking loop.

By using the state feedback/state estimator methodology to carrier tracking loop design, it is shown that the traditional PIF, WF, and KF designs is a special case of our general design framework. In addition, we applied control system analysis, linking the controllability and stability of the second order tracking loop to single input NCOs, such as rate-only feedback NCO and phase and rate feedback NCO. Such insight is especially useful when higher order NCO model is used, and, in particular, for "multi-input NCO" design where one is no longer limited to just rate or phase and rate feedback NCOs.

1.2.2 Analytical equations for tracking error variance and dynamic stress error:

We derived analytical equations, such as tracking error variance and dynamic stress error, to characterize both the phase and frequency tracking loop performances under various operating conditions. Since the frequency error measurement noise is non-white, this non-white noise characteristic has been taken into account in the analytical derivations, unlike the traditional KF design which assumes white Gaussian noise. These equations relate the phase/frequency tracking error variance and dynamic stress phase/frequency error to the filter design parameters, such as integration time and noise equivalent bandwidth, as well as other parameters, such as thermal noise, oscillator noise, and receiver platform dynamics. Using these equations, we are able to compare and evaluate the performance of the PIF, WF, and KF designs in the generalized phase tracking loop according to an unified performance assessment and we are also able to compare and evaluate the performance in both the generalized phase tracking loop and generalized frequency tracking loop within the general theoretical framework.

1.2.3 Optimization of tracking loop parameters:

We optimized the filter design parameters, such as the optimal integration time and the optimal noise equivalent bandwidth, to minimize the mean square error

in generalized phase and frequency tracking loops under various operating conditions. The corresponding theoretical tracking sensitivity limits in generalized phase and frequency tracking loops for data and pilot channels are respectively obtained based on the 3-sigma rule. We demonstrated that if a 2-state model is used, the optimized PIF, WF, and KF can be tuned equivalently, whereas if a 3-state model is used, the optimized WF and KF are equivalent and slightly better than the optimized PIF.

1.2.4 Adaptive phase and frequency tracking schemes:

The idea of adaptive tracking has been suggested in the literature but it is limited to adjusting the filter gain(loop parameters). We proposed an adaptive phase tracking scheme with varying integration time and loop parameters and an adaptive frequency tracking scheme with varying loop parameters to track weak and highly dynamic signals. The schemes assume a prior known maximum line-of-sight(LOS) jerk. We validated the adaptive phase and frequency tracking schemes through simulations with high receiver platform dynamics and low signal power. We demonstrated that the proposed adaptive phase tracking scheme outperforms the traditional phase lock loop (PLL) and the adaptive frequency tracking scheme outperforms the traditional KF-based frequency lock loop (FLL).

1.3 Thesis Outline

The rest of the thesis is organized as follows:

Chapter 2 reviews the background of GNSS signal structure, baseband processing in GNSS software receivers, the state-of-art of the GNSS tracking technologies, and the state space feedback/state estimator design process in control theory. This chapter provides the basics of GNSS signal acquisition and tracking process. It also introduces conventional design and implementation of the baseband signal processing. Next, the current carrier tracking technologies, such as the scalar carrier tracking, the vector

tracking, and open loop tracking for highly dynamics and weak signals are reviewed. Finally, the state space design process in control theory is included in this chapter, laying the foundation of its application for subsequent GNSS carrier tracking loop design.

Chapter 3 provides a state space framework for phase tracking loop design. The state feedback/state estimator design approach is adopted. The selection of suitable plant models and the design of the state feedback gain matrices using PIF, WF, and KF are studied. Closed-form expressions of tracking accuracy, including phase tracking error variance and dynamic stress error in the presence of thermal noise, oscillator effects, and receiver platform dynamics are derived. Subsequently, the optimization of three different design approaches under the MMSE criteria is discussed. The theoretical tracking sensitivity analysis for these tracking loops is provided and the optimal values of the loop parameters are derived accordingly. Finally, an adaptive phase tracking scheme which adjusts the integration time and filter parameters to provide optimal performance is proposed.

Chapter 4 outlines the state space design approach for design of the generalized frequency tracking loop. Analytical equations for the frequency tracking error variance and dynamic stress frequency error are derived, taking into account the non-white noise characteristic, unlike the traditional KF design which assumes white Gaussian noise. Subsequently, optimal solutions of loop parameters under the MMSE criterion and tracking sensitivity with respect to 3-sigma rule are obtained. Following on the theoretical analysis, an adaptive frequency tracking scheme which adjusts the filter parameters to provide optimal performance is proposed.

Chapter 5 presents the tracking results of simulated signal from Spirent simulator for the phase and frequency tracking loop designs. The simulated dynamic signals with nominal strength are sampled by a low cost low oscillator quality front-end, and then used to validate the theoretical prediction of dynamic stress error and tracking accuracy for both phase and frequency tracking loops. Then two case studies under the scenarios of weak static signal sampled by a front-end with high quality oscillator (HQO), and highly dynamic weak signal sampled by a front-end with low quality oscillator (LQO), validated the systematic design of optimized loop parameters and

the adaptive phase and frequency tracking schemes. The comparison between the adaptive phase/frequency tracking loop and the existing traditional PLL/FLL is provided. The superiority of the adaptive phase/frequency tracking loop with optimal design validated the effectiveness of the theoretical analysis.

Finally, Chapter 6 concludes this thesis and proposes future research work.

Chapter 2

Review of GNSS signals and tracking technologies [1]

2.1 Introduction

This chapter reviews some fundamental techniques in GNSS receivers. First, the GNSS signal background is presented. After that, the typical baseband processing of GNSS receivers is introduced. Then, the review of current carrier tracking technologies for high dynamics and weak signals is presented. Finally, the typical control system design process is studied as the theoretical foundation for the following GNSS carrier tracking loop design.

2.2 GNSS signal background

GNSS is a direct sequence spread spectrum system, where the pseudo random noise (PRN) codes with good auto-/cross-correlation characteristics are modulated on the carrier waves to spread the navigation data for each satellite. Currently, GPS broadcasts three navigational signals in L1 (1575.42 MHz), L2 (1227.60 MHz), and L5

[1]Part of the materials in Chapter 2 are taken from "R. Yang, KV Ling, and EK Poh, *Optimal combination of coherent and non-coherent acquisition of weak GNSS signals*, Pacific PNT, Honolulu, Hawaii, April 2015" and "R. Yang, KV Ling, and EK Poh, *NCO Models for Tracking Loop Design in GNSS Software Receiver*, IEEE/ION PLANS, Monterey, California, May 2014"

(1176.45 MHz) [6]. Two types of PRN codes are modulated in the GPS signals, namely Coarse Acquisition (C/A) Code and Precision (P) code, for civilian and military applications, respectively.

In this work, GPS L1 signal using C/A code will be discussed as a case study for carrier tracking loop modelling and design. The theoretical analysis and design approaches can be easily applied in the other navigation signals, such as, GPS L2, L5 and Beidou B1 signals. In GNSS receivers, satellite signals are normally received through the use of a right-hand circularly polarized (RHCP) antenna and amplified using a low-noise amplifier (LNA), then downconverted to an intermediate frequency (IF) in radio frequency (RF) front-end for GNSS software processing. The received IF signal can be written as

$$r(t) = \sum_{i \in S_{sig}} s^i(t) + n(t). \tag{2.1}$$

where S_{sig} is the set of satellite signals in view, $s^i(t)$ denotes the received signal from the i^{th} satellite and $n(t)$ denotes the additive receiver thermal noise. Since the satellite signals are received by the same receiver, we assume that the noise for different channels are identical. The received signal broadcast by the i^{th} satellite can be written as

$$s^i(t) = \sqrt{\frac{C^i}{2}} d^i\left(t - \tau^i\right) c^i\left(t - \tau^i\right) \cos\left(\left(\omega_{IF} + \omega_d^i\right) t + \varphi^i\right) \tag{2.2}$$

where C^i is the received i^{th} satellite signal power and the functions $d^i(t - \tau^i)$ and $c^i(t - \tau^i)$ represent the data sequence and C/A code sequence, delayed by time τ^i, respectively. $\omega_{IF} = 2\pi f_{IF}$, $\omega_d^i = 2\pi f_d^i$, where f_{IF}, f_d^i, and φ^i represent the IF frequency, Doppler frequency, and carrier phase of i^{th} satellite signal, respectively. The noise $n(t)$ is assumed to be a zero-mean additive white Gaussian noise, with noise power $\sigma^2 = B_{IF} N_0/2$ [7], where B_{IF} is the two-sided IF filter bandwidth, approximately equals to the sampling frequency f_s and $N_0/2$ is the two-sided noise power spectrum density (PSD) [7].

2.3 Baseband Processing in GNSS Receiver

The fundamental of the baseband processing in GNSS receivers are that of signal acquisition and tracking. The signal acquisition operation provides a coarse estimation of C/A code delay and Doppler frequency for each visible satellite signal in the two-dimensional search area. These signal estimations are used to initiate the tracking process. When delay lock loop (DLL) and PLL are locked, the code shift (pseudorange) and phase measurements are obtained. Then the C/A code sequence and carrier wave can be wiped off from the signal for the navigation data decoding. By using the measurements and the data bits, the receiver calculates the positioning results.

2.3.1 Acquisition

Acquisition process detects the absence or presence of each satellite signals in the two-dimensional searching area as shown in Fig.2.1. A typical range of frequency is ± 10 kHz and code delay 1023 chips (or in samples within 1ms code period) for 32 GPS satellites are covered to search for the visible satellite signals [8, 9].

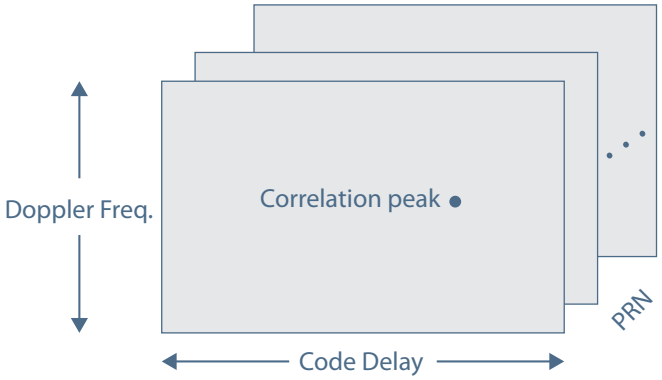

Figure 2.1: Software GNSS receiver acquisition searching area.

In weak signal environment, when the signal to noise ratio (SNR) requirement (typically -19dB) cannot be satisfied by the inherent spread spectrum gain for signal detection, the integration time in acquisition procedure has to be expanded in

order to achieve the desirable detection SNR. Coherent integration technique [8–10], which represents the integration between the received signal and the local signal replica, produces the best performance in the absence of data bit transition and carrier phase error. However, in a weak signal environment, the required integration time is generally in multiples of one data bit interval (20ms for GPS) and any resulting bit transitions will lead to a significant SNR loss. In addition, due to the ambiguity function characteristics, the Doppler search step should be decreased when coherent integration time increases. Hence, the length of the coherent integration time is limited due to the computational burden and data bit transition consideration. These restrictions severely limit the effectiveness of coherent integration for a weak signal acquisition. To address this issue, the non-coherent integration technique [7, 10], which uses the sum of the squares of the signal, reduces the influence of bit transition and inaccurate carrier phase. However, this square operation amplifies the noise and introduces the so-called squaring loss. Note that the squaring loss increases as non-coherent integration time increases. To overcome these limitations, various algorithms, such as the combination of coherent and non-coherent integration [7], the differential integration [7, 11, 12], and the double differential integration [13], were adopted in a weak signal acquisition.

In a highly dynamic signal environment, one of the biggest challenges in acquisition is the computational complexity. Many works have been done on decreasing the computational load, using techniques such as the code domain parallel with inverse FFT approach [8, 9] and signal down sampling in frequency domain method [14].

At present, the combination of coherent and non-coherent acquisition technique is widely used in real implementation. Fig. 2.2 shows the block diagram of the coherent and non-coherent combing acquisition.

Assuming coherent integration time T is N times code period T_c (1ms for GPS L1 C/A code), the k^{th} coherent integration result after the correlation with the local

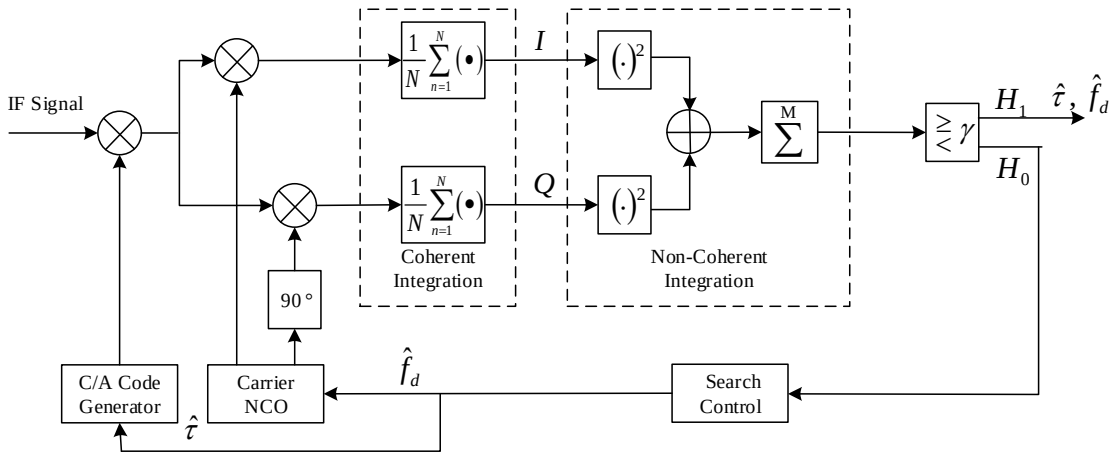

Figure 2.2: The architecture of coherent and non-coherent combining acquisition.

signal replica can be written as:

$$Y_k = \frac{\exp(j\varphi)}{N} \sum_{l=1}^{N} d_l(t-\tau) \sqrt{\frac{C}{2}} \frac{1}{T_c} \int_0^{T_c} c(t-\tau)(t-\hat{\tau}) \exp\left(j2\pi\left(f_d - \hat{f}_d\right)\right) dt + \tilde{n}_Y(t) \tag{2.3}$$

where $\hat{\tau}$ and $\hat{f}_d$ represent the local estimation of code delay and Doppler frequency. $\tilde{n}_Y(t)$ is the white Gaussian noise of the correlation result with the variance

$$\sigma_Y^2 = \frac{\sigma^2}{2N} = \frac{N_0}{4NT_c}. \tag{2.4}$$

Then the non-coherent integration operation sums the signal energy for M times as

$$D = \sum_{k=1}^{M} E^2[\mathrm{Re}(Y_k)] + E^2[\mathrm{Im}(Y_k)]. \tag{2.5}$$

The normalised form of detection variable for the combination of coherent and non-coherent acquisition can be written as:

$$\bar{D} = \frac{D}{\sigma_Y^2} \tag{2.6}$$

Under the null hypothesis H_0 that the signal is absent or the alternative hypothesis H_1 that the signal is present, the detection variable $\bar{D}$ obeys central or non-central χ^2 distribution [7, 15]. The χ^2 distribution parameter can be expressed as:

$$\lambda_M = \sum_{k=1}^{M} \frac{E^2\left[Re\left(Y_k\right)\right] + E^2\left[Im\left(Y_k\right)\right]}{\sigma_Y^2} \approx 2MNT_c\frac{C}{N_0}. \tag{2.7}$$

It is noted that λ_M represents the output SNR and the values of N and M can be increased and adjusted to compensate the power loss when the signal is weak.

Given the threshold γ, the false alarm probability and detection probability of N ms coherent integration combining M times non-coherent accumulation acquisition can be found as [7, 15]:

$$P_{fa}(\gamma) = P(\bar{D} > \gamma|H_0) = \exp\left(-\frac{\gamma}{2}\right)\sum_{i=0}^{M-1}\frac{1}{i!}\left(\frac{\gamma}{2}\right)^i \tag{2.8}$$

$$P_d(\gamma) = P(\bar{D} > \gamma|H_1) = Q_M\left(\sqrt{\lambda_M},\ \sqrt{\gamma}\right) \tag{2.9}$$

where $Q_M(\ \cdot,\ \cdot)$ is the generalized Marcum Q function.

In the real implementation, the value of threshold γ is obtained by the given false alarm probabilities, such as 10^{-5} and 10^{-3} [15]. As the examples shown in Fig.2.3 and 2.4, the signal is detected as present or absent according to whether the detection variable passes the threshold or not with 10^{-3} false alarm probability. Finally, the estimations of code delay and Doppler frequency can be obtained from the successful peak cell for the subsequent tracking process. Several issues should be considered in the real implementation to improve the acquisition performance: a) non-coherent doesnt recover the carrier phase only Doppler, b) data bit transitions can be handled many different ways (e.g. removal as most bits are known, or can do bit guessing, etc.), c) sensitivity to cross correlation especially when tracking both weak and strong signals, non-coherent has a much larger bandwidth which results in much larger cross correlation error, d) computational load: e.g. size of coherent vs non-coherent FFT.

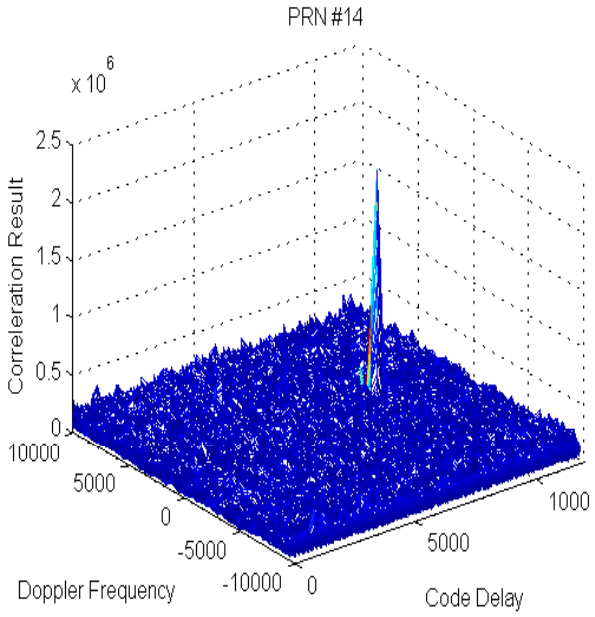

Figure 2.3: Coherent($N = 1$) and non-coherent($M = 1$) combining acquisition result of PRN 14 satellite signal at $C/N_0 = 43$dB-Hz (acquired).

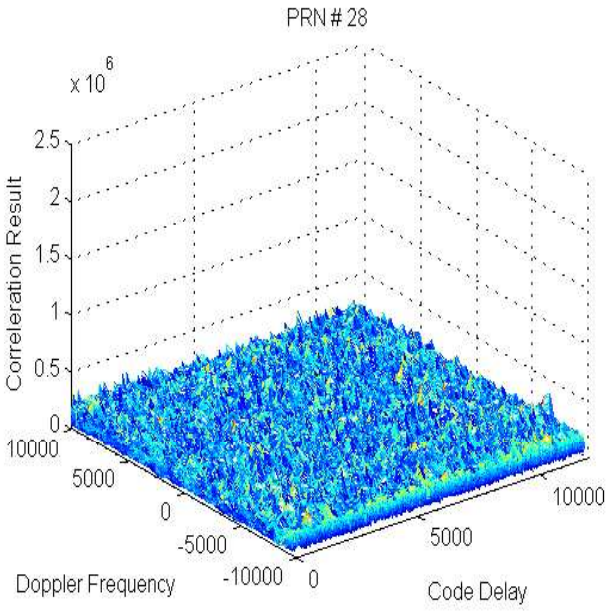

Figure 2.4: Coherent($N = 1$) and non-coherent($M = 1$) combining acquisition result of PRN 28 satellite signal (not acquired).

2.3.2 Tracking

The traditional GNSS tracking loop is designed to provide the local replica with accurate code phase, carrier phase and carrier frequency, to wipe off the C/A code and carrier wave in order to obtain the navigation data. A typical GNSS tracking loop consists of a DLL for code tracking and a PLL for carrier tracking. Fig. 2.5 illustrates typical baseband code and carrier tracking loops for one receiver channel in the closed loop mode of operation.

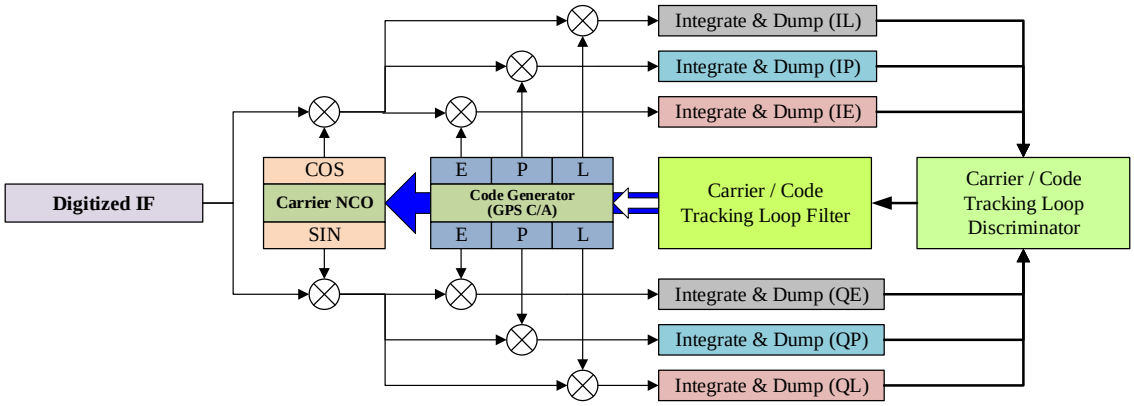

Figure 2.5: Generic GNSS code and carrier tracking loops block diagram.

Both the code and carrier tracking loops share the same loop architecture which typically contains a loop discriminator, a loop filter and a voltage controlled oscillator (VCO) [8, 9] as shown in Fig. 2.6.

The loop discriminator generates the error signal ε between the loop input V_{in} and output V_{out}. The loop filter is used to reduce the in-band noise so as to produce an accurate estimate of the original signal at its output. Based on the filtered error signal, VCO updates the local generated signal V_{out} to follow the input signal V_{in}.

Discriminator output ε

Both the code and carrier discriminators utilize the correlation results between the local replica and the received signal to obtain their corresponding estimation errors. The dump and integration branches of the early code, late code, and prompt code

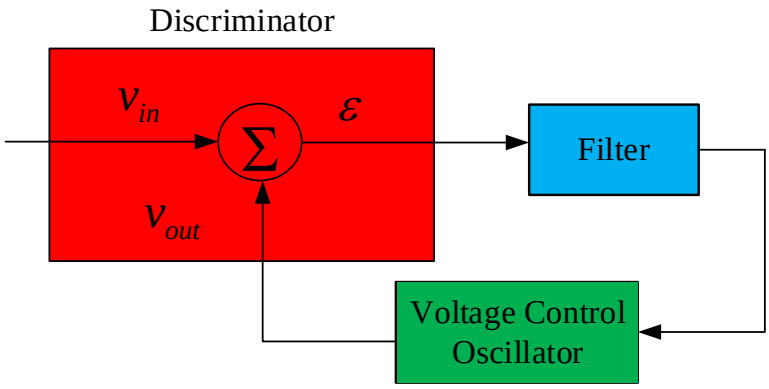

Figure 2.6: Generic analog phase lock loop block diagram.

with the in-phase and quadrature carriers at the k^{th} epoch can be written as [16]:

$$I_{Pk} = d_k\sqrt{\frac{C}{2}}sinc\left(\frac{\Delta\omega_k T}{2}\right)R\left(\Delta\tau_k\right)\sin\left(\Delta\omega_k\frac{T}{2}+\Delta\varphi_k\right)+n_{Pk}^{I} \tag{2.10}$$

$$Q_{Pk} = d_k\sqrt{\frac{C}{2}}sinc\left(\frac{\Delta\omega_k T}{2}\right)R\left(\Delta\tau_k\right)\cos\left(\Delta\omega_k\frac{T}{2}+\Delta\varphi_k\right)+n_{Pk}^{Q} \tag{2.11}$$

$$I_{Ek} = d_k\sqrt{\frac{C}{2}}sinc\left(\frac{\Delta\omega_k T}{2}\right)R\left(\Delta\tau_k-\frac{\delta}{2}\right)\sin\left(\Delta\omega_k\frac{T}{2}+\Delta\varphi_k\right)+n_{Ek}^{I} \tag{2.12}$$

$$Q_{Ek} = d_k\sqrt{\frac{C}{2}}sinc\left(\frac{\Delta\omega_k T}{2}\right)R\left(\Delta\tau_k-\frac{\delta}{2}\right)\cos\left(\Delta\omega_k\frac{T}{2}+\Delta\varphi_k\right)+n_{Ek}^{Q} \tag{2.13}$$

$$I_{Lk} = d_k\sqrt{\frac{C}{2}}sinc\left(\frac{\Delta\omega_k T}{2}\right)R\left(\Delta\tau_k+\frac{\delta}{2}\right)\sin\left(\Delta\omega_k\frac{T}{2}+\Delta\varphi_k\right)+n_{Lk}^{I} \tag{2.14}$$

$$Q_{Lk} = d_k \sqrt{\frac{C}{2}} sinc\left(\frac{\Delta\omega_k T}{2}\right) R\left(\Delta\tau_k + \frac{\delta}{2}\right) \cos\left(\Delta\omega_k \frac{T}{2} + \Delta\varphi_k\right) + n_{Lk}^{Q} \qquad (2.15)$$

where $\Delta\tau_k = \tau_k - \hat{\tau}_k$, $\Delta\omega_k = \omega_k - \hat{\omega}_k$, and $\Delta\varphi_k = \varphi_k - \hat{\varphi}_k$ represent the errors between the received signals and the local replicas. δ is the early-late spacing (typically 1 code chip), and n_{Pk}^{I}, n_{Pk}^{Q}, n_{Ek}^{I}, n_{Ek}^{Q}, n_{Lk}^{I}, and n_{Lk}^{Q} are the correlation result between the white Gaussian noise and the local replicas with the variance as in equation (2.4) [16].

In the code tracking loop, the output of the normalized noncoherent early minus late envelope discriminator can be obtained as [8, 17]:

$$\Delta\tau_k = \frac{1}{2} \frac{\sqrt{I_{Ek}^2 + Q_{Ek}^2} - \sqrt{I_{Lk}^2 + Q_{Lk}^2}}{\sqrt{I_{Ek}^2 + Q_{Ek}^2} + \sqrt{I_{Lk}^2 + Q_{Lk}^2}} \approx \Delta\bar{\tau}_k + \eta_k \qquad (2.16)$$

where $\Delta\bar{\tau}_k$ is actual code delay estimation error, η_k is the equivalent code error noise with variance [8, 17]

$$\sigma_\eta^2 = \frac{1}{4TC/N_0}\left(1 + \frac{1}{4TC/N_0}\right), \qquad (2.17)$$

and C/N_0 is the carrier to noise ratio (the typical value of C/N_0 for nominal signal strength is above 40 dB-Hz).

In the carrier tracking loop, the output of the arctangent carrier phase discriminator is: [8, 17]:

$$\Delta\theta_k = \arctan\left(\frac{Q_{Pk}}{I_{Pk}}\right) \approx \Delta\bar{\theta}_k + v_k. \qquad (2.18)$$

where $\Delta\bar{\theta}_k$ denotes the actual average phase error and v_k represents the equivalent phase error noise with variance [18, 19]

$$\sigma_v^2 = \frac{1}{2TC/N_0}\left(1 + \frac{1}{2TC/N_0}\right) \qquad (2.19)$$

Filter Design

PIF is commonly used in the traditional tracking loop design [8, 9]. Generally, two main parameters, namely, the filter order and the corresponding coefficients, can be

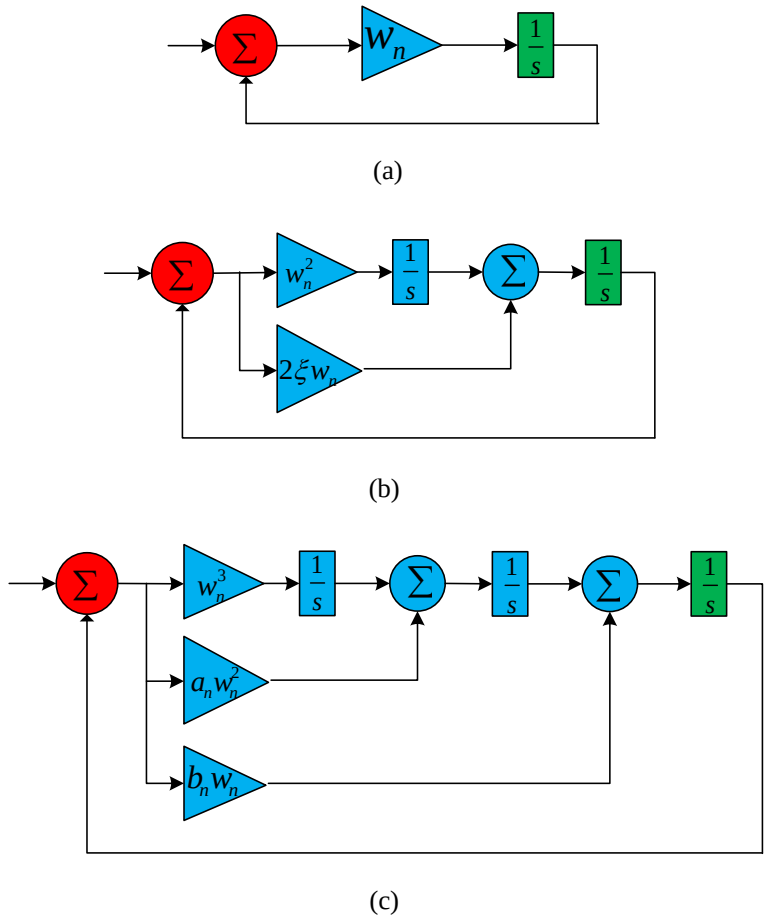

Figure 2.7: Block diagrams of: (a) first-, (b) second-, and (c) third-order analog PLLs.

adjusted in the filter design. The filter order determines the system's capability in tracking signal dynamics [8,9], and the first-, second-, and third-order loops are usually employed to process signals under static, constant velocity dynamic and constant acceleration dynamic environments, respectively. Fig.2.7 shows the implementation of Fig.2.6 with three types of PIF [8].

The three loop filters in Fig.2.7 can be written as:

$$F_1(s) = w_n \tag{2.20}$$

$$F_2(s) = 2\xi w_n + \frac{w_n^2}{s} \tag{2.21}$$

Table 2.1: Loop Filter Characteristics

Loop order	Noise bandwidth B_n(Hz)	Typical values
First	$\frac{w_n}{4}$	$B_n = 0.25w_n$
Second	$\frac{w_n\left(1+\xi^2\right)}{4\xi}$	ξ=0.707 $B_n \approx 0.53w_n$
Third	$\frac{w_n\left(a_n b_n^2+a_n^2-b_n\right)}{4(a_n b_n-1)}$	$a_n = 1.1$ $b_n = 2.4$ $B_n \approx 0.7845w_n$

$$F_3(s) = b_n w_n + \frac{a_n w_n^2}{s} + \frac{w_n^3}{s^2} \tag{2.22}$$

in $s-$domain [8]. Moreover, in the traditional continuous-time tracking loop design, VCO in the feedback path of the tracking loop in Fig. 2.7, is modeled as an integrator with the transfer function as [8]:

$$V(s) = \frac{1}{s} \tag{2.23}$$

Therefore, the closed-loop transfer functions for the first-, second-, and third-order analog PLLs can be obtained as:

$$H_{PIF1}(s) = \frac{w_n}{s + w_n} \tag{2.24}$$

$$H_{PIF2}(s) = \frac{2\xi w_n s + w_n^2}{s^2 + 2\xi w_n s + w_n^2} \tag{2.25}$$

$$H_{PIF3}(s) = \frac{b_n w_n s^2 + a_n w_n^2 s + w_n^3}{s^3 + b_n w_n s^2 + a_n w_n^2 s + w_n^3} \tag{2.26}$$

Their loop parameters can be obtained by the predefined values of damping ratio ξ and noise equivalent bandwidth B_n, as listed in Table 2.1 [8], where w_n is the natural frequency.

The typical methodology to design the loop filter is based on discretization of an analog PLL [8, 9] since the theoretical and practical aspects of continuous-time PLL and its performance in different situations are well developed. The commonly used transformation formulas from s-domain to z-domain are bilinear ($s = \frac{2}{T}\frac{1-z^{-1}}{1+z^{-1}}$), forward Euler ($s = \frac{1-z^{-1}}{Tz^{-1}}$), and backward Euler ($s = \frac{1-z^{-1}}{T}$) transformations.

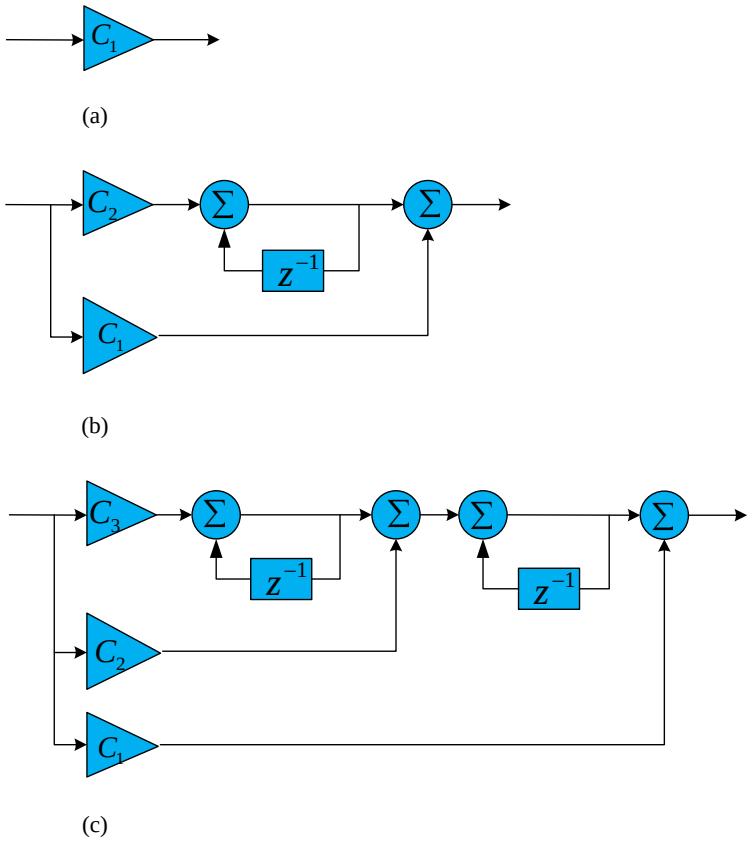

Figure 2.8: Block diagrams of discrete loop filters in (a) first-, (b) second-, and (c) third-order PLLs.

In modern realization of software receivers, the analog PIF is digitized and VCO is replaced by a numerical control oscillator (NCO) as shown in Fig. 2.8. Through forward Euler transformation $s = (z-1)/T$ (valid only for $B_n \cdot T \ll 1/2$ [20]), the discrete PIFs [9] can be written as [9, 21]:

$$F_1(z) = C_1 \tag{2.27}$$

$$F_2(z) = C_1 + \frac{C_2}{1 - z^{-1}} \tag{2.28}$$

$$F_3(z) = C_1 + \frac{C_2}{1 - z^{-1}} + \frac{C_3}{(1 - z^{-1})^2} \tag{2.29}$$

and VCO is digitized as a discrete-time integrator with [9]

$$V(z) = \frac{Tz^{-1}}{1 - z^{-1}} \tag{2.30}$$

The closed-loop transfer functions for the first-, second-, and third-order discrete PLLs can be obtained as

$$H_1(z) = \frac{C_1 T}{z + C_1 T - 1} \tag{2.31}$$

$$H_2(z) = \frac{C_1 T z - (C_1 - C_2)T}{z^2 + (C_1 T - 2)z - (C_1 - C_2)T + 1} \tag{2.32}$$

$$H_3(z) = \frac{C_1 T z^2 + (C_2 T - 2C_1 T)z - C_2 T + C_3 T + C_1 T}{z^3 + (C_1 T - 3)z^2 + (-2C_1 T + C_2 T + 3)z - C_2 T + C_3 T + C_1 T - 1} \tag{2.33}$$

We discretize equations (2.24), (2.25), and (2.26) from the s-domain to the z-domain:

$$H_{PIF1}(z) = \frac{w_n T}{z + w_n T - 1} \tag{2.34}$$

$$H_{PIF2}(z) = \frac{2\xi w_n T z + w_n^2 T^2 - 2\xi w_n T}{z^2 + (2\xi w_n T - 2)\, z + (w_n^2 T^2 - 2\xi w_n T + 1)} \tag{2.35}$$

$$H_{PIF3}(z) = \frac{(b_n w_n T)\, z^2 + \left(a_n w_n^2 T^2 - 2b_n w_n T\right) z + \left(w_n^3 T^3 - a_n w_n^2 T^2 + b_n w_n T\right)}{z^3 + (b_n w_n T - 3)\, z^2 + (a_n w_n^2 T^2 - 2b_n w_n T + 3)\, z + (w_n^3 T^3 - a_n w_n^2 T^2 + b_n w_n T - 1)} \tag{2.36}$$

Comparing equations (2.31), (2.32), and (2.33) with equations (2.34), (2.35), and (2.36), the expressions of the discrete PIFs' parameters are:

$$first\ \ order : C_1 = w_n \tag{2.37}$$

$$\begin{aligned} second\ \ order : C_1 &= 2\xi w_n \\ C_2 &= w_n^2 T \end{aligned} \tag{2.38}$$

$$\begin{aligned} third\ \ order : C_1 &= b_n w_n \\ C_2 &= a_n w_n^2 T \\ C_3 &= w_n^3 T^2 \end{aligned} \tag{2.39}$$

Feedback process in NCO

Given the filtered tracking errors, i.e., the code delay estimation error in DLL and the carrier phase estimation error in PLL, NCOs update the local estimations to generate C/A code and carrier signals in the new epoch. Typically, the code delay, instead of code frequency, is adjusted in DLL since the C/A code frequency is nearly constant and less affected by the receiver dynamics than the carrier signal. More importantly, the code delay estimation accuracy ultimately determines the positioning performance. The carrier signal updates of NCO in PLL is completely different from that in DLL since the carrier signal is much more sensitive to the receiver dynamics than C/A code. The local generated carrier signal has the form of $\omega_d t + \varphi$ that contains Doppler frequency ω_d and initial phase φ in every interval. The locally generated signal is obviously not an exact copy of the incoming signal. The strategies that update frequency only or phase only or both the frequency and phase will result in different carrier tracking performance.

As mentioned above, VCO is usually modeled as an integrator and digitized as a discrete NCO through forward Euler transformation [9,21]. The other two transformations, i.e., the backward [18,22] and bilinear [8], also have been used in the discretization procedure. The different transformation may lead to different implementation of the feedback operation in NCO. J.B.Thomas has divided NCO models into two broad categories: the rate-only feedback NCO, and the phase and rate feedback NCO [23, 24]. The analysis indicates that the bilinear transformation is equivalent to the rate-only feedback NCO [23, 24] and backward Euler is equivalent to the phase and rate feedback NCO [20].

In a loop with rate-only feedback NCO, the NCO rate register is updated at the end of the previous accumulation with a value equivalent to the present rate estimate. NCO phase register is left untouched so that NCO phase is continuous from interval to interval [23]. In a loop with phase and phase-rate feedback NCO, the phase is updated by using the phase change from the filter output. The rate register of the NCO is initialized with a rate value equivalent to the phase change and the phase register with a phase value equal to model phase minus one half interval of NCO phase change [23]. These two NCOs can be implemented as single input-NCOs in hardware. In-depth analysis shows that phase and phase rate feedback NCO will usually be discontinuous at the update point because the initial phase at each interval is calculated by propagating the average generated phase of the interval backward.

The above tracking technologies are most frequently used in GNSS receivers. The

improved design and analysis of this conventional tracking loop as well as other advanced tracking methods will be reviewed next.

2.4 Receiver Tracking Technologies

As the most fragile component of a GNSS receiver, the carrier tracking loop ultimately determines the overall receiver performance. Carrier signal tracking under the challenging and stressful environments, where the signal experiences deep fading, blockage, and high platform dynamics, has received much attention in recent years [25]. Various tracking techniques, e.g., the scalar tracking, the vector tracking, and the open loop tracking, have been used and designed to cope with the technical challenges.

2.4.1 Scalar Tracking

In scalar tracking loop, each satellite signal is independently processed by a closed-loop tracking system. Typically, three tracking approaches: PLL (as presented in Section 2.3), FLL, and FLL-assisted-PLL are used to track the carrier phase and carrier frequency [8, 9, 18, 23, 26] in GNSS software receiver.

I. Phase locked loop

PLL is the most widely adopted approach in GNSS receivers since the phase discriminator characteristics and loop filter design are well investigated over the past few decades . Coherent phase discriminators were initially used to obtain the phase error signal [8]. Then non-coherent discriminators were adopted for a weak GNSS signal tracking to avoid the power loss due to the navigation data transition. A maximum likelihood (ML) phase estimator in the non-coherent tracking architecture was proposed in [27] and a non-coherent phase memory discriminator for integration time extension was proposed in [28]. Given the phase error from the above phase discriminators, the corresponding filter designs have been discussed in many literature as well. PIF, WF, and KF, are commonly used in the existing literature.

The PIF design follows the transformation of an appropriate continuous-time (s-domain), analog filter to its corresponding z-domain representation in discrete-time [8, 9]. The PIF-based, digital PLL tracking error analysis in the presence of thermal noise, oscillator noise,

and dynamic stress was presented in [19]. A major limitation of the PIF-based design is that the s-domain to z-domain transformation is only valid when $B_n \cdot T \ll 1/2$. This constraint limits its application in a weak signal and highly dynamic signal processing because a long integration time and a wide bandwidth are required when the signal is weak and highly dynamic. To overcome this limitation, an alternative approach, which directly designs the loop filter in z-domain based on the discrete-time input carrier phase, was proposed in [20, 26, 28]. The well-known, controlled-root method to determine the filter parameters in a digital PLL was first proposed in [23] and subsequently employed in [20] and [28] for GNSS carrier tracking loop design. Reference [26] provides the stability ranges of the discrete-time filter parameters and the corresponding tracking error variance. However, it did not consider the oscillator noise effect, which can not be neglected under weak signal conditions. In [29–31], the PIF-based PLL is transformed into a state space tracking loop architecture for comparison with the KF-based tracking loop. *However, the theoretical tracking accuracy of the resulting state space tracking loop architecture was not investigated.*

The WF-based approach is based on the MMSE criteria [32]. It separates the input signal from noise in the frequency domain and is known to have better tracking accuracy than the PIF design [32]. Hence, it has been widely used in GNSS tracking loop applications [16,18,33]. References [16,18] proposed WF filter that tracks carrier signals with thermal and oscillator noises only under static condition. This limitation was addressed in [33] which developed a WF that separated carrier phase dynamics from thermal noise but without including the oscillator noise effects.

Being the optimal filter for unbiased white Gaussian noise in linear systems, KF is widely adopted in phase tracking loop implementations [4, 29–31, 34, 35]. The signal models used in the KF technique consist of a state space model and a measurement model. The state space model represents the signal of a dynamic process driven by system noise, whereas the measurement model depicts measurements corrupted by thermal noise. There are two typical state space models, namely the error state model and the direct state model, which have both been used in KF-based PLL design [31]. PLLs based on these two models are equivalent and share the same architecture with the PIF-based PLL [29,31]. By using these models, KF is able to provide the optimal estimates of an input signal corrupted by a white Gaussian noise.

Various efforts have been made to optimize these filters to improve tracking loop performance under weak signal environments [18, 19, 34, 36, 37] or for receivers on highly dynamic platforms [38–43], or in environments where both weak signals and highly dynamics exist [44, 45]. For the PIF-based tracking loop, an optimal bandwidth can be found by adjusting the filter coefficients with a specified value of C/N_0 [46, 47]. In [46], an adaptive bandwidth PLL was proposed, which, through comparing the discriminator output with a predefined threshold, allows the system to automatically calculate the optimal loop bandwidth. In order to avoid the computational burden in real time calculation, Reference [47] provides a look up table according to the input C/N_0 and some pre-defined platform dynamics (jerk dynamic stress ranging from 0.1 g/s to 1 g/s). In [48] and [49], adaptive KF tracking method has been proposed. It adjusts the KF gains according to C/N_0 or the equivalent noise bandwidth. Reference [4] investigated the optimization of the integration time selection for a KF-based design to improve tracking sensitivity of low dynamic signals. The value of C/N_0 is required, which is challenging to obtain for a weak signal. In reference [4], the receiver oscillator noise and the thermal noise effects were both taken into consideration. *However, the analysis is not applicable to highly dynamic signals and receivers equipped with low quality oscillators.*

II. Frequency locked loop

A cycle-slip and a potential loss of phase lock frequently occurred in a PLL due to its vulnerable phase measurement under a weak signal or highly dynamic environment [50]. Hence, a FLL is often employed for carrier signal tracking by neglecting absolute phase error and permitting relative phase rotation of the received signal and the local carrier replica under some challenging environments with both severe fading and highly dynamics [3, 8, 17, 51].

Much efforts have been devoted to the frequency estimator/discriminator design and analysis. References [3] and [51] investigated the characteristics and inherent nonlinearity of the different coherent frequency discriminators such as the arctangent and cross product frequency discriminators. They also provided the expressions of the noise equivalent bandwidth in the presence of thermal noise. However, when the receiver operates in weak signal conditions, the coherency of the carrier phase between epochs can not be guaranteed. To achieve better frequency estimation, the non-coherent frequency discriminators,

which only use the absolute signal power instead of the difference between successive carrier phase measurements, have been introduced in the frequency tracking. A new type of non-coherent frequency discriminator was proposed in [52], which implemented the so called 'F-correlator'. Reference [53] analyzed the statistics of the non-coherent frequency discriminator and derived the corresponding tracking jitter. Reference [54] applied the discrete time Fourier transform (DTFT) to obtain a maximum likelihood (ML) frequency estimation. Reference [55] applied the cost function of the maximum likelihood estimation (MLE) technique to derive an iterative frequency discriminator.

Similar to PLL, filter design in the FLL has been discussed widely in the literature as well. The conventional method that transfers the analog FLL to the digital FLL to obtain the PIF parameters [8] is exactly the same as that of a traditional PLL design. Different from the traditional PIF design, reference [3] applied the controlled-root method [23] to design the loop filter in the z-domain directly. Reference [30] presented the KF design method based on the frequency error measured from two successive carrier phase difference. References [56] and [57] presented the Extended Kalman Filter (EKF) frequency tracking scheme based on the frequency error measured from the absolute signal power. Reference [58] proposed a noniterative filter-based MLE algorithm to reduce the computational burden of iterative MLE method.

It is known that the oscillator noise has effects on both the carrier phase and frequency tracking accuracy [4]. The oscillator noise accumulates as integration time increases, which also degrades the frequency tracking performance in weak signal processing [4]. Besides, the measurement noise from two successive carrier phase difference is not a white noise [3]. This effect will degrade the tracking performance in KF-based FLLs as well. *However, the detailed analysis of these effects and the advanced design of FLL to handle these effects have not been studied yet.*

III. Frequency-assisted-phase locked loop

Reference [5] shows that PLL is superior to FLL with better tracking accuracy under a high C/N_0 and a low dynamic environment. While, a well-designed FLL will outperform a well-designed PLL tracking threshold under dynamic stress conditions but at the cost of a low measurement accuracy. To improve the robustness and tracking ability of the carrier signal tracking, the combination of FLL and PLL measurements, which is known as FLL-assisted-PLL, has been used in carrier tracking loop design. The PIF-based dual loop tracking

architecture with the arctangent frequency and phase discriminator outputs was designed and analyzed in [5]. Monte Carlo simulation shows that this FLL-assisted-PLL design approach provides the best features when the C/N_0 is above the PLL tracking threshold [5]. The optimum PIF parameters of FLL-assisted-PLL are investigated in [59] to improve the tracking performance under highly dynamic environment. Reference [60] adopts the similar PIF design approach as [5] to design FLL-assisted-PLL but with the different frequency error measurement, where frequency error is measured from the difference of the two correlator outputs. Reference [61] combined the KF design and PIF design in FLL-assisted-PLL, where the KF estimates the frequency rate and feeds this information back to the PIF-based PLL. Reference [30] presented a pure KF design method that utilizes both the frequency and phase arctangent discriminator outputs in FLL-assisted-PLL. Reference [62] proposed an unambiguous frequency-aided PLL (UFA-PLL) for a high-dynamic signal tracking.

2.4.2 Vector Tracking

Vector tracking loop is a closed-loop architecture that utilizes the inherent coupling characteristic between different satellites and the correlation of signal tracking and positioning. This inter-channel aiding characteristic enables vector tracking loop to achieve better tracking performance with weak signals and highly dynamic signals as compared to the traditional scalar tracking loop.

Vector tracking was first proposed in [63] and the structure of vector delay lock loops (VDLL) was used to combine the code tracking among different channels. The result reveals that VDLL is superior to traditional scalar DLL. In carrier signal tracking, the vector tracking loop utilizes observations from all available channels to estimate carrier phase or Doppler frequency of each individual channel. Multicarrier vector phase locked loop (MC-VPLL) combined traditional PLL technique was proposed in [64], where the orthogonal projection method was used to determine the optimal filter parameters in order to eliminate clock and atmospheric errors. Vector frequency locked loop (VFLL) assisted VPLL for carrier phase tracking was presented in [65]. The results demonstrated that better performance of carrier phase tracking in degraded signal environment can be achieved by using this algorithm. In [66,67], a vector delay frequency lock loop (VDFLL) architecture was implemented in the navigation processor, and replaces the traditional scalar tracking loops completely which allows tracking weak signals with C/N_0 as low as 10 dB-Hz. The combined approach of the

block processing and centralized VDFLL was utilized in [68] for robust indoor navigation. Reference [69] is also a vector tracking implementation with the additional improvement of an inertial measurement unit. It tracks fully coherent well below 10 dB-Hz.

Dr Lashley has published many valuable papers in this area [70–77]. A method for making a valid comparison between VDFLL and scalar tracking loops was developed in [71]. In the comparison, the traditional scalar tracking loop is characterized by loop bandwidth and order, while the KF in VDFLL is characterized by process and measurement noise. The improvement in vector tracking over scalar tracking ranges from 2.4 to 6.2 dB in various scenarios. Two different formulations of VDFLL, such as position-state and pseudo-range-state formulations, were presented in [72] and were demonstrated equivalent to each other. Reference [74] explored the tracking ability of VDFLL in weak and highly dynamic tracking and demonstrated that the VDFLL is able to operate through 2g and 4g turns at C/N_0 of 16dB-Hz.

Nevertheless, the vector-tracking loop is vulnerable due to the inter-dependence of all tracking channels. Vector tracking is sensitive to faults because a fault occurring in one channel could propagate to the other channels. To solve this issue, the effectiveness of vector-tracking in signal faded environments was investigated in [78]. Reference [79] proposed an adaptive vector-tracking loop based on both the linear local filter and adaptive navigation filter. Results show that when the satellite signals are weak, the adaptive vector-tracking loop performs better as compared to the conventional vector-tracking loop. A review of internal operations of the vector architecture and integrity study of the vector loops was presented in [80] and the receiver autonomous integrity monitoring (RAIM) scheme in vector tracking loop was proposed to address the fault detection issue [81, 82]. Recently, a novel vector tracking with a moving horizon estimation(MHE) approach to enhance the vector tracking robustness by incorporating constraints was proposed in [83]. Simulation results show that MHE-based vector tracking is more robust to environment change than the traditional KF-based vector tracking.

2.4.3 Open Loop Tracking

Both scalar and vector tracking architecture can be classified as closed-loop tracking where the local estimations are updated based on the feedback information. The difference between the system input and output is gradually reduced through the feedback process. However,

when the signal is extremely weak, the loss-of-lock probably occurs through the feedback operation from the incorrect system output. In contrast to closed-loop feedback process, open loop control system neither measured nor feed back the system output for comparison with the reference input. Therefore, loss-of-lock and system stability are not major problems in open loop control systems [84].

Open loop technique was originally used to process radio occultation signals [85–88] in GNSS receivers. It has been found that the open loop tracking has good performance due to its inherent stability. Subsequently, the open loop tracking is adopted for weak GNSS signal processing. The batch processing technique is widely used in the open loop tracking and has greatly improved the tracking robustness as compared to the traditional closed-loop receiver architecture [89, 90].

The stability in the open loop is guaranteed but at the cost of a low estimation accuracy and a high computational complexity. A proper combination of open-loop and closed-loop controls may give a satisfactory overall system performance. The quasi-open loop architecture has been proposed in [89] as the transition architecture between open- and closed-loop to improve the stability and accuracy. The quasi-open loop that uses zoom fast fourier transform(FFT) approach could reduce the computational complexity of the standard FFT computation by computing the correlation of the area around the peak [91]. The novel quasi-open loop architecture works with three different rates was proposed in [92], which allows the higher flexibility and freedom in loop filter design.

In carrier signal tracking, reference [93] proposed the circular data processing tools to track the GNSS signals phase in a phase open loop (POL), especially in the case of multi-channel signal architecture. Reference [94] proposed POL for phase and frequency tracking, where the long integration time is used by suppressing the temporal correlation in strong noise environment. The open loop tracking with FFT-based frequency discriminators was proposed in [95] for weak signal tracking. Reference [96] proposed and characterized the open loop tracking schemes for fine frequency estimation.

In summary, the vector tracking and the open loop tracking are more capable, robust, and stable in dealing with high attenuation and highly dynamic signals than the scalar carrier tracking loop. To improve the scalar carrier tracking loop design, both of the frequency and phase estimations should be accurately estimated and updated in NCO model since they jointly determine the carrier tracking performance. This is difficult to design and implement in the traditional carrier tracking loop design since it only considers the relationship

between single-input and single-output. Therefore, the multi-input multi-output tracking architecture in state space design is useful to satisfy such an advanced design requirement. The general state space design process will be discussed in the following section to provide the theoretical foundation for state space-based GNSS carrier tracking loop design.

2.5 General State Space Design Process

Conventional design methods of a control system, such as the root locus and frequency response methods, are useful for dealing with single-input single-output systems [97]. They are based on the input-output relationship, or transfer function, of the system. A modern control system may have multiple inputs and outputs, and some of them may be interrelated in complex ways. For analysis and optimal controller design of multiple-input multiple-output systems, the state space method is more suitable [97].

Given a system model, the design of a control system involves the design of a controller $\mathbf{u}_k$ to control the plant to follow the desired trajectory. The design process for a state feedback control system is depicted in Fig. 2.9. It includes the following steps: 1). Modeling a plant; 2). Designing and analyzing a controller for the plant; 3). Designing the state estimator.

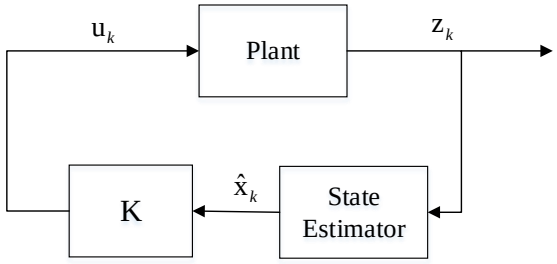

Figure 2.9: State feedback design paradigm in control system.

The plant model for a discrete time system can be represented as [97]:

$$\mathbf{x}_{k+1} = \mathbf{A}\mathbf{x}_k + \mathbf{B}\mathbf{u}_k + \mathbf{n}_k \tag{2.40}$$

$$\mathbf{z}_k = \mathbf{H}\mathbf{x}_k + \mathbf{v}_k \tag{2.41}$$

where

$\mathbf{x}_k \in \mathcal{R}^{n\times 1}$ is the state vector

$\mathbf{z}_k \in \mathcal{R}^{m\times 1}$ is the measurement vector

$\mathbf{n}_k \in \mathcal{R}^{n\times 1}$ is the system noise vector

$\mathbf{v}_k \in \mathcal{R}^{m\times 1}$ is the measurement noise vector

$\mathbf{A} \in \mathcal{R}^{n\times n}$ is the system transition matrix

$\mathbf{H} \in \mathcal{R}^{m\times n}$ is the measurement matrix

and $\mathbf{B}$ is an operator that maps the controller $\mathbf{u}_k$ to the plant. The matrix $\mathbf{B}$ should be chosen to make the pair $(\mathbf{A}, \mathbf{B})$ controllable; thus the system state can transition from an arbitrary initial value to any desired value in a finite time period regardless of the controller [97].

To design the controller $\mathbf{u}_k$ for a closed-loop control system, the feedback strategy can be adopted and $\mathbf{u}_k$ is typically chosen as:

$$\mathbf{u}_k = \mathbf{K}\mathbf{x}_k \tag{2.42}$$

where $\mathbf{K}$ is the state feedback gain matrix. To ensure the stability of the control system, $\mathbf{K}$ should be designed to make eigenvalues of $(\mathbf{A} + \mathbf{B}\mathbf{K})$ less than 1. The pole placement approach can be adopted to make the eigenvalues of $(\mathbf{A} + \mathbf{B}\mathbf{K})$ at the desired locations, such as the origin in a typical control system design [97].

Finally, the design process the state feedback is accomplished by using the actual state variables if the state variables are measurable. However, $\mathbf{x}_k$ may not be available in reality. In this case, we construct a state estimator (e.g. KF) as follows:

$$\hat{\mathbf{x}}_{k+1} = \mathbf{A}\hat{\mathbf{x}}_k + \mathbf{B}\mathbf{u}_k + \mathbf{L}_k(\mathbf{z}_{k+1} - \hat{\mathbf{z}}_{k+1}) \tag{2.43}$$

where

$$\hat{\mathbf{z}}_{k+1} = \mathbf{H}\hat{\mathbf{x}}_{k+1} \tag{2.44}$$

$$\tag{2.45}$$

In this case, the estimated state variables $\hat{\mathbf{x}}_k$ instead of the actual state variables $\mathbf{x}_k$ are used by the controller in equation (2.42) to control the plant. It is noted that besides

KF, many other filter techniques and estimation approaches, such as the least squares estimation (LSE) [32] and the moving horizon estimation (MHE) [98], could be used to design the state estimator. Among these designs, the state estimations in KF and MHE are adjusted according to the state model and the measurement, which can be classified as a model-based design process. When knowledge of the state model is available, KF and MHE may lead to a more superior design of the complex dynamic systems.

In summary, the state feedback control system design is characterized by the three gain matrices, i.e., the plant operator matrix $\mathbf{B}$, the state feedback gain matrix $\mathbf{K}$ and the state estimator gain matrix $\mathbf{L}$. The design of the plant operator matrix $\mathbf{B}$ is to ensure controllability, which is a necessary condition for placing the closed-loop pole locations [97]. The procedure for determining the state feedback gain matrix $\mathbf{K}$ is to select suitable locations for all closed-loop poles so that the effects of the disturbances can be minimized with sufficient speed [97]. The design of state estimator gain matrix $\mathbf{L}$ is to extract the actual state information from the noisy measurement for state feedback control. The overall system performance is determined by the choice of these three gain matrices. Hence, the design of the control system involves the design of $\mathbf{B}$, $\mathbf{K}$, and $\mathbf{L}$ and this design approach can be applied for the subsequent phase and frequency tracking loop designs.

Chapter 3

State feedback/state estimator design for phase tracking loop[2]

The previous chapter presented the state feedback/state estimator design process for closed control system design. This chapter will apply the state space design methodology in phase tracking loop design.

3.1 System Model

The following state space system model:

$$\mathbf{x}_{k+1} = \mathbf{A}_P \mathbf{x}_k + \mathbf{n}_k \tag{3.1}$$

$$\mathbf{z}_k = \mathbf{H}_P \mathbf{x}_k + \mathbf{v}_k \tag{3.2}$$

is widely applied for GNSS carrier signal tracking loop design [31], where the platform dynamics, oscillator noise, and thermal noise effects can be incorporated into these models.

[2]Chapter 3 is the phase tracking loop part of our papers "R. Yang, KV Ling, EK Poh, and Y.Morton, *Generalized GNSS Signal Carrier Tracking: Part I: Modelling and Analysis*, accepted by IEEE Transactions on Aerospace and Electronic Systems, January 2017. " and "R. Yang, Y.Morton, KV Ling, and EK Poh, *Generalized GNSS Signal Carrier Tracking: Part II: Optimization and Implementation*, accepted by IEEE Transactions on Aerospace and Electronic Systems, January 2017."

3.1.1 State model

The state vector $\mathbf{x}_k$, which describes the received carrier signal on dynamic platforms at the k^{th} epoch, can be expressed as a 2-state or a 3-state vector as follows:

$$2-state:\mathbf{x}_k=\left[\begin{array}{cc}\varphi & \omega\end{array}\right]_k^{\mathrm{T}} \tag{3.3}$$

$$3-state:\mathbf{x}_k=\left[\begin{array}{ccc}\varphi & \omega & \dot{\omega}\end{array}\right]_k^{\mathrm{T}} \tag{3.4}$$

where φ_k is the initial fractional phase in rad, ω_k is carrier frequency in rad/s, and $\dot{\omega}_k$ is the frequency rate in rad/s^2.

The system transition matrix $\mathbf{A}_P$ in phase tracking loop has the following forms [30] [99]:

$$2-state:\mathbf{A}_P=\left[\begin{array}{cc}1 & T\\ 0 & 1\end{array}\right] \tag{3.5}$$

$$3-state:\mathbf{A}_P=\left[\begin{array}{ccc}1 & T & \frac{T^2}{2}\\ 0 & 1 & T\\ 0 & 0 & 1\end{array}\right] \tag{3.6}$$

where T represents the coherent integration time (typically 1ms for GPS L1 CA signals).

The vector $\mathbf{n}_k$, representing the system intrinsic noise, typically includes the oscillator noise effect in the RF front-end and the random walk process due to the platform dynamics in GNSS applications [4]. Its covariance matrix $\mathbf{Q}_P$ are dependent on receiver platform dynamics [4,18]:

$$2-state:\mathbf{Q}_P=\left[\begin{array}{cc}\sigma_\varphi^2 & \sigma_{\omega\varphi}^2\\ \sigma_{\omega\varphi}^2 & \sigma_\omega^2\end{array}\right]=(2\pi f_L)^2\left[\begin{array}{cc}Tq_\varphi+\frac{T^3}{3}q_\omega & \frac{T^2}{2}q_\omega\\ \frac{T^2}{2}q_\omega & Tq_\omega\end{array}\right] \tag{3.7}$$

$$3-state:\mathbf{Q}_P=\left[\begin{array}{ccc}\sigma_\varphi^2 & \sigma_{\omega\varphi}^2 & \sigma_{\dot{\omega}\varphi}^2\\ \sigma_{\omega\varphi}^2 & \sigma_\omega^2 & \sigma_{\omega\dot{\omega}}^2\\ \sigma_{\dot{\omega}\varphi}^2 & \sigma_{\omega\dot{\omega}}^2 & \sigma_{\dot{\omega}}^2\end{array}\right]=(2\pi f_L)^2\left[\begin{array}{ccc}Tq_\varphi+\frac{T^3}{3}q_\omega+\frac{T^5}{20}\frac{q_a}{c^2} & \frac{T^2}{2}q_\omega+\frac{T^4}{8}\frac{q_a}{c^2} & \frac{T^3}{6}\frac{q_a}{c^2}\\ \frac{T^2}{2}q_\omega+\frac{T^4}{8}\frac{q_a}{c^2} & Tq_\omega+\frac{T^3}{3}\frac{q_a}{c^2} & \frac{T^2}{2}\frac{q_a}{c^2}\\ \frac{T^3}{6}\frac{q_a}{c^2} & \frac{T^2}{2}\frac{q_a}{c^2} & T\frac{q_a}{c^2}\end{array}\right] \tag{3.8}$$

In equations (3.7) and (3.8), f_L is the carrier frequency ($f_L=1575.42MHz$ for the GPS L1 signal), q_φ and q_ω represent the power spectral density of the carrier phase noise and carrier frequency noise due to the local oscillator, respectively. Given the oscillator h-parameters

h_0 and h_{-2}, the spectral densities q_φ and q_ω are obtained as follows [4, 18]:

$$q_\varphi = \frac{h_0}{2} \tag{3.9}$$

$$q_\omega = 2\pi^2 h_{-2}. \tag{3.10}$$

The values of the oscillator h-parameters depend on the type of oscillator used in receivers. In GNSS applications, temperature-compensated oscillators (TCXO) and oven-controlled oscillators (OCXO) are commonly used [6,8]. Two receiver front-ends, one with a low quality oscillator (LQO) similar to that of a TCXO, while the other has a high quality oscillator (HQO) similar to that of an OCXO, will be used in analysis and simulation validation in this thesis. Their h-parameters are set as $h_0 = 1 \times 10^{-21}(s^2/\text{Hz})$, $h_{-2} = 2 \times 10^{-20}(1/\text{Hz})$ for the receiver front-end with LQO, and $h_0 = 6.4 \times 10^{-26}(s^2/\text{Hz})$, $h_{-2} = 4.3 \times 10^{-23}(1/\text{Hz})$ for the receiver front-end with HQO, respectively. These values are similar to typical values that can be found in [4, 18]. Additionally, the parameter q_a in equation (3.8) denotes the power spectral density of the random walk process due to the LOS platform acceleration with the unit of m^2/s^5 [4] and c is the speed of light ($3 \times 10^8 m/s$). When the receiver is static or moving with a nearly constant velocity, q_a should be set to 0 and the 3-state model degenerates to a 2-state model. When the receiver is moving with a nearly constant acceleration, q_a should be set to a small value. For receivers on more dynamic platforms where the LOS acceleration may change in the receiver-satellite LOS direction over short range, where the maximum changes over a sampling period T should be on the order of $\sqrt{q_a T}$ [100]:

$$\sqrt{q_a T} \propto j_M T \tag{3.11}$$

where j_M is maximum LOS jerk. A practical range for $\sqrt{q_a T}$ is [100]:

$$0.5 j_M T \leq \sqrt{q_a T} \leq j_M T \tag{3.12}$$

Note that $j_M T$ should be relatively small compared to the actual acceleration levels. Thus, by using this relationship we can set the corresponding value of q_a according to the empirical knowledge of the platform's dynamics. Several values of q_a, i.e., $q_a = 0 m^2/s^5$, $q_a = 0.1 m^2/s^5$, and $q_a = 10 m^2/s^5$ are used to represent the static, low dynamic, and high dynamic scenarios in the subsequent sections. Assuming that $T = 1ms$ for the normal signal tracking and according to equation (3.12), the corresponding values for j_M are $10 m/s^3$ and

$100m/s^3$ for the low and high dynamic scenarios, respectively. A maximum $10m/s^3$ jerk probably occurs in a car or a train. A maximum $100m/s^3$ jerk probably occurs in the high dynamic platforms, such as airplane and aircraft. Therefore, the values of $q_a = 0m^2/s^5$, $q_a = 0.1m^2/s^5$, and $q_a = 10m^2/s^5$ represent the receiver mounted at the static locations, low dynamic platforms, such as car and train, and high dynamic platforms, such as airplane and aircraft, respectively. Additionally, q_a with the value even larger than $10m^2/s^5$ can be used for the ionosphere scintillation scenario where the phase fluctuates at rapid speed.

3.1.2 Measurement model

Although in real world applications, there are various error sources, such as interference [101], ionospheric scintillation [102], and time-correlated clock errors [103], that corrupt and distort carrier phase measurements, only white Gaussian thermal noise effects are considered in the analysis presented here the measurement noise is assumed to be uncorrelated with the system noise. In this thesis, we use the simplest measurement model to illustrate the general design process in the state space framework. If a more sophisticated signal model that considers the interference, ionospheric scintillation and clock errors is available, it can be included in the design process. The carrier phase θ_k of the received signal, which includes the average input signal phase $\bar{\theta}_k$ during the integration time T and the white Gaussian noise, v_k, can be described as

$$\theta_k \triangleq \bar{\theta}_k + v_k = \mathbf{H}_P \mathbf{x}_k + v_k \tag{3.13}$$

where $\mathbf{H}_P$ is the measurement matrix [99]:

$$2 - state : \mathbf{H}_P = \begin{bmatrix} 1 & \frac{T}{2} \end{bmatrix} \tag{3.14}$$

$$3 - state : \mathbf{H}_P = \begin{bmatrix} 1 & \frac{T}{2} & \frac{T^2}{6} \end{bmatrix}. \tag{3.15}$$

Let the vector $\hat{\mathbf{x}}_k$ to denote the local estimate of $\mathbf{x}_k$. The average phase $\hat{\theta}_k$ of a local generated signal can be expressed as:

$$\hat{\theta}_k \triangleq \mathbf{H}_P \hat{\mathbf{x}}_k. \tag{3.16}$$

Since θ_k cannot be directly measured, the phase error $\Delta\theta_k = \theta_k - \hat{\theta}_k$ is used as the

measurement in real implementations. From (3.13) and (3.16), we have:

$$\Delta\theta_k = \mathbf{H}_P \Delta\mathbf{x}_k + v_k \tag{3.17}$$

where $\Delta\mathbf{x}_k = (\mathbf{x}_k - \hat{\mathbf{x}}_k)$. $\Delta\theta_k$ is the average phase error which contains all the estimated state errors, i.e., the initial phase error, the frequency error, and the frequency rate error if the frequency rate is considered. This average phase error can be obtained from the phase discriminator, see equation (2.18). Generally, the two-quadrant or four-quadrant arctangent carrier phase discriminators are adopted in generic receiver design for the signals with and without navigation message modulations due to their linear characteristic in the range of $-90°$ to $90°$ and $-180°$ to $180°$, respectively [8]. The noise variance σ_v^2 of v_k in an arctangent discriminator output is given as [18, 19]

$$\mathbf{R} = \sigma_v^2 = \frac{1}{2TC/N_0}\left(1+\frac{1}{2TC/N_0}\right) \tag{3.18}$$

The typical value of C/N_0 for nominal signal strength is above 40dB-Hz.

3.2 State Space Design For Phase Tracking Loop

Fig.3.1 shows the block diagram of the closed phase tracking loop in the GNSS receiver.

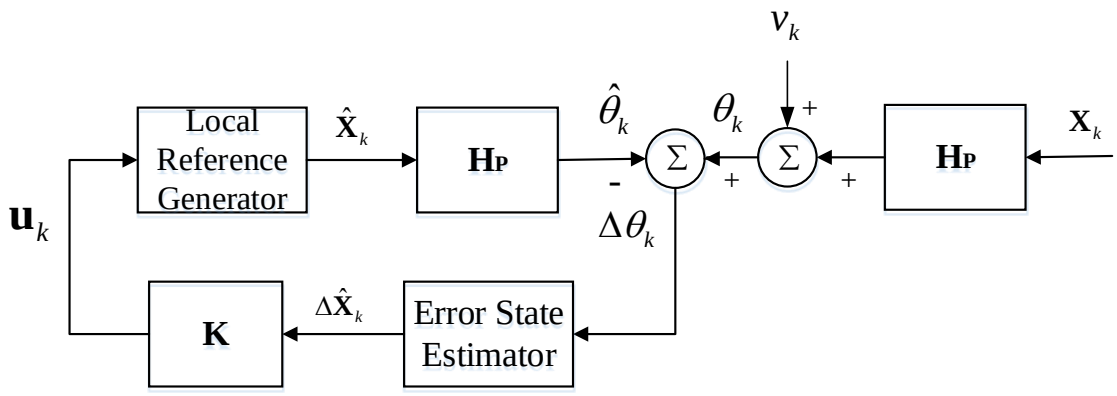

Figure 3.1: Closed-loop phase tracking architecture in GNSS software receiver.

Assuming that the local reference generator is controlled by the input signal, $\mathbf{u}_k$, then

the local signal generated by the local reference generator can be expressed as:

$$\hat{\mathbf{x}}_{k+1} = \mathbf{A}_P \hat{\mathbf{x}}_k + \mathbf{B}\mathbf{u}_k. \tag{3.19}$$

Substracting (3.19) from (3.1) and letting $\Delta\mathbf{x}_{k+1} = \mathbf{x}_{k+1} - \hat{\mathbf{x}}_{k+1}$, we have the error state plant model as:

$$\Delta\mathbf{x}_{k+1} = \mathbf{A}_P \Delta\mathbf{x}_k - \mathbf{B}\mathbf{u}_k + \mathbf{n}_k \tag{3.20}$$

The objective of the tracking loop is to drive $\Delta\mathbf{x}_k$ towards zero. It can be achieved if we select

$$\mathbf{u}_k = \mathbf{K}\Delta\mathbf{x}_k \tag{3.21}$$

such that $\mathbf{A}_P - \mathbf{B}\mathbf{K}$ has all its eigenvalues within the stability region. Since, $\Delta\mathbf{x}_k$ is not directly measurable, but it has to be estimated from the phase error measurement $\Delta\theta_k$ (equation (3.17)), equation (3.21) is then replaced by

$$\mathbf{u}_k = \mathbf{K}\Delta\hat{\mathbf{x}}_k. \tag{3.22}$$

with a state estimator of the form:

$$\Delta\hat{\mathbf{x}}_{k+1} = \mathbf{A}_P \Delta\hat{\mathbf{x}}_k - \mathbf{B}\mathbf{u}_k + \mathbf{L}\left(\Delta\theta_{k+1} - \mathbf{H}_P(\mathbf{A}_P \Delta\hat{\mathbf{x}}_k - \mathbf{B}\mathbf{u}_k)\right) \tag{3.23}$$

where $\mathbf{L}$ is the estimator gain matrix.

Substituting equation (3.22) into (3.23), the error estimation can be obtained as:

$$\Delta\hat{\mathbf{x}}_{k+1} = \left(\mathbf{I} - \mathbf{L}\mathbf{H}_\mathbf{P}\right)\left(\mathbf{A}_\mathbf{P} - \mathbf{B}\mathbf{K}\right)\Delta\hat{\mathbf{x}}_k + \mathbf{L}\Delta\theta_{k+1}. \tag{3.24}$$

Finally, this estimation is input to the local reference generator, and using equations (3.19) and (3.22), the local signal can be generated as:

$$\hat{\mathbf{x}}_{k+1} = \mathbf{A}_P \hat{\mathbf{x}}_k + \mathbf{B}\mathbf{K}\Delta\hat{\mathbf{x}}_k. \tag{3.25}$$

The above equation shows that the state feedback tracking loop design is characterized by the three gain matrices, i.e., the plant input matrix $\mathbf{B}$, the state feedback gain matrix $\mathbf{K}$, and the state estimator gain matrix $\mathbf{L}$. The design of these matrices will be discussed next.

3.3 B, K, and L Matrices Design Considerations

3.3.1 B and K design

The state estimation in equation (3.19) is updated by the control signal $\mathbf{u}_k$. $\mathbf{B}$ should satisfy the following condition to guarantee the system controllability [97]:

$$rank[\mathbf{B}|\mathbf{A}_P\mathbf{B}|...|\mathbf{A}_P^{n-1}\mathbf{B}] = n \tag{3.26}$$

where n is the state dimension.

To ensure the system stability, $\hat{\mathbf{x}}_{k+1}$ should follow the variation of the received signal $\mathbf{x}_{k+1}$; therefore, $\Delta\mathbf{x}_{k+1}$ should converge to zero. Hence, the matrices $\mathbf{B}$ and $\mathbf{K}$ should satisfy the following condition [97]

$$|eig(\mathbf{A_P} - \mathbf{BK})| < 1. \tag{3.27}$$

Clearly, $\mathbf{A_P} - \mathbf{BK}$ with different eigenvalues will lead to different system responses. On the one hand, we desire the closed loop control system to reach steady state value with the minimum possible settling time. On the other hand, the system should also be designed without steady-state error and with minimal ripples between the sampling instants. This is the so-called deadbeat response design in control theory which can be achieved by forcing the eigenvalues of the matrix $\mathbf{A}_P - \mathbf{BK}$ to be zeros [97]

$$eig(\mathbf{A}_P - \mathbf{BK}) = 0. \tag{3.28}$$

More importantly, this deadbeat response design simplifies the error dynamic of (3.24) so that the corresponding state estimation update method is similar to those in the literature [30].

Taking the 2-state system as an example, there are six possible choices of $\mathbf{B}$:

$$\begin{bmatrix} 1 \\ 0 \end{bmatrix}, \begin{bmatrix} 0 \\ 1 \end{bmatrix}, \begin{bmatrix} 1 \\ 1 \end{bmatrix}, \tag{3.29}$$

$$\begin{bmatrix} 1 & 0 \\ 0 & 0 \end{bmatrix}, \begin{bmatrix} 0 & 0 \\ 0 & 1 \end{bmatrix}, and \begin{bmatrix} 1 & 0 \\ 0 & 1 \end{bmatrix} \tag{3.30}$$

depending whether $\mathbf{u}_k$ is a scalar or a 2×1 vector.

A straight forward controllability analysis shows that only $\mathbf{B} = [1;1]$ and $\mathbf{B} = [1,0;0,1]$ are acceptable. This is because for $\mathbf{B} = [1;0]$ and $[1,0;0,0]$, the rank of $[\mathbf{B}|\mathbf{A}_P\mathbf{B}]$ is 1, which indicates uncontrollable systems. For $\mathbf{B} = [0;1]$, $[1;1]$, and $[0,0;0,1]$, the rank of $[\mathbf{B}|\mathbf{A}_P\mathbf{B}]$ is 2 only when the value of T is nonzero, which is indeed the case for a GNSS tracking loop. However, for $\mathbf{B} = [0;1]$ and $[0,0;0,1]$, it is not possible for $\hat{\mathbf{x}}_k$ to transit from an arbitrary state to a desired state in one step. Finally, for $\mathbf{B} = [1,0;0,1]$, $[\mathbf{B}|\mathbf{A}_P\mathbf{B}]$ is full rank, regardless of the value of T, and hence the system is completely controllable. Therefore, $\mathbf{B} = [1;1]$ and $[1,0;0,1]$ are the only candidates associated with controllable systems for the scalar and vector controller $\mathbf{u}_k$, respectively. It should be noted that indeed $\mathbf{B} = [1,0;0,1]$ was adopted in [48] although detailed explanation was not provided.

To ensure the closed-loop matrix $\mathbf{A}_P - \mathbf{B}\mathbf{K}$ has all its eigenvalues at the origin, the well-known pole placement approach [97] was applied to derive the matrix $\mathbf{K}$ as follows:

$$\mathbf{K} = \begin{cases} \begin{bmatrix} \frac{1}{T} & 2 - \frac{1}{T} \end{bmatrix}, & \text{for } \mathbf{B} = \begin{bmatrix} 1 \\ 1 \end{bmatrix} \\ \begin{bmatrix} 1 & T \\ 0 & 1 \end{bmatrix} \text{ or } \begin{bmatrix} 1 & 0 \\ 0 & 1 \end{bmatrix}, & \text{for } \mathbf{B} = \begin{bmatrix} 1 & 0 \\ 0 & 1 \end{bmatrix} \end{cases} \tag{3.31}$$

and the corresponding closed-loop matrix is:

$$\mathbf{A}_P - \mathbf{B}\mathbf{K} = \begin{cases} \begin{bmatrix} 1 - \frac{1}{T} & T - 2 + \frac{1}{T} \\ -\frac{1}{T} & -1 + \frac{1}{T} \end{bmatrix}, & \text{for } \mathbf{B} = \begin{bmatrix} 1 \\ 1 \end{bmatrix}, \text{ and } \mathbf{K} = \begin{bmatrix} \frac{1}{T} & 2 - \frac{1}{T} \end{bmatrix} \\ \begin{bmatrix} 0 & 0 \\ 0 & 0 \end{bmatrix}, & \text{for } \mathbf{B} = \mathbf{I}, \text{ and } \mathbf{K} = \mathbf{A}_P \\ \begin{bmatrix} 0 & T \\ 0 & 0 \end{bmatrix}, & \text{for } \mathbf{B} = \mathbf{I}, \text{ and } \mathbf{K} = \mathbf{I} \end{cases} \tag{3.32}$$

Equation (3.32) shows that for $\mathbf{K} = \begin{bmatrix} \frac{1}{T} & 2 - \frac{1}{T} \end{bmatrix}$ and $\mathbf{B} = [1;1]$, the values of $\mathbf{K}$ and $\mathbf{A}_P - \mathbf{B}\mathbf{K}$ become very large in GNSS tracking loops since the typical value of T is 1ms for normal signal tracking (around 44dB-Hz) in GNSS applications. Therefore, the error state is accumulated and amplified by this gain through equations (3.22) and (3.24). Such a situation should be avoided in control system design. According to (3.24) and (3.32), for $\mathbf{B} = \mathbf{I}$ and $\mathbf{K} = \mathbf{I}$, the error state estimation becomes a first-order Gauss-Markov process, with which an inaccurate prior estimation will affect the present estimates. This effect

will be eliminated in 2 sampling periods, since $(\mathbf{A}_P - \mathbf{BK})^2 = 0$. For the case $\mathbf{B} = \mathbf{I}$ and $\mathbf{K} = \mathbf{A}_P$, equation (3.24) reduces to $\Delta\hat{\mathbf{x}}_{k+1} = \mathbf{L}\Delta\theta_{k+1}$, hence the integrator action in the estimator is eliminated and the estimation error will not be accumulated. Hence, the desired state could be achieved instantly. A similar conclusion can be derived for the 3-state case.

Although this thesis focuses on a general design framework and fundamental performance analysis, practical implementation feasibility and constraints should still be taken into consideration for the proposed schemes. One such practical issue concerns the implementation of the local reference generator, which corresponds to the NCO in the traditional tracking loop. In a traditional PLL, the loop filter output is used for a NCO to update its carrier phase and carrier frequency (phase-rate) registers. In a PLL with rate-only feedback NCO, the NCO rate register is updated, but the NCO phase register is left untouched, while in a PLL with phase and phase-rate feedback NCO, both the rate and phase registers are updated, based on the single input from the loop filter output [20, 23, 24]. Therefore, if $\mathbf{u}_k$ is selected as a scalar variable and $\mathbf{B}$ is set to $[0; 1]$ or $[1; 1]$, the local reference generators effectively correspond to the so-called traditional rate-only feedback NCO or phase and rate feedback NCO. These selections correspond to the single-input systems and were preferred in practical design due to their simplicity. The above analysis on controllability and stability presented in this paper leads to the recommendation of a two-input system, which requires carrier phase and phase-rate updated with respect to their corresponding corrections from the two-input variables. While the two-input system imposes certain limitations on practical implementations, such limitations are diminishing as the receiver design trend becomes more software-defined. The same argument applies to the multi-input NCO model challenges in the 3-state system. If we assume that the NCO is implemented in software, then the 3-state variables: $\hat{\varphi}$, $\hat{\omega}$, and $\hat{\dot{\omega}}$ can be used to generate the carrier signals. However, if traditional designs implement only the single-input NCOs where the phase and phase-rate registers for some practical reasons, then some conversions from multi-input to single-input, as well as some approximations between the frequency-rate ($\hat{\dot{\omega}}$) register, and phase-rate register are needed.

Finally, substituting $\mathbf{B} = \mathbf{I}$ and $\mathbf{K} = \mathbf{A_P}$ into equations (3.19), (3.22), and (3.24), the local reference generator output can be obtained as

$$\hat{\mathbf{x}}_{k+1} = \mathbf{A}_P\hat{\mathbf{x}}_k + \mathbf{A}_P\mathbf{L}\Delta\theta_k \tag{3.33}$$

where $\mathbf{L}$ is the estimator gain, and it determines the state estimation performance.

3.3.2 Estimator Gain Matrix L

The estimator gain matrix $\mathbf{L}$ will be analyzed for three filter designs commonly used in practical PLL implementations: PIF, WF, and KF. The PIF and WF can be classified as a traditional single-input single-output system based on the transfer function from scalar phase input to scalar phase output. KF is based on the state and the measurement models in state space, which can be classified as a model-based design. For PIF and WF, we obtain their gain matrix $\mathbf{L}$ through their corresponding closed loop transfer function, while for KF, its gain matrix is derived according to the state and measurement models.

The closed-loop transfer function in the state feedback phase tracking loop with $\mathbf{B} = \mathbf{I}$, $\mathbf{K} = \mathbf{A}_P$ can be obtained as

$$F(z) = \frac{\hat{\theta}_k}{\theta_k} = \frac{\mathbf{H}_P(z\mathbf{I} - \mathbf{A}_P)^{-1}\mathbf{A}_P\mathbf{L}}{1 + \mathbf{H}_P(z\mathbf{I} - \mathbf{A}_P)^{-1}\mathbf{A}_P\mathbf{L}}. \tag{3.34}$$

Let $\mathbf{L}$ take the following forms for the 2- and 3-state model respectively:

$$2 - state : \mathbf{L} = \begin{bmatrix} \alpha & \beta \end{bmatrix}^{\mathrm{T}} \tag{3.35}$$

$$3 - state : \mathbf{L} = \begin{bmatrix} \alpha & \beta & \gamma \end{bmatrix}^{\mathrm{T}}. \tag{3.36}$$

Their corresponding closed-loop transfer functions can be written as:

$$F_2(z) = \frac{\left(\alpha + \frac{3T}{2}\beta\right) z - \left(\alpha + \frac{T}{2}\beta\right)}{z^2 + \left(\alpha + \frac{3T}{2}\beta - 2\right) z + \left(-\alpha - \frac{T}{2}\beta + 1\right)} \tag{3.37}$$

and

$$F_3(z) = \frac{\left(7T^2\gamma + 9T\beta + 6\alpha\right) z^2 + \left(-2T^2\gamma - 12T\beta - 12\alpha\right) z + T^2\gamma + 3T\beta + 6\alpha}{6z^3 + \left(7T^2\gamma + 9T\beta + 6\alpha - 18\right) z^2 + \left(-2T^2\gamma - 12T\beta - 12\alpha + 18\right) z + T^2\gamma + 3T\beta + 6\alpha - 6} \tag{3.38}$$

Proportional integral filter

PIF is based on the discretization of analog PLL [8,9], and both the practical and theoretical aspects of analog PLL and their performances under various conditions are well developed. The implementation of Fig. 3.1 using second-order and third-order analog PLLs with PIF is shown in Fig.3.2. Their loop parameters can be obtained by the predefined values of damping ratio and noise equivalent bandwidth, as listed in Table 2.1 [8]. Here, we denote w_p as the natural frequency in phase tracking loop and it can be calculated by the predefined value of phase tracking loop bandwidth BN.

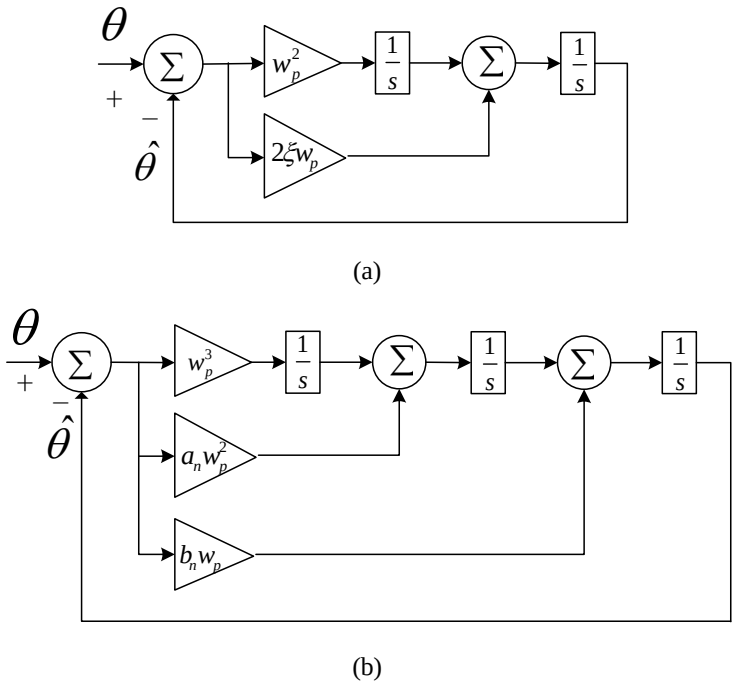

Figure 3.2: Analog PLL. (a) Second order. (b) Third order.

The closed-loop transfer functions for the second- and third-order PLLs can be obtained as

$$H_{PIF2}(s) = \frac{2\xi w_p s + w_p^2}{s^2 + 2\xi w_p s + w_p^2} \tag{3.39}$$

$$H_{PIF3}(s) = \frac{b_n w_p s^2 + a_n w_p^2 s + w_p^3}{s^3 + b_n w_p s^2 + a_n w_p^2 s + w_p^3} \tag{3.40}$$

By using the forward Euler transformation $s = (z-1)/T$ (valid only for $BN \cdot T \ll 1/2$ [20]),

we discretize equations (3.39) and (3.40) from the s-domain to the z-domain as:

$$H_{PIF2}(z) = \frac{2\xi w_p T z + w_p^2 T^2 - 2\xi w_p T}{z^2 + (2\xi w_p T - 2) z + \left(w_p^2 T^2 - 2\xi w_p T + 1\right)} \tag{3.41}$$

$$H_{PIF3}(z) = \frac{(b_n w_p T) z^2 + \left(a_n w_p^2 T^2 - 2 b_n w_p T\right) z + \left(w_p^3 T^3 - a_n w_p^2 T^2 + b_n w_p T\right)}{z^3 + (b_n w_p T - 3) z^2 + \left(a_n w_p^2 T^2 - 2 b_n w_p T + 3\right) z + \left(w_p^3 T^3 - a_n w_p^2 T^2 + b_n w_p T - 1\right)} \tag{3.42}$$

Comparing (3.37) and (3.38) with (3.41) and (3.42), we obtain the estimator gain matrix $\mathbf{L}$ for the 2-state and 3-state state feedback tracking loops, respectively:

$$\mathbf{L}_{PIF2} = \begin{bmatrix} \alpha \\ \beta \end{bmatrix} = \begin{bmatrix} 2\xi w_p T - \frac{3}{2} w_p^2 T^2 \\ w_p^2 T \end{bmatrix} \tag{3.43}$$

$$\mathbf{L}_{PIF3} = \begin{bmatrix} \alpha \\ \beta \\ \gamma \end{bmatrix} = \begin{bmatrix} (11 w_p^3 T^3 - 9 a_n w_p^2 T^2 + 6 b_n w_p T)/6 \\ -2 w_p^3 T^2 + a_n w_p^2 T \\ w_p^3 T \end{bmatrix}. \tag{3.44}$$

Wiener filter

A WF computes a statistical estimate of $\hat{\theta}_k$ of the input signal θ_k which is corrupted by additive noise v_k in the sense of minimizing $E[(\bar{\theta}_k - \hat{\theta}_k)^2]$ [18, 32]. A WF transfer function is obtained by spectral factorization of the auto-correlation functions $S_{\bar{\theta}}$ and S_θ of discrete signal $\bar{\theta}_k$ and θ_k in z-domain.

$$S_\theta(z) = Y(z) Y\left(z^{-1}\right) \tag{3.45}$$

$$H_{WF}(z) = \frac{\hat{\theta}_k}{\theta_k} = \frac{\left[\frac{S_{\bar{\theta}}(z)}{Y(z^{-1})}\right]_+}{Y(z)} \tag{3.46}$$

where $[]_+$ represents the part of the partial fraction expansion of its argument whose poles are inside the unit circle [32]. Appendix A shows the derivation of the second- and third-order WF transfer functions based on this process:

$$H_{WF2}(z) = \frac{(2 - z_0 - z_1) z + z_0 z_1 - 1}{z^2 - (z_0 + z_1) z + z_0 z_1} \tag{3.47}$$

$$H_{WF3}(z) = \frac{(3 - z_0 - z_1 - z_2) z^2 + (z_0 z_1 + z_0 z_2 + z_1 z_2 - 3) z + 1 - z_0 z_1 z_2}{z^3 + (-z_0 - z_1 - z_2) z^2 + (z_0 z_1 + z_0 z_2 + z_1 z_2) z - z_0 z_1 z_2} \tag{3.48}$$

where z_0, z_1 and z_2 are determined by the signal and noise characteristics, and their expressions can be found in Appendix A.

Comparing (3.47) and (3.48) with the closed-loop transfer functions of the state feedback tracking loop in equations (3.37) and (3.38), the estimator gain matrix $\mathbf{L}$ for the 2-state and 3-state state phase tracking loops respectively can be obtained as:

$$\mathbf{L}_{WF2} = \begin{bmatrix} \alpha \\ \beta \end{bmatrix} = \begin{bmatrix} \frac{1+z_0+z_1-3z_0z_1}{2} \\ \frac{(1-z_0)(1-z_1)}{T} \end{bmatrix} \tag{3.49}$$

$$\mathbf{L}_{WF3} = \begin{bmatrix} \alpha \\ \beta \\ \gamma \end{bmatrix} = \begin{bmatrix} \frac{(z_0+z_1+z_2)+2(z_0z_1+z_0z_2+z_1z_2)+2-11z_0z_1z_2}{6} \\ \frac{1-(z_0z_1+z_0z_2+z_1z_2)+2z_0z_1z_2}{T} \\ \frac{1+(z_0z_1+z_0z_2+z_1z_2)-z_0z_1z_2-(z_0+z_1+z_2)}{T^2} \end{bmatrix}. \tag{3.50}$$

Kalman filter

A KF estimates the error state $\Delta\hat{\mathbf{x}}_k$ based on the given measurement $\Delta\theta_k$. A KF estimator should be independent of the controller and its matrix $\mathbf{L}$ should minimize the quadratic form $\chi^{\mathrm{T}} E\left[\left(\Delta\mathbf{x}_k - \Delta\hat{\mathbf{x}}_k\right)\left(\Delta\mathbf{x}_k - \Delta\hat{\mathbf{x}}_k\right)^{\mathrm{T}}\right]\chi$, where χ is an arbitrary $n \times 1$ vector. Referring to the error state model in equation (3.20), the measurement model in equation (3.17), and also the state estimator in equation (3.23), the estimation error can be obtained as:

$$\varepsilon_{k+1} = \Delta\mathbf{x}_k - \Delta\hat{\mathbf{x}}_k = \left(\mathbf{I} - \mathbf{L}_{k+1}\mathbf{H}_P\right)\mathbf{A}_P\varepsilon_k + \left(\mathbf{I} - \mathbf{L}_{k+1}\mathbf{H}_P\right)\mathbf{n}_k - \mathbf{L}_{k+1}\mathbf{v}_{k+1}. \tag{3.51}$$

The error state estimation error's covariance matrix $\mathbf{W}_{k+1} = E\left[\varepsilon_{k+1}{\varepsilon_{k+1}}^{\mathrm{T}}\right]$ is:

$$\mathbf{W}_{k+1} = \left(\mathbf{I} - \mathbf{L}_{k+1}\mathbf{H}_P\right)\left(\mathbf{A}_P\mathbf{W}_k\mathbf{A}_P^{\mathrm{T}} + \mathbf{Q}_P\right)\left(\mathbf{I} - \mathbf{L}_{k+1}\mathbf{H}_P\right)^{\mathrm{T}} + \mathbf{L}_{k+1}\mathbf{R}\mathbf{L}_{k+1}^{\mathrm{T}}. \tag{3.52}$$

Defining

$$\mathbf{N}_{k+1} = \mathbf{A}_P\mathbf{W}_k\mathbf{A}_P^{\mathrm{T}} + \mathbf{Q}_P \tag{3.53}$$

and expanding equation (3.52), we have:

$$\mathbf{W}_{k+1} = \mathbf{N}_{k+1} + \mathbf{U}_{k+1}\left(\mathbf{R} + \mathbf{H}_P\mathbf{N}_{k+1}\mathbf{H}_P^{\mathrm{T}}\right)\mathbf{U}_{k+1}^{\mathrm{T}} - \mathbf{N}_{k+1}\mathbf{H}_P^{\mathrm{T}}\left(\mathbf{R} + \mathbf{H}_P\mathbf{N}_{k+1}\mathbf{H}_P^{\mathrm{T}}\right)^{-1}\mathbf{H}_P\mathbf{N}_{k+1} \tag{3.54}$$

where

$$\mathbf{U}_{k+1} = \mathbf{L}_{k+1} - \mathbf{N}_{k+1}\mathbf{H}_P^{\mathrm{T}}\left(\mathbf{R} + \mathbf{H}_P\mathbf{N}_{k+1}\mathbf{H}_P^{\mathrm{T}}\right)^{-1}\mathbf{H}_P\mathbf{N}_{k+1}. \tag{3.55}$$

Hence the quadratic form $\chi^{\mathrm{T}}\mathbf{W}_{k+1}\chi$ is a minimum when $\mathbf{U}_{k+1} = 0$. Thus, KF gain matrix can be obtained as:

$$\mathbf{L}_{k+1} = \mathbf{N}_{k+1}\mathbf{H}_P^{\mathrm{T}}\left(\mathbf{R} + \mathbf{H}_P\mathbf{N}_{k+1}\mathbf{H}_P^{\mathrm{T}}\right)^{-1} \tag{3.56}$$

and the corresponding $\mathbf{W}_{k+1}$ is:

$$\mathbf{W}_{k+1} = \left(\mathbf{I} - \mathbf{L}_{k+1}\mathbf{H}_P\right)\mathbf{N}_{k+1}. \tag{3.57}$$

The above analysis shows that the KF gain $\mathbf{L}_{k+1}$ is the the gain matrix that minimizes $\chi^{\mathrm{T}}\mathbf{W}_{k+1}\chi$ regardless of the matrices $\mathbf{B}$, $\mathbf{K}$ and the controller $\mathbf{u_k}$. However, the error state estimator is only a subsystem of the control system, see Fig.3.1. To obtain the performance of the overall closed system with this error state estimator, we apply $\mathbf{B} = \mathbf{I}$, $\mathbf{K} = \mathbf{A}_P$ and $\mathbf{u}_k = \mathbf{K}\Delta\hat{\mathbf{x}}_k$ into equation (3.19):

$$\hat{\mathbf{x}}_{k+1} = \mathbf{A}_P\hat{\mathbf{x}}_k + \mathbf{A}_P\Delta\hat{\mathbf{x}}_k. \tag{3.58}$$

The full state estimation variance can be derived from (3.1) and (3.58):

$$E\left[\left(\mathbf{x}_{k+1} - \hat{\mathbf{x}}_{k+1}\right)\left(\mathbf{x}_{k+1} - \hat{\mathbf{x}}_{k+1}\right)^{\mathrm{T}}\right] = \mathbf{A}_P\mathbf{W}_k\mathbf{A}_P^{\mathrm{T}} + \mathbf{Q}_P = \mathbf{N}_{k+1}. \tag{3.59}$$

Equation (3.59) shows that a minimal $\mathbf{W}_k$ corresponds to a minimal quadratic form $\chi^{\mathrm{T}}E\left[\left(\mathbf{x}_{k+1} - \hat{\mathbf{x}}_{k+1}\right)\left(\mathbf{x}_{k+1} - \hat{\mathbf{x}}_{k+1}\right)^{\mathrm{T}}\right]\chi$; therefore the gain matrix $\mathbf{L}_{k+1}$ in equation (3.56) not only minimizes the error state estimation errors but also the full state estimation errors. Since χ is an arbitrary $n \times 1$ vector, we may choose $\chi = \mathbf{H}_P^{\mathrm{T}}$:

$$\begin{aligned}\chi^{\mathrm{T}}E\left[\left(\mathbf{x}_{k+1} - \hat{\mathbf{x}}_{k+1}\right)\left(\mathbf{x}_{k+1} - \hat{\mathbf{x}}_{k+1}\right)^{\mathrm{T}}\right]\chi &= \mathbf{H}_P E\left[\left(\mathbf{x}_{k+1} - \hat{\mathbf{x}}_{k+1}\right)\left(\mathbf{x}_{k+1} - \hat{\mathbf{x}}_{k+1}\right)^{\mathrm{T}}\right]\mathbf{H}_P^{\mathrm{T}} \\ &= E[(\bar{\theta}_k - \hat{\theta}_k)^2].\end{aligned} \tag{3.60}$$

As a result, with $\mathbf{B} = \mathbf{I}$, $\mathbf{K} = \mathbf{A}_P$, and $\mathbf{u}_k = \mathbf{K}\Delta\hat{\mathbf{x}}_k$ and the KF gain matrix $\mathbf{L}_{k+1}$, the overall closed phase tracking loop operates at the MMSE tracking performance.

In the KF implementation, the gain update process is operated in two stages; namely, the transient and the steady-state stage. Given an initial error covariance matrix $\mathbf{W}_0$, $\mathbf{L}_{k+1}$ will converge to the constant optimal gain matrix as the system transits from the transient-state to the steady-state. Letting $\mathbf{L}_{KF} = \lim_{k\to\infty}\mathbf{L}_{k+1}$ denotes the steady-state KF gain. To obtain $\mathbf{L}_{KF}$, we first solve the following discrete algebraic Riccati equation (DARE) to get

the steady-state covariance matrix $\mathbf{N}_\infty$

$$\mathbf{A}_P\mathbf{N}_\infty\mathbf{A}_P^{\mathrm{T}} - \mathbf{A}_P\mathbf{N}_\infty\mathbf{H}_P^{\mathrm{T}}\big(\mathbf{H}_P\mathbf{N}_\infty\mathbf{H}_P^{\mathrm{T}} + \mathbf{R}\big)^{-1}\mathbf{H}_P\mathbf{N}_\infty\mathbf{A}_P^{\mathrm{T}} + \mathbf{Q}_P - \mathbf{N}_\infty = 0. \tag{3.61}$$

Substituting $\mathbf{N}_\infty$ into equation (3.56), we obtain the numerical solutions of $\mathbf{L}_{KF}$.

Discussions and analysis

The gain matrix for PIF, WF, and KF provides a powerful analysis tool for their corresponding designs and performances. In the PIF design, the values of $\mathbf{L}_{PIF}$ in equations (3.43) and (3.44) are primarily determined by the values of BN and T as shown in Table 2.1. Adjusting the value of BN is the most effective way to obtain the desired performance for nominal signal tracking, i.e., increasing BN allows fast convergence in the transient-state and decreasing BN achieves better tracking accuracy in the steady-state. For weak signal tracking, the value of T should be increased to compensate for the power loss through coherent or non-coherent accumulations [4, 34]; in this case the value of BN should also be adjusted accordingly. In practice, the values of BN and T are typically chosen based on the empirical guidelines which do not provide rigorous analysis under different signal conditions.

In the WF design, $\mathbf{L}_{WF}$ is a function of the characteristic roots as shown in equations (3.49) and (3.50), where the locations of these roots are uniquely determined by the signal and noise characteristics. Since the value of $\mathbf{L}_{WF}$ is related to the signal model, with this optimal gain, the WF-based tracking loop could achieve MMSE tracking performance in the steady-state by design, which is superior compared to the heuristic nature of the PIF-based tracking loop.

In the KF design, $\mathbf{L}_{KF}$ is calculated from an iterative operation and determined by the system characteristic matrices $\mathbf{A}_P$, $\mathbf{H}_P$, $\mathbf{Q}_P$ and $\mathbf{R}$. With this gain the KF-based tracking loop could achieve the MMSE performance with both the error state and full state estimation.

Since WF and KF both generate estimations to minimize $E[(\bar{\theta}_k - \hat{\theta}_k)^2]$ under the assumption of white Gaussian noise in the time-invariant linear systems, is it possible that $\mathbf{L}_{WF}$ and $\mathbf{L}_{KF}$ are equivalent? If they are, then we may use $\mathbf{L}_{WF}$ as the closed form representation of steady-state $\mathbf{L}_{KF}$. To investigate the relationship between $\mathbf{L}_{WF}$ and $\mathbf{L}_{KF}$ and the impact of the systematic characteristic matrices $\mathbf{A}_P$, $\mathbf{H}_P$, $\mathbf{Q}_P$ and $\mathbf{R}$ on the gain matrices $\mathbf{L}_{WF}$ and $\mathbf{L}_{KF}$, we compare the analytical solutions of $\mathbf{L}_{WF}$ with numerical solutions

of $\mathbf{L}_{KF}$ under various settings. In all calculations, we set $C/N_0 = 14$dB-Hz and assume that either the data have been wiped off on the data channel or the pilot channel signals are used. The integration time T varies from 1ms to 1000ms. The LQO and HQO are considered and several values of the dynamic parameter q_a, i.e., $q_a = 0m^2/s^5$, $q_a = 0.1m^2/s^5$, and $q_a = 10m^2/s^5$ are used to represent the static, low dynamic, and high dynamic scenarios, respectively. The numerical solutions for $\mathbf{L}_{KF}$ (circles) and the analytical solutions (lines) for $\mathbf{L}_{WF}$ are plotted and depicted in Fig. 3.3 to Fig. 3.5.

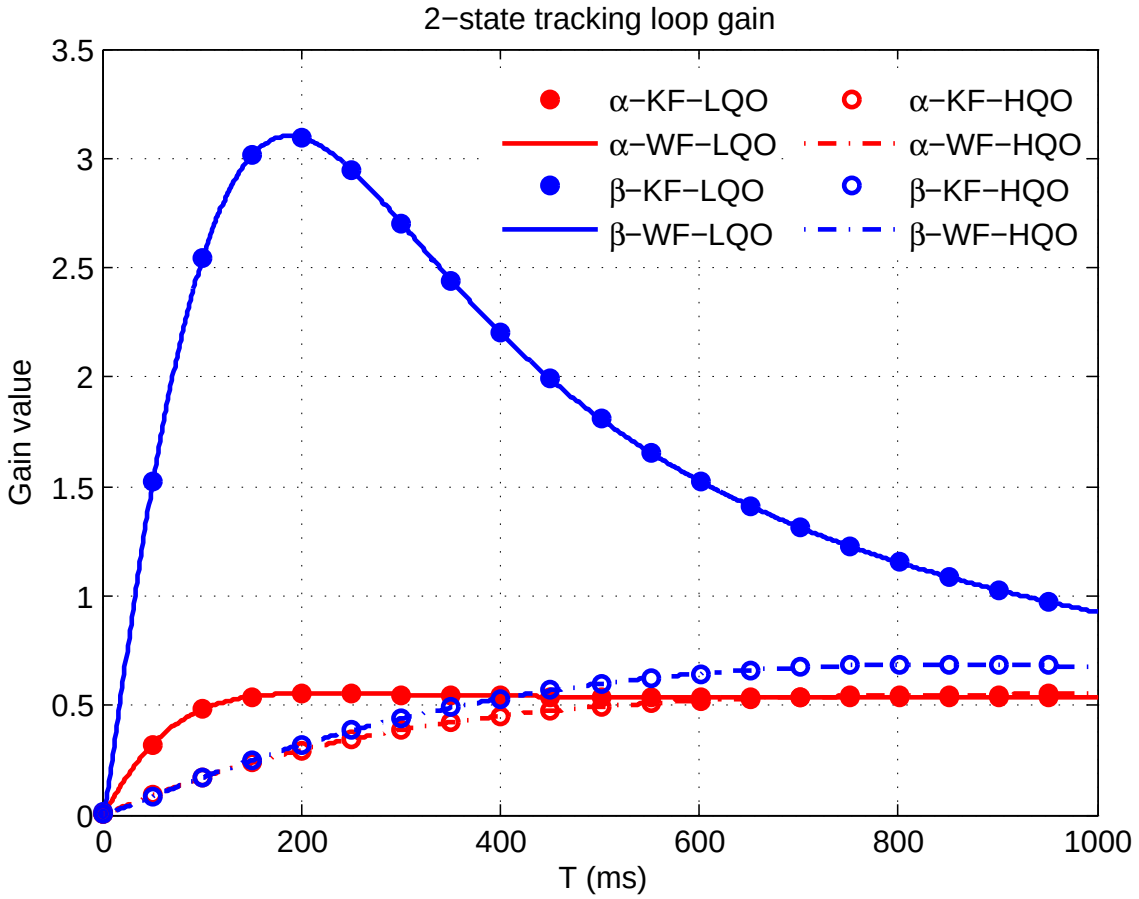

Figure 3.3: The variations of α and β in $\mathbf{L}_{KF}$ and $\mathbf{L}_{WF}$ for different integration times and oscillator qualities in a 2-state phase tracking loop under static conditions.

1). The values of $\mathbf{L}_{WF}$ perfectly match with those of $\mathbf{L}_{KF}$, demonstrating that the analytic expressions of the derived $\mathbf{L}_{WF}$ indeed mirrors the $\mathbf{L}_{KF}$ behavior. This confirms

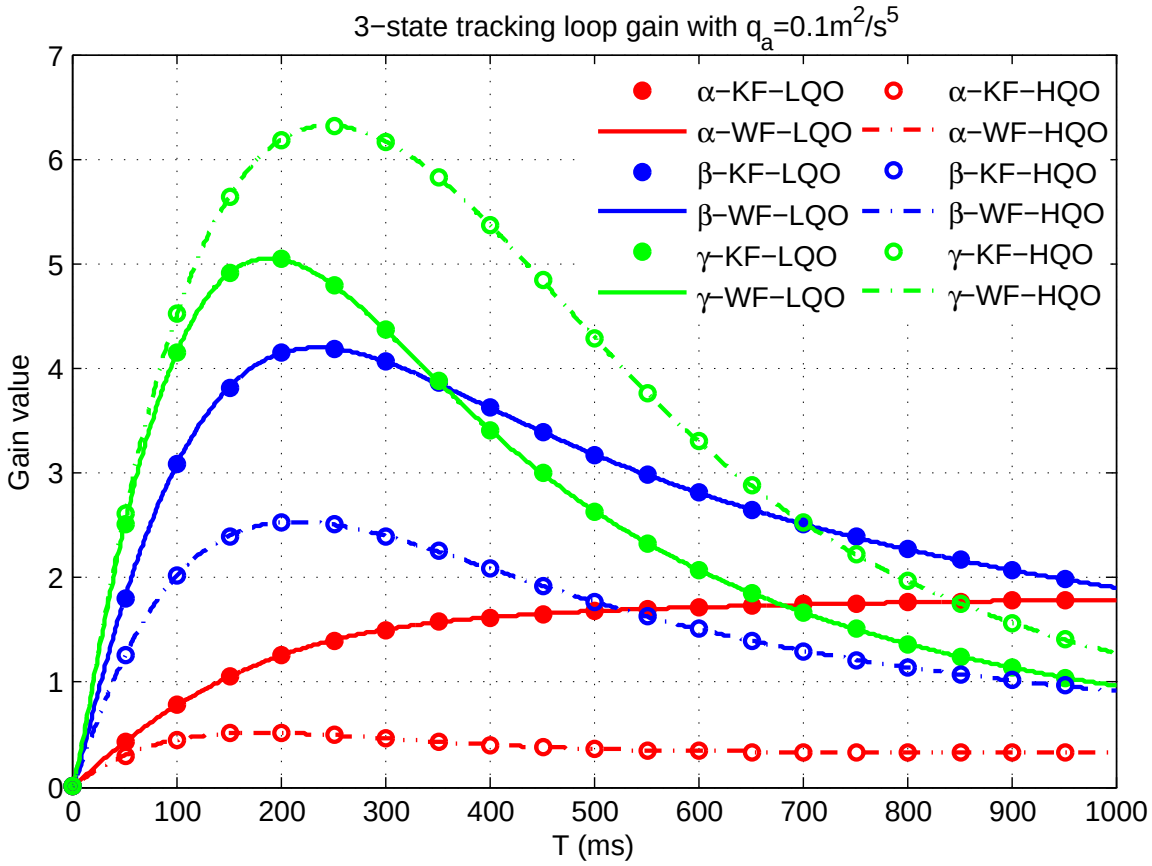

Figure 3.4: The variations of α, β, and γ in $\mathbf{L}_{KF}$ and $\mathbf{L}_{WF}$ for different integration time and oscillator qualities in a 3-state phase tracking loop under low dynamic conditions when $q_a = 0.1m^2/s^5$.

that WF and KF are equivalent under the white Gaussian noise assumption in a time-invariant linear system.

2). From the perspective of system noise, the values of α and β are higher for the receiver with LQO than those with HQO. This indicates that the system modelling error with a good quality oscillator is smaller than that of a poor quality oscillator. Therefore, more weight should be given to estimation from system prediction for receivers with HQOs.

3). From the perspective of measurement noise, increasing the value of T effectively reduces the measurement noise especially when the signal is weak. However, there is a limit to the effective range of T values. The figures show that as T increases from 1ms to 100ms, the loop gain parameters values are increased monotonically. For T >200 ms,

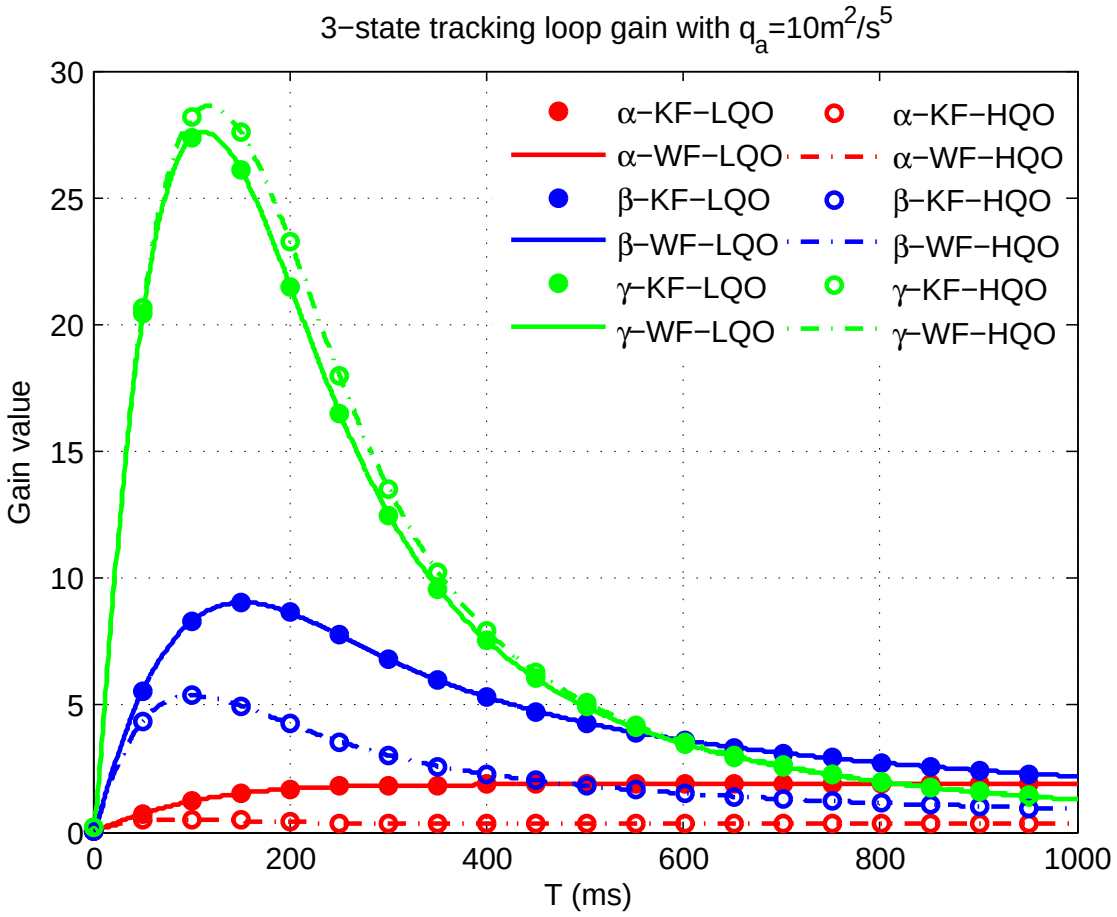

Figure 3.5: The variations of α, β, and γ in $\mathbf{L}_{KF}$ and $\mathbf{L}_{WF}$ for different integration time and oscillator qualities in a 3-state phase tracking loop under high dynamic conditions when $q_a = 10m^2/s^5$.

the gain parameters subsequently decreases before reaching a steady level. Therefore, the filter gain and the integration time are not always positively correlated. Moreover, long time integration will cause some problems. For example, the oscillator phase noise is accumulated with a longer integration time and the small errors of frequency estimation may lead to the signal correlation loss. Hence, it is better to combine an appropriate integration time with a well-designed filter to achieve equivalent or better tracking performance.

4). From the perspective of signal dynamics, the dynamic parameter q_a has a greater influence on the value of γ in $\mathbf{L}_{WF}$ and $\mathbf{L}_{KF}$. From Fig.3.4 and Fig.3.5, it can be observed that the value of γ increases drastically as q_a increases, while the values of α and β are less

affected. For the special case $q_a = 0m^2/s^5$, comparison of the $\mathbf{Q}_P$ matrix in equations (3.7) and (3.8), shows that the 3-state model degrades to the 2-state model when $\gamma = 0$. Hence, γ determines the ability of the filter to track dynamic signals. For the static scenario shown in Fig.3.3, the value of α reaches its steady state level when T is about 600ms for a receiver with HQO, while for a receiver with LQO, α reaches its steady state level when T is about 100ms. The reason is that increasing T in the receiver with LQO is not as effective as that of HQO due to the larger oscillator noise. While the opposite cases are presented in the dynamic scenarios as shown in Fig.3.4 and Fig.3.5, indicating that the receivers with HQO are more sensitivity to platform dynamics than that with LQO.

3.4 Closed Form Performance Indicators and Performance Analysis

In this section, the closed form expressions of phase tracking loop performance indicators in terms of error covariance and mean error for the state feedback/state estimator representation of carrier tracking loops are derived. The tracking performance of the different tracking designs, (i.e., PIF, WF and KF designs) under various operating situations, with varying signal strength, platform dynamics, and oscillator qualities will be compared and analyzed. In addition, the 3-sigma phase error rule will be applied to characterize the admissible range of the loop parameters for tracking loop design implementation.

3.4.1 Tracking Performance Indicators

The most frequently used performance indicators for the GNSS applications are the expectation and the variance of the state estimation errors. In this section, we derive closed-form expressions of the corresponding performance indicators for the phase tracking loop with $\mathbf{B} = \mathbf{I}$, $\mathbf{K} = \mathbf{A}_P$, and different gain matrix representations of PIF, WF, and KF implementations.

Tracking error variance

Denote $\mathbf{P}_{k+1}$ as the tracking error covariance matrix at the $(k+1)^{th}$ epoch:

$$\mathbf{P}_{k+1} = E\left[\left(\mathbf{x}_{k+1} - \hat{\mathbf{x}}_{k+1}\right)\left(\mathbf{x}_{k+1} - \hat{\mathbf{x}}_{k+1}\right)^{\mathrm{T}}\right]. \tag{3.62}$$

Substituting the received and local generated signal in equations (3.1) and (3.33) into (3.62), we have

$$\mathbf{P}_{k+1} = \mathbf{A}_P \left(\mathbf{I} - \mathbf{L}\mathbf{H}_P\right) \mathbf{P}_k (\mathbf{I} - \mathbf{L}\mathbf{H}_P)^{\mathrm{T}} \mathbf{A}_P^{\mathrm{T}} + \mathbf{Q}_P + \mathbf{A}_P \mathbf{L}\mathbf{R}(\mathbf{A}_P \mathbf{L})^{\mathrm{T}} \tag{3.63}$$

When k approaches infinity, the system reaches the steady-state, $\mathbf{P}_{k+1} = \mathbf{P}_k$. Denoting the steady-state error covariance as $\mathbf{P}_X$, for a given estimator gain matrix $\mathbf{L}$, the closed-form expression of $\mathbf{P}_X$ can be obtained by solving equation (3.63). $\mathbf{L}$ can be $\mathbf{L}_{PIF}$, $\mathbf{L}_{WF}$ and $\mathbf{L}_{KF}$, and the corresponding $\mathbf{P}_X$ is denoted as $\mathbf{P}_{PIF}$, $\mathbf{P}_{WF}$ and $\mathbf{P}_{KF}$, can be obtained accordingly. Note that $\mathbf{L}_{WF}$ is equivalent to $\mathbf{L}_{KF}$, and $\mathbf{P}_{WF}$ is identical to $\mathbf{P}_{KF}$ which converges to $\mathbf{N}_\infty$ (see equation (3.59)). For the 3-state tracking model, the main diagonal elements $\mathbf{P}_X$ represent the instantaneous estimation error for initial carrier phase, frequency, and frequency rate, respectively. The remaining elements of $\mathbf{P}_X$ denote the error covariance between the state variables. The error variance of the overall average phase over an integration time T can be obtained as

$$\mathbf{p}_{\bar{\theta}} = E\left[\left(\bar{\theta}_{k+1} - \hat{\theta}_{k+1}\right)^2\right] = \mathbf{H}_P E\left[\left(\mathbf{x}_{k+1} - \hat{\mathbf{x}}_{k+1}\right)\left(\mathbf{x}_{k+1} - \hat{\mathbf{x}}_{k+1}\right)^{\mathrm{T}}\right] \mathbf{H}_P^{\mathrm{T}} = \mathbf{H}_P \mathbf{P}_X \mathbf{H}_P^{\mathrm{T}}. \tag{3.64}$$

Substituting equation (3.63) into (3.64), it can be seen that $\mathbf{p}_{\bar{\theta}}$ is related to system characteristics, such as oscillator error, platform dynamics, signal C/N_0, and signal frequency f_L. Equation (3.64) also provides a quantitative relationship between the phase tracking accuracy and design parameters, such as T or BN (if $\mathbf{L}_{PIF}$ is adopted).

Dynamic stress steady-state error

When the receiver platform acceleration $a_k \neq 0 m/s^2$, a steady-state error will occur in the 2-state phase tracking loop. Similarly, when the receiver platform jerk $j_k \neq 0 m/s^3$, a steady-state error will occur in the 3-state phase tracking loop. Here, we derived the dynamic stress error in the phase tracking loops for the dynamic scenarios having constant acceleration or constant jerk. To reflect this dynamic, we add an input dynamic vector [72] to the system model and obtain:

$$\mathbf{x}_{k+1} = \mathbf{A}\mathbf{x}_k + \mathbf{n}_k + \mathbf{M}\mathbf{d}_k \tag{3.65}$$

where $\mathbf{d}_k$ represents the platform LOS acceleration a_k in the 2-state phase tracking loop or LOS jerk j_k in the 3-state phase tracking loop [72]

$$2-state:\mathbf{d}_k=a_k(m/s^2) \tag{3.66}$$

$$3-state:\mathbf{d}_k=j_k(m/s^3). \tag{3.67}$$

$\mathbf{M}$ is an operator that maps the dynamic input vector $\mathbf{d}_k$ to the state vector, $\mathbf{M}$ for phase tracking has the corresponding forms:

$$2-state:\mathbf{M}_P=\left[\begin{array}{cc}\frac{2\pi f_L}{c}\frac{T^2}{2} & \frac{2\pi f_L T}{c}\end{array}\right]^{\mathrm{T}} \tag{3.68}$$

$$3-state:\mathbf{M}_P=\left[\begin{array}{ccc}\frac{2\pi f_L}{c}\frac{T^3}{6} & \frac{2\pi f_L}{c}\frac{T^2}{2} & \frac{2\pi f_L T}{c}\end{array}\right]^{\mathrm{T}}. \tag{3.69}$$

Thus the average state error at $(k+1)^{th}$ epoch can be expressed as

$$E\left(\mathbf{x}_{k+1}-\hat{\mathbf{x}}_{k+1}\right)=\mathbf{A}_P\left(\mathbf{I}-\mathbf{L}\mathbf{H}_P\right)E\left(\mathbf{x}_k-\hat{\mathbf{x}}_k\right)+\mathbf{M}_P\mathbf{d}_k. \tag{3.70}$$

Denoting $\mathbf{e}_X=\lim_{k\to\infty}E\left(\mathbf{x}_{k+1}-\hat{\mathbf{x}}_{k+1}\right)$ as the steady-state error, we have

$$\mathbf{e}_X=\left[\mathbf{I}-\mathbf{A}_P\left(\mathbf{I}-\mathbf{L}\mathbf{H}_P\right)\right]^{-1}\mathbf{M}_P\mathbf{d}_k. \tag{3.71}$$

The steady-state dynamic stress phase error can be expressed as

$$\mathbf{e}_{\bar{\theta}}=\lim_{k\to\infty}E\left(\bar{\theta}_{k+1}-\hat{\theta}_{k+1}\right)=\mathbf{H}_P e_X=\mathbf{H}_P[\mathbf{I}-\mathbf{A}_P\left(\mathbf{I}-\mathbf{L}\mathbf{H}_P\right)]^{-1}\mathbf{M}_P\mathbf{d}_k \tag{3.72}$$

It can be seen that $\mathbf{e}_{\bar{\theta}}$ is related to platform dynamics. Equation (3.72) also provides the quantitative relationship between the dynamic stress error and design parameters, such as T or BN (if $\mathbf{L}_{PIF}$ is adopted).

3.4.2 Performance Analysis

The 3-sigma phase jitter [8] can be expressed as:

$$3\sigma_{PLL}=3\sqrt{\mathbf{p}_{\bar{\theta}}}+\mathbf{e}_{\bar{\theta}} \tag{3.73}$$

In traditional PLL design, a conservative rule of thumb requires that the 3-sigma phase

jitter does not exceed one-fourth of the phase pull-in range of the PLL discriminator [8]. For the two-quadrant arctangent and four-quadrant discriminators in data and pilot channels, the tracking error should satisfy the following conditions respectively [8]:

$$\sigma_{PLL} = \sqrt{\mathbf{p}_{\bar{\theta}}} + \frac{\mathbf{e}_{\bar{\theta}}}{3} \leq 15^\circ \text{ or } 30^\circ. \tag{3.74}$$

We can observe that σ_{PLL} is related to the users' dynamic, signal strength, oscillator quality, and loop parameters. Therefore, to satisfy the above conditions, the loop parameters, should be carefully designed to adapt to different environments to avoid loss of lock.

To compare the performance of these designs and to investigate the admissible range of the loop parameters under the different signal strengths, platform dynamics, and oscillator conditions, the value of σ_{PLL} with a 15° or 30° locked range of the phase tracking loops are plotted in Fig.3.6 to Fig.3.9. In our analysis, the value of C/N_0 is varied from 10dB-Hz to 44dB-Hz and the oscillators are chosen either as LQO or HQO. Several dynamic situations, i.e., $a_k = 0m/s^2$ and $a_k = 1m/s^2$ in the 2-state phase tracking loops, $j_k = 0m/s^3$ and $j_k = 1m/s^3$ in the 3-state phase tracking loops are considered, respectively. Since the navigation data period for GPS L1 signal is 20ms, the integration time used in carrier tracking loop is typically less than 20ms to avoid data bit transition. Here we assume that the data have been wiped off for the data channel or the pilot channel signals are used and the value of T varies from 1ms to 1000ms. The value of $BN \cdot T$ is set at 0.3 in PIF-based phase tracking loop, and the value of q_a is set at $0.1m^2/s^5$ in the 3-state model. The curves in Fig.3.6-3.9 represent the locus of (T,C/N_0) where the tracking error is 15° or 30°. Some conclusions can be drawn from these figures.

i). If there is no dynamic stress error, the 2-state and 3-state phase tracking loop results are shown in Fig.3.6 and Fig.3.7, respectively. For the same C/N_0, the admissible range of T in the receiver with HQO is wider than that of the receiver with LQO, due to the better clock characteristics for all phase tracking loop designs. Furthermore, the 15° and 30° locked range of the tracking loops with $\mathbf{L}_{WF}$ and $\mathbf{L}_{KF}$ are wider than that of the loop with $\mathbf{L}_{PIF}$, since both $\mathbf{L}_{WF}$ and $\mathbf{L}_{KF}$ are the optimal gains in the sense of MMSE, which ensures better tracking accuracy.

ii). If dynamic stress error exists, such as the velocity changes with a rate of $1m/s^2$ in the 2-state phase tracking loop, as shown in Fig.3.8, or the acceleration changes with a rate of $1m/s^3$ in the 3-state phase tracking loop, as shown in Fig.3.9, the admissible range of T

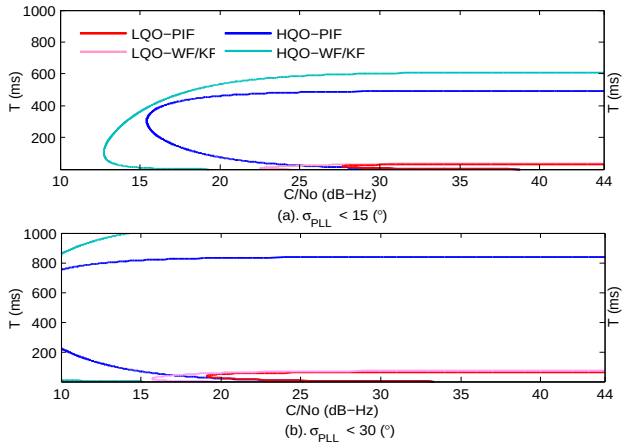

Figure 3.6: σ_{PLL} in 2-state phase tracking loops for various receiver oscillator qualities and tracking loop designs without dynamic stress error ($a = 0m/s^2$)

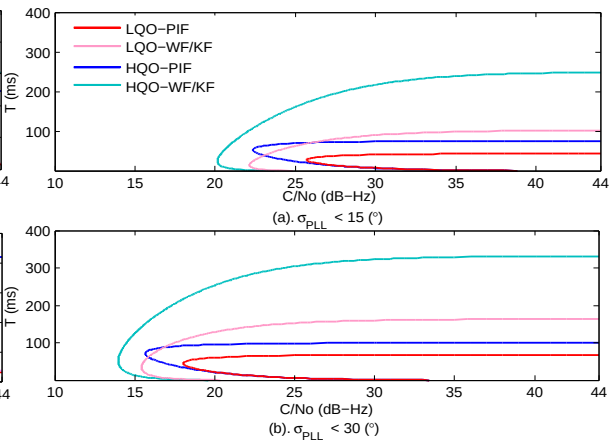

Figure 3.7: σ_{PLL} in 3-state phase tracking loops for various receiver oscillator qualities and tracking loop designs without dynamic stress error ($j = 0m/s^3$)

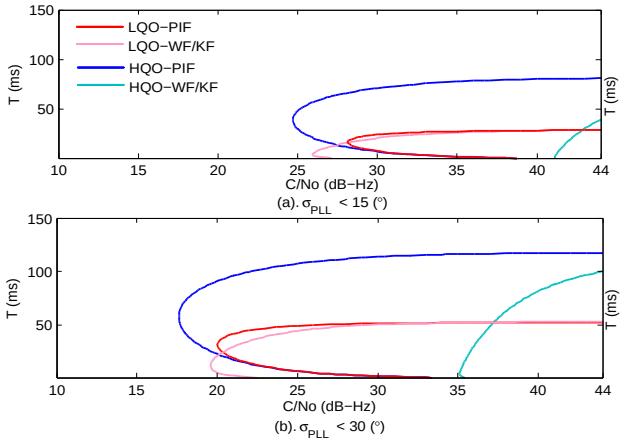

Figure 3.8: σ_{PLL} in 2-state phase tracking loops for various receiver oscillator qualities and tracking loop designs with dynamic stress error ($a = 1m/s^2$)

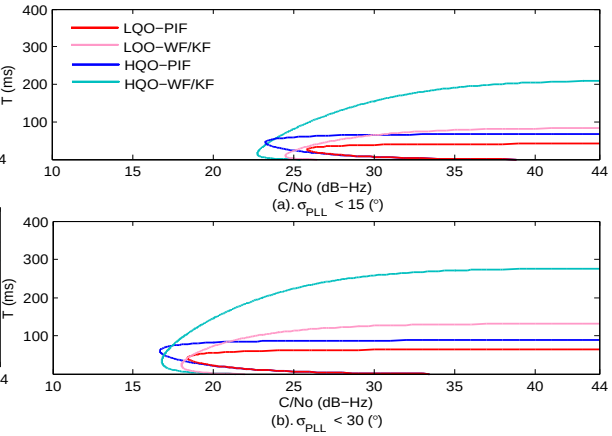

Figure 3.9: σ_{PLL} in 3-state phase tracking loops for various receiver oscillator qualities and tracking loop designs with dynamic stress error ($j = 1m/s^3$)

is decreased, as can be seen by comparing Fig.3.6 and Fig.3.7. This observation indicates that using a shorter integration time may increase the dynamic tracking ability, but at the cost of tracking sensitivity. Additionally, the 15° and 30° locked range of the phase tracking loops with $\mathbf{L}_{WF}$ and $\mathbf{L}_{KF}$ are decreased substantially when dynamic stress error occurs as compared to the loop with $\mathbf{L}_{PIF}$, as can be seen in Fig.3.8 and Fig.3.9. The reason is that PIF uses a model-free approach, where the filter parameters are designed according to the empirical values, but WF/KF is a model-based approach, where the filter is designed according to the system noise characteristic. As such, WF/KF results in a narrower equivalent bandwidth which is able to eliminate the system noise more effectively but at the cost of dynamic adaptability. It is known that the components α and β in $\mathbf{L}_{WF}$ and $\mathbf{L}_{KF}$ are mainly determined by the oscillator characteristic, and γ is mainly determined by the dynamic parameter q_a. Hence, the design of $\mathbf{L}_{WF}$ and $\mathbf{L}_{KF}$ with poor oscillator quality results in large values of α and β. In this case, the tracking loop with LQO parameters is more robust than that of HQO parameters when the dynamic stress error exists, as can be seen in Fig. 3.8. However, a different result arises when γ is introduced in 3-state phase tracking loops with $\mathbf{L}_{WF}$ and $\mathbf{L}_{KF}$, as shown in Fig. 3.9. With almost the same value of γ, the tracking sensitivity of the loop with HQO is higher than that of the receiver with LQO due to the smaller oscillator noise.

In summary, σ_{PLL} in equation (3.74) provide the admissible range of the loop parameters under various operating situations, with varying signal strength, platform dynamics, and oscillator qualities. If $\mathbf{d}_k$ is non-zero, there will be a bias, such as $\mathbf{e}_{\bar{\theta}}$ in phase tracking loop that degrades the tracking performance. To avoid the performance degradation caused by the dynamic stress error, additional state should be included in the state model to account for this unknown constant bias. For example, under the constant acceleration where $\mathbf{d}_k = a_k \neq 0 m/s^2$, there will be a bias in 2-state phase tracking loop, while 3-state phase tracking loop is unbiased because the additional state $\dot{\omega}_k$ is used to estimate this bias. In this thesis, we assume that d_k is zero for simplicity. To further improve the tracking performance, the loop parameters that minimize $\mathbf{p}_{\bar{\theta}}$ will be discussed in the following section.

3.5 Optimization: Minimum Average Phase Tracking Error Variance Criteria

Analysis presented in Section 3.4 shows that the error variance, $\mathbf{p}_{\bar{\theta}}$, is determined by signal strength, platform dynamics, receiver oscillator, and tracking loop gain matrix $\mathbf{L}$. The signal characteristics, which are determined by the external factors, can not be controlled. However, the gain matrix $\mathbf{L}$, is determined by the design specifications, such as the value of integration time T and equivalent noise bandwidth BN (if PIF is adopted), and can be optimized to improve the tracking accuracy. According to the analysis in Section 3.4, the minimum tracking error variance could be achieved if the appropriate value of T is selected for each specified signal strength and dynamics in the phase tracking loops with PIF, WF, and KF designs. Similarly, the optimal value of BN could also be obtained which enables higher tracking accuracy in the PIF-based phase tracking loop. Therefore, the objective in this section is to investigate the optimal parameters that minimize the value of $\mathbf{p}_{\bar{\theta}}$ in three PLL designs employing PIF, WF, and KF for GPS L1 signals.

In the optimization procedure, several typical situations: weak and strong signal strength ($C/N_0 = 10 \sim 44$dB-Hz), low and highly dynamics ($q_a = 0, 0.1, 1, 10, 100, 1000 m^2/s^5$), LQO and HQO effects are considered. The value of T varies from 1ms to 1000ms in PIF-, WF-, and KF-based phase tracking loops and the maximum value of $BN \cdot T$ is set at 0.5 in PIF-based phase tracking loop. Under these given conditions, the optimal values of T, T_{opt}, can be obtained by minimizing $\mathbf{p}_{\bar{\theta}}$ in the PIF-, WF-, and KF-based phase tracking loops accordingly. Besides, the values of BN_{opt} for a PIF-based phase tracking loop can be obtained by dividing the $BN \cdot T$ that minimizes $\mathbf{p}_{\bar{\theta}}$ by T_{opt} as well. With these optimal loop parameters, the minimum phase tracking error variance, $\mathbf{p}_{\bar{\theta}min}$, in these three phase tracking loops could be investigated and compared. The corresponding values of T_{opt}, $\sqrt{\mathbf{p}_{\bar{\theta}min}}$, and BN_{opt} are plotted in Fig. 3.10-3.13 accordingly.

For a static receiver as shown in Fig. 3.10, the phase tracking error is dominated by thermal noise and oscillator noise and T_{opt} should be chosen to balance them. The followings can be observed from Fig. 3.10:

i). The value of T_{opt} increases as the signal C/N_0 decreases especially when the C/N_0 is low.

ii). T_{opt} for the receiver with a HQO is larger than that of the receiver with a LQO. The higher oscillator quality results in a ∼9dB improvement in tracking sensitivity if 15°

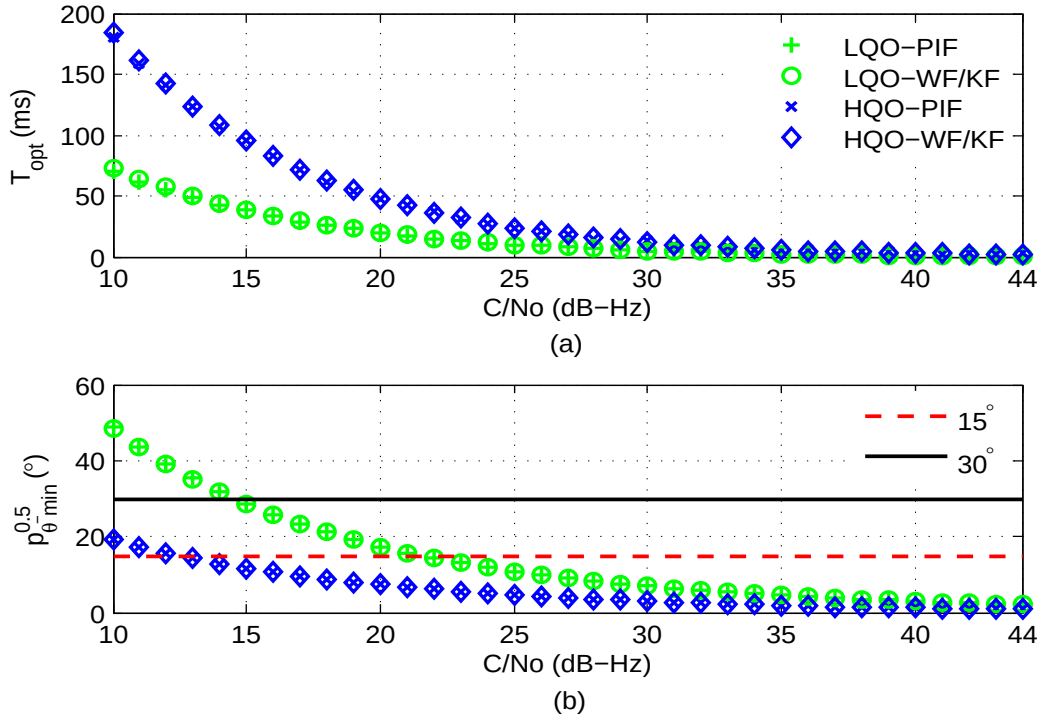

Figure 3.10: T_{opt} and $\sqrt{\mathbf{p}_{\bar{\theta}min}}$ versus C/N_0 for both high and low receiver oscillator qualities for 2-state phase tracking loop with PIF, WF, and KF designs under the static condition.

threshold is used.

iii). For T_{opt} and $\sqrt{\mathbf{p}_{\bar{\theta}min}}$ the difference between PIF- and WF/KF- based phase tracking loops are barely noticeable, which indicates that based on the same cost function, i.e., minimizing $\mathbf{p}_{\bar{\theta}}$, there is only one optimal design regardless of the specific filter design.

For a receiver on a dynamic platform, the effects of oscillator noise are not as significant as for a static receiver, and T_{opt} is chosen to balance the dynamic and the thermal noise effect in phase tracking loop design. Fig. 3.11 and Fig. 3.12 show that:

i). The oscillator noise effect becomes less important when the dynamics is increased. T_{opt} and $\sqrt{\mathbf{p}_{\bar{\theta}min}}$ for receivers with LQO and HQO gradually overlap for both the low and highly dynamic cases, as the C/N_0 decreases.

ii). As the dynamic increases, T_{opt} decreases while $\sqrt{\mathbf{p}_{\bar{\theta}min}}$ increases. In a receiver with HQO at 10dB-Hz signal strength, a WF/KF-based PLL operating with T_{opt} at a ∼80ms could obtain a $\sim 50^{\circ}$ MMSE performance under low dynamic conditions, while under highly

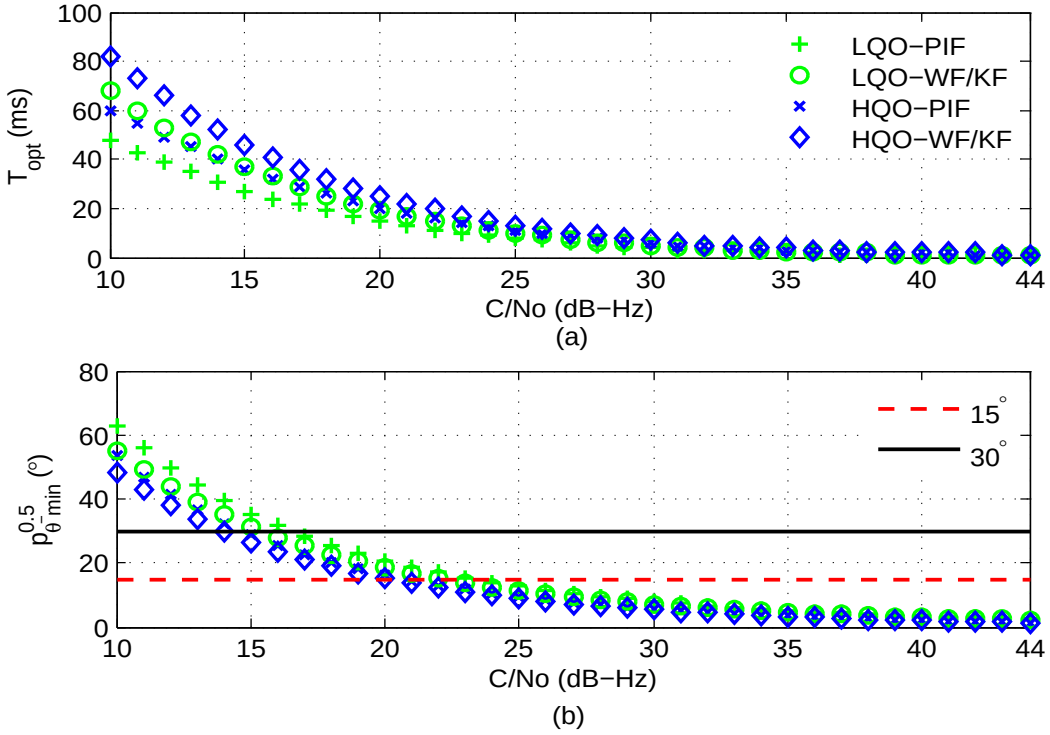

Figure 3.11: T_{opt} and $\sqrt{\mathbf{p}_{\bar{\theta}min}}$ versus C/N_0 for both high and low receiver oscillator qualities for 3-state phase tracking loop with PIF, WF, and KF designs under the low dynamic condition ($q_a = 0.1m^2/s^5$).

Table 3.1: Theoretical PLL tracking sensitivities with thresholds of 15° (data channel) and 30° (pilot channel) values for static, low, and high signal dynamics, both high and low receiver oscillator qualities, and the optimal PIF-, WF-, and KF-based phase tracking loop designs (unit: dB-Hz)

$q_a(m^2/s^5)$	LQO		HQO	
	PIF	WF/KF	PIF	WF/KF
0	22/15	22/15	13/6	13/6
0.1	23/17	23/16	21/15	21/14
1	24/18	23/17	23/17	23/16
10	26/19	25/19	25/19	25/18
100	27/21	27/21	27/21	27/21
1000	29/23	29/22	29/23	29/22

*Note: */* represent the corresponding phase tracking loop sensitivity with respect to 15°/30° threshold;*

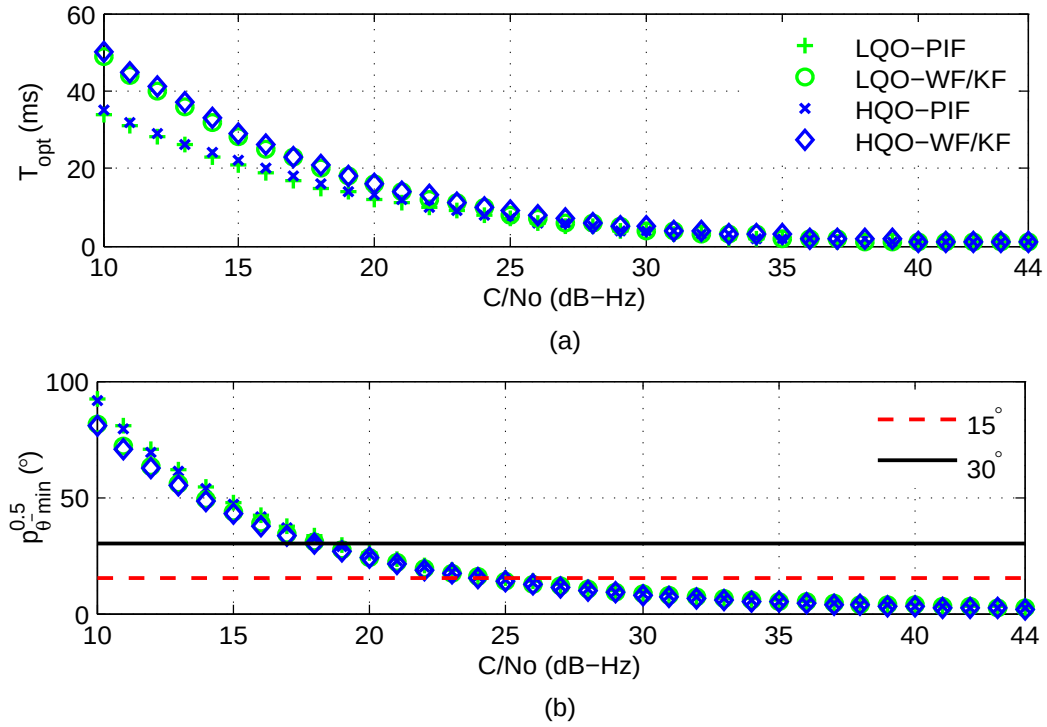

Figure 3.12: T_{opt} and $\sqrt{\mathbf{p}_{\bar{\theta}min}}$ versus C/N_0 for both high and low receiver oscillator qualities for 3-state phase tracking loop with PIF, WF, and KF designs under the highly dynamic condition ($q_a = 10m^2/s^5$).

dynamic conditions T_{opt} is ∼50ms, and the corresponding minimum phase tracking error is $\sim 80^\circ$, indicating that higher dynamic limits integration times, degrades tracking accuracy, as well as tracking sensitivity.

iii). The minimum tracking errors in PIF-based phase tracking loops are slightly larger than that in WF- and KF-based phase tracking loops under both low and highly dynamic conditions. As was discussed in Section 3.3, for $\mathbf{L}_{PIF}$, its components, α, β, and γ, are determined by the values of BN and T, while for $\mathbf{L}_{WF}$ and $\mathbf{L}_{KF}$, their α and β are mainly determined by the oscillator $h-$parameters and T, and γ is determined by q_a and T. The value of γ is coupled with α and β in $\mathbf{L}_{PIF}$, but is independent of α and β in $\mathbf{L}_{WF}$ and $\mathbf{L}_{KF}$. This allows a higher degree of freedom in the WF- and KF-based phase tracking loop designs. Hence, PIF-based phase tracking loop only achieves a sub-optimal performance, while the optimizations of WF- and KF-based phase tracking loops can realize the MMSE performance.

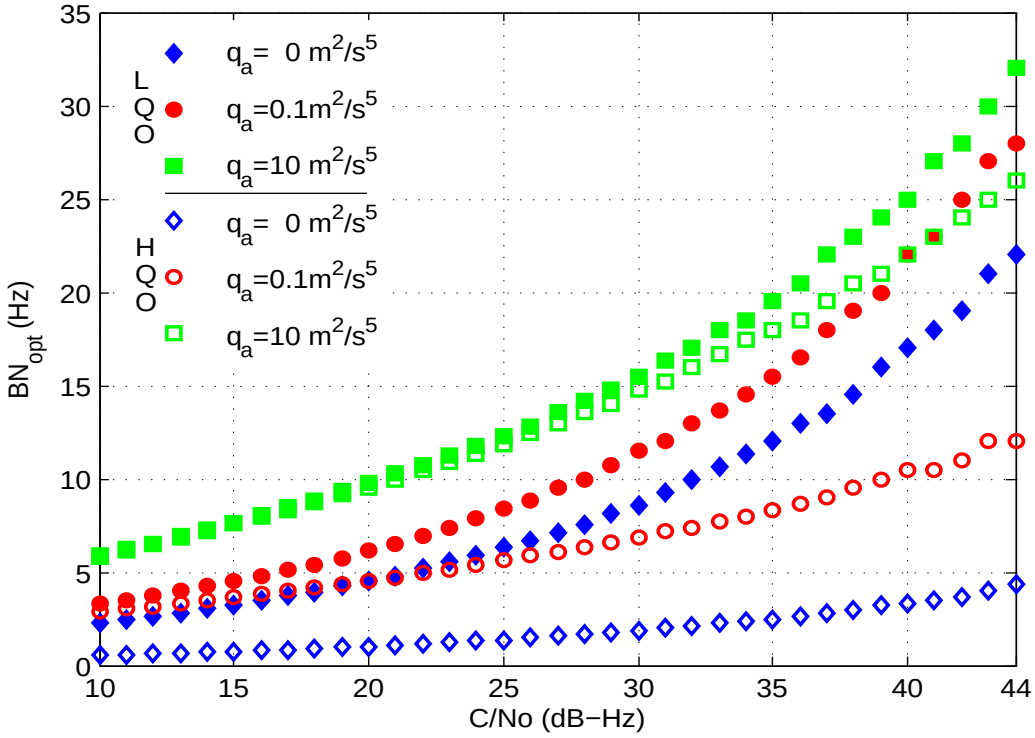

Figure 3.13: BN_{opt} dependency on C/N_0 for static, low, and high signal dynamics, both high and low receiver oscillator qualities in the PIF-based phase tracking loop.

Fig.3.13 shows that:

i). BN_{opt} increases as the signal C/N_0 increases.

ii). BN_{opt} in a receiver with LQO is wider than that in a receiver with HQO.

iii). BN_{opt} increases as receiver dynamics increase. These trends are opposite to that of T_{opt} in Fig.3.10-3.12. This is because for a stronger signal, a shorter integration time is needed, so a larger loop bandwidth can be accommodated to handle the higher dynamics and the larger oscillator noises.

Tracking sensitivity refers to the tracking capability of the weak signal in GNSS receiver. Here, we assume that the tracking loop could maintain lock when the tracking error is below the tracking threshold, such as 15° for data channel and 30° for pilot channel. The tracking sensitivity represents the lowest signal C/N_0 that can be tracked by the phase tracking loops without loss-of-lock. The theoretical tracking sensitivities of the generalized phase tracking loops with optimal loop parameters, i.e., T_{opt} and BN_{opt}, according to the 3-sigma

Table 3.2: T_{opt} and BN_{opt} parameter values for static, low, and high signal dynamics, both high and low receiver oscillator qualities, and PIF-, WF-, and KF-based phase tracking loop designs

$q_a(m^2/s^5)$	Oscillator quality	Tracking loop type	b_1	μ_1	b_2	μ_2
0	Low	PIF	0.257	0.559	1.191	0.288
		WF/KF	0.272	0.567	N/A	
	High	PIF	0.700	0.583	0.313	0.258
		WF/KF	0.719	0.588	N/A	
0.1	Low	PIF	0.166	0.527	1.677	0.278
		WF/KF	0.247	0.555	N/A	
	High	PIF	0.190	0.487	1.981	0.179
		WF/KF	0.279	0.526	N/A	
1	Low	PIF	0.140	0.501	2.212	0.251
		WF/KF	0.211	0.537	N/A	
	High	PIF	0.140	0.473	2.858	0.181
		WF/KF	0.213	0.514	N/A	
10	Low	PIF	0.103	0.467	3.597	0.213
		WF/KF	0.163	0.511	N/A	
	High	PIF	0.104	0.459	4.110	0.183
		WF/KF	0.163	0.502	N/A	
100	Low	PIF	0.076	0.448	5.662	0.193
		WF/KF	0.121	0.492	N/A	
	High	PIF	0.074	0.438	5.910	0.184
		WF/KF	0.124	0.493	N/A	
1000	Low	PIF	0.052	0.416	8.271	0.191
		WF/KF	0.092	0.482	N/A	
	High	PIF	0.052	0.415	8.433	0.187
		WF/KF	0.090	0.473	N/A	

rule are summarized in Table 3.1. The values in Table 3.1 shows that:

i). Under the static scenario ($q_a = 0m^2/s^5$), a phase tracking loop tracking sensitivity mainly depends on the receiver oscillator quality. The theoretical tracking sensitivity for a receiver with a HQO is as low as 13dB-Hz and 6dB-Hz for data channels and pilot channels, respectively, which is $\sim$ 9dB higher than that for a receiver with LQO. These are the theoretical upper bounds of phase tracking loop tracking sensitivity.

ii). Under the dynamic scenario ($q_a \neq 0m^2/s^5$), the influence of oscillator quality

becomes less important as the platform dynamics increases. The tracking sensitivity for a receiver with a LQO is the same as one with a HQO when $q_a > 1m^2/s^5$. The higher the platform dynamics, the worse the tracking sensitivity becomes.

iii). Although a phase tracking loop with $\mathbf{L}_{PIF}$ is suboptimal, it can still achieve nearly the same tracking sensitivity as the ones with $\mathbf{L}_{WF}$ and $\mathbf{L}_{KF}$. This indicates that under the uniform optimization criteria, the phase tracking loop performance is mainly limited by the signal characteristics and receiver hardware quality, such as oscillator quality and platform dynamics, regardless of what filter design is used.

iv). There is a general 6dB to 7dB improvement in pilot channels over data channels. The potential advantages of pilot channels over data channels are not greatly affected by the receiver oscillator quality and platform dynamics, as well as filter designs. These results are consistent with the conclusions in

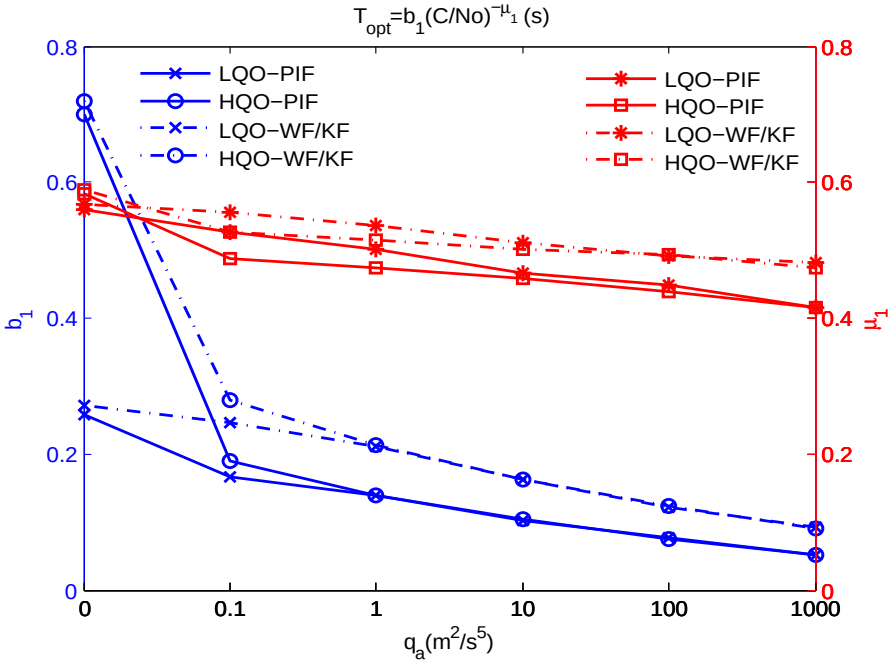

Figure 3.14: Trends of b_1 and μ_1 versus signal dynamics for high and low receiver oscillator quality, and phase tracking loop with PIF, WF, and KF designs.

To calculate the optimal values of T_{opt} and BN_{opt} for various signal scenarios, we obtain the minimum value of $\mathbf{p}_{\bar{\theta}min}$ over the search space of T from 1ms to 1000ms, $BN \cdot T$ from 0.0001 to 0.5, and C/N_0 from 10dB-Hz to 44dB-Hz for each specified dynamics. These

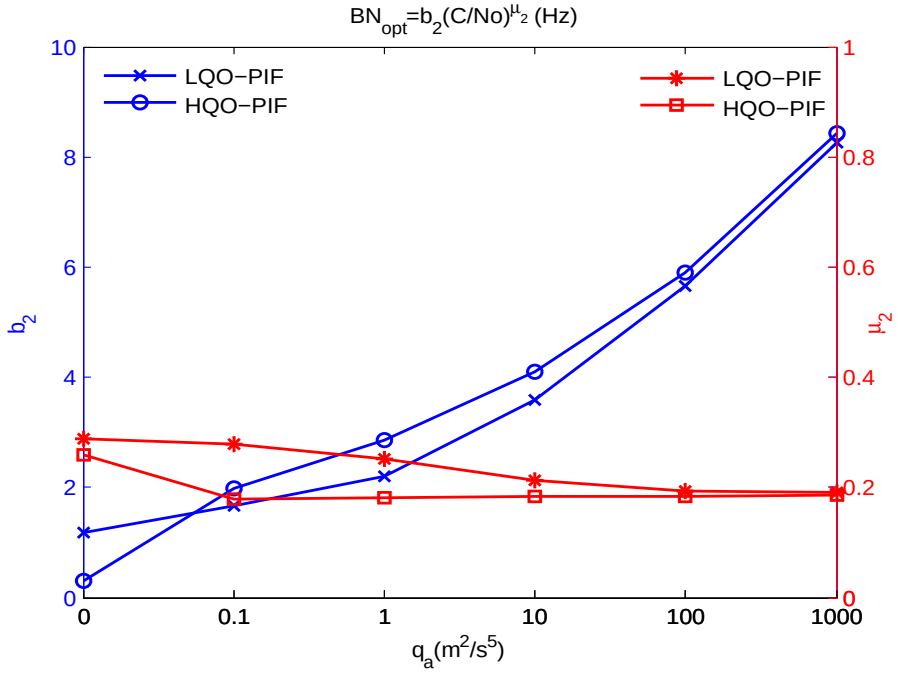

Figure 3.15: Trends of b_2 and μ_2 versus signal dynamics for high and low receiver oscillator qualities in the PIF-based phase tracking loop.

optimal values are uniquely associated with a given set of signal conditions and can be predetermined. Therefore, for practical applications, the relationships between T_{opt} and C/N_0, BN_{opt} and C/N_0 can be established beforehand. Such relationships also provide insights into the influence signal parameters have on the design choices. The relationships can be summarized below:

$$T_{opt} = b_1(C/N_0)^{-\mu_1}(s) \tag{3.75}$$

$$BN_{opt} = b_2(C/N_0)^{\mu_2}(Hz) \tag{3.76}$$

where the parameters b_1, μ_1, b_2, and μ_2 for various signal dynamics, receiver oscillator qualities, and phase tracking loop designs are obtained through curve fitting of numerical calculations and listed in Table 3.2. Fig.3.16 shows an example of curve fitting of T_{opt} versus C/N_0 for $q_a = 1m^2/s^5$ in the receiver with low quality oscillator and WF/KF design. This curve fitting guarantees 95% confidence degree. Equations (3.75) and (3.76) provide the optimal parameter designs in the generalized phase tracking loop under diverse dynamic and weak signal scenarios. To clearly show the trends of these parameters versus different

signal dynamics with various receiver oscillator qualities, and phase tracking loop designs, their values are plotted in Fig.3.14 and Fig.3.15. [8].

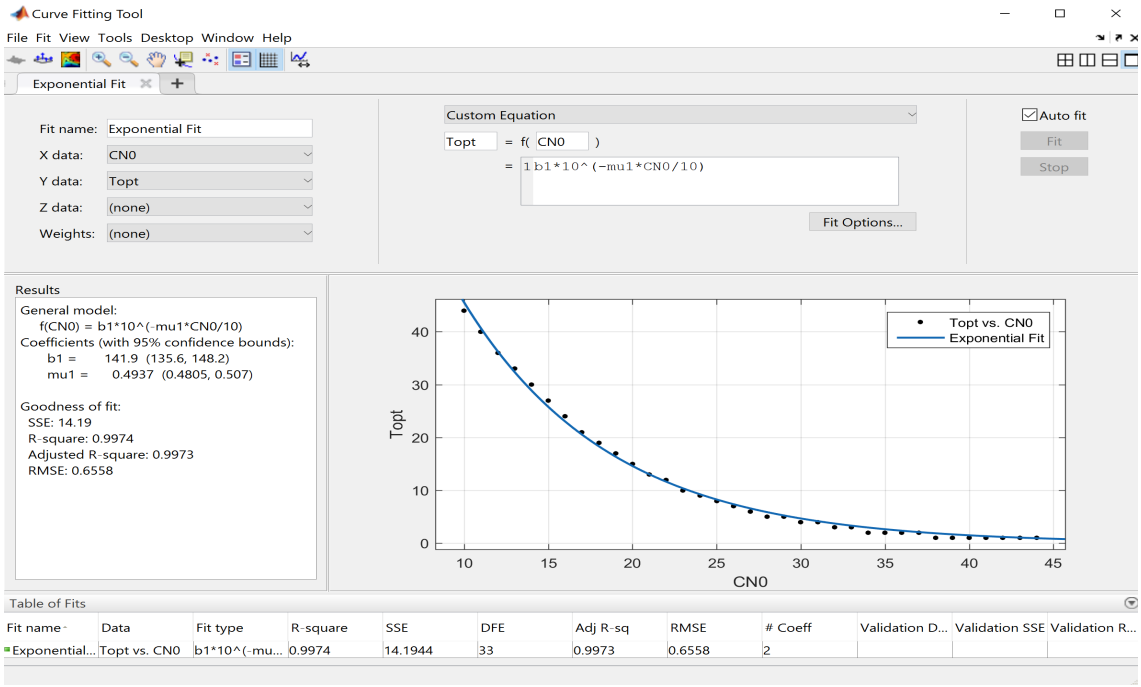

Figure 3.16: Curve fitting example of T_{opt} versus C/N_0 for $q_a = 1m^2/s^5$ in the receiver with low quality oscillator and WF/KF design.

Fig.3.14 shows that as dynamic parameter q_a increases, b_1 and μ_1 will decrease for both LQO and HQO. Fig.3.15 shows that with the increasing of dynamic parameter q_a, there is a slight decline in μ_2, and a sharp rise in b_2. This indicates that the parameter b_2 is more sensitive to the changing signal dynamics. Similarly, the difference between b_2 and μ_2 for low and high oscillator qualities is reduced with increasing signal dynamics.

3.6 Adaptive Phase Tracking Process

The typical phase tracking loops can be classified as a fixed $\mathbf{L}$ and fixed T (FL-FT) algorithm or an adaptive $\mathbf{L}$ and fixed T (AL-FT) algorithm, respectively. The FL-FT approach corresponds to the traditional PIF-based phase tracking loop, where $\mathbf{L}$ is determined by the predefined value of BN and T. The AL-FT approach corresponds to the KF-based phase tracking loop, where $\mathbf{L}$ is adjustable, based on the signal strength's and platform

dynamics estimations, while the value of T is usually predefined and constant. When the signal changes in a real environment, the tracking loop should be flexible enough to respond accordingly, such that the value of T should be increased or decreased when the signal is weak or strong under different dynamic scenarios. Based on the optimization analysis under the assumption of white Gaussian noise, we apply these optimal designs in an adaptive phase tracking loop, where the values of T_{opt} in PIF, WF, and KF and BN_{opt} in PIF are adaptively tuned according to the variation of signal strength and dynamics to achieve the optimal phase tracking loop sensitivity and accuracy.

The proposed adaptive tracking scheme requires knowledge of the signal C/N_0 and dynamic characteristics. C/N_0 can be obtained by using real time signal-to-noise ratio (SNR) estimator at regular intervals [104–106]. A common approach is to utilize averaging times on the order of a navigation data bit, or 20ms to achieve the lowest expected measurable C/N_0 estimates on the order of approximately 17dB-Hz [104]. The dynamics parameter q_a can be estimated directly using receiver measurements or other on-board sensors. Thus, by using this relationship in equation (3.12), we can set the corresponding value of q_a according to the empirical knowledge of the platform's dynamics.

In our proposed adaptive phase tracking algorithm (see Algorithm 1), T and other loop parameters are adaptively tuned according to the estimations of C/N_0 and q_a to achieve optimal tracking loop sensitivity and accuracy. Below is a summary of the processes in Algorithm 1:

Assuming the C/N_0 and q_a are available, the adaptive tracking algorithm can be implemented as follows:

1) Initialization. The tracking loop is initialized with Doppler frequency, carrier phase, and C/N_0 estimation from the acquisition process. In this initial stage, phase tracking loop is operating with a 1ms integration time, and large loop bandwidth values (for example $BN \geq 50$Hz) are adapted to ensure fast convergence to the steady state.

2) Optimal tracking. When the phase tracking loop operates in a steady state, the T_{opt} and BN_{opt} are obtained according to knowledge of C/N_0 and q_a estimations through equations (3.75) and (3.76). The corresponding loop gain $\mathbf{L}_{PIF}/\mathbf{L}_{WF}/\mathbf{L}_{KF}$ are calculated and used to update the state estimations, which are subsequently used to generate T_{opt}ms carrier signals (we assume that the data is wiped off when $T > 1ms$ on data channel) for correlation with new incoming signals, in phase discriminator calculation, and estimating the signal C/N_0 for preparation of the next tracking iteration.

3) Update. The integration time and loop parameters computed from 2) are updated when a new C/N_0 estimation is obtained in each new epoch. Otherwise, the loop parameters are kept unchanged until C/N_0 is updated.

Consequently, the adaptive phase tracking loop adjusts the values of T and $\mathbf{L}$ in an time-varying manner aimed to achieve the theoretical MMSE performance. Noted that in a fading environment, this algorithm may not work if the fading is faster than the C/N_0 estimation time interval.

Algorithm 1 Adaptive phase tracking algorithm

1: **Initialization**:
2: Set $T = 1$ms and calculate the phase error $\Delta\theta_k$ from the phase discriminator once per 1ms;
3: Set $BN = 50Hz$ to make the tracking loop fast convergent to steady-state;
4: Obtain the value of C/N_0 estimation, c/n_0, through the SNR estimator;
5: **Optimal tracking**:
6: Set $T = T_{opt}$, where $T_{opt} = b_1(c/n_0)^{-\mu_1}$;
7: Set $BN = BN_{opt}$, where $BN_{opt} = b_2(c/n_0)^{\mu_2}$ (if PIF is adopted);
8: Calculate the loop gain matrix $\mathbf{L}$, such as $\mathbf{L}_{PIF}$, $\mathbf{L}_{WF}$, and $\mathbf{L}_{KF}$;
9: Calculate the phase error $\Delta\theta_k$ from the phase discriminator once per T_{opt}ms;
10: Estimate the state $\hat{\mathbf{x}}_{k+1} = \mathbf{A}_P\hat{\mathbf{x}}_k + \mathbf{A}_P\mathbf{L}\Delta\theta_k$ once per T_{opt}ms;
11: Generate T_{opt}ms carrier signals for correlation and estimate the signal C/N_0;
12: **Update**:
13: ***if*** c/n_0 is not changed ***then***
14: go to line 9;
15: ***else***
16: go to line 6;
17: ***endif***

Chapter 4

State feedback/state estimator design for frequency tracking loop[3]

Frequency tracking is essentially differential carrier phase tracking that neglects absolute phase error and permits relative phase rotation between the received signal and the local carrier replica [8]. Hence, a FLL can be treated as a reduced-order PLL, where a first-order or a second-order FLL achieves the equivalent frequency tracking capability as a second-order or a third-order PLL respectively.

In this Chapter, the general state space design control system process in Chapter 2 is applied in frequency tracking loop design. The detailed frequency tracking loop design and analysis follow the same approach as that of the generalized phase tracking loop design in Chapter 3.

[3]Chapter 4 is the frequency tracking loop part of our papers "R. Yang, KV Ling, EK Poh, and Y.Morton, *Generalized GNSS Signal Carrier Tracking: Part I: Modelling and Analysis*, accepted by IEEE Transactions on Aerospace and Electronic Systems, January 2017. " and "R. Yang, Y.Morton, KV Ling, and EK Poh, *Generalized GNSS Signal Carrier Tracking: Part II: Optimization and Implementation*, accepted by IEEE Transactions on Aerospace and Electronic Systems, January 2017."

4.1 Signal Model

Similar to the system model in phase tracking loop in Chapter 3, we have the following system model for frequency tracking loop:

$$\mathbf{x}_{k+1} = \mathbf{A}_F \mathbf{x}_k + \mathbf{n}_k \tag{4.1}$$

$$\mathbf{z}_k = \mathbf{H}_F \mathbf{x}_k + \mathbf{v}_k \tag{4.2}$$

to incorporate the platform dynamics, oscillator noise, and thermal noise effects into these models. We use these models to design the generalized frequency tracking loop in state space.

4.1.1 State model

In GNSS receivers, PLLs replicate the exact phase and frequency of the incoming signal to enable carrier wipe-off from the incoming signals, while FLLs perform the carrier wipe-off process by replicating the approximate frequency and allowing the replicate phase to rotate with respect to the incoming carrier signal [8]. Thus, only the estimation of the frequency ω_k and frequency rate $\dot{\omega}_k$ are required in frequency tracking loop design. For this reason, we adopt the following state vectors:

$$1 - state : \mathbf{x}_k = \omega_k \tag{4.3}$$

$$2 - state : \mathbf{x}_k = \begin{bmatrix} \omega & \dot{\omega} \end{bmatrix}_k^{\mathrm{T}} \tag{4.4}$$

to represent the input signals associated with typical dynamics of a GNSS receiver.

Similar to the state model of phase tracking loop in Chapter 3, we have the corresponding reduced-order system transition matrix in frequency tracking loop:

$$1 - state : \mathbf{A}_F = 1 \tag{4.5}$$

$$2 - state : \mathbf{A}_F = \begin{bmatrix} 1 & T \\ 0 & 1 \end{bmatrix} \tag{4.6}$$

and the associated noise covariance matrix:

$$1-state:\mathbf{Q}_F=\sigma_\omega^2=(2\pi f_L)^2Tq_\omega \tag{4.7}$$

$$2-state:\mathbf{Q}_F=\begin{bmatrix}\sigma_\omega^2 & \sigma_{\omega\dot{\omega}}^2\\ \sigma_{\omega\dot{\omega}}^2 & \sigma_{\dot{\omega}}^2\end{bmatrix}=(2\pi f_L)^2\begin{bmatrix}Tq_\omega+\frac{T^3}{3}\frac{q_a}{c^2} & \frac{T^2}{2}\frac{q_a}{c^2}\\ \frac{T^2}{2}\frac{q_a}{c^2} & T\frac{q_a}{c^2}\end{bmatrix} \tag{4.8}$$

4.1.2 Measurement model

In frequency tracking loop, the measurement can be obtained through the arctangent frequency discriminator, using dot and cross products [8]:

$$\begin{aligned}\Delta\varpi_{k+1}&=\frac{1}{T}arc\tan\left(cross,\,dot\right)\\&=\frac{1}{T}arc\tan\left(\frac{I_{Pk}Q_{Pk+1}-I_{Pk+1}Q_{Pk}}{I_{Pk}I_{Pk+1}+Q_{Pk}Q_{Pk+1}}\right)\\&=\frac{1}{T}arc\tan\left(\frac{Q_{Pk+1}/I_{Pk+1}-Q_{Pk}/I_{Pk}}{1+\left(Q_{Pk+1}/I_{Pk+1}\right)\left(Q_{Pk}/I_{Pk}\right)}\right)\\&=\frac{1}{T}arc\tan\left(\frac{\tan\left(\Delta\theta_{k+1}\right)-\tan\left(\Delta\theta_k\right)}{1+\tan\left(\Delta\theta_{k+1}\right)\tan\left(\Delta\theta_k\right)}\right)\\&=\frac{1}{T}arc\tan\left(\tan\left(\Delta\theta_{k+1}-\Delta\theta_k\right)\right)\\&=\frac{1}{T}\left(\Delta\theta_{k+1}-\Delta\theta_k\right)\end{aligned} \tag{4.9}$$

Generally, the two-quadrant and four-quadrant arctangent FLL discriminators are adopted in generic receiver design for signals with and without navigation message modulations [3,8]. The frequency trackings of GNSS receivers must be insensitive to 180° reversals in the I_{Pk} and Q_{Pk} signals. Therefore, the sample times of the I_{Pk} and Q_{Pk} signals should not straddle the data bit transitions [17]. The maximum integration time of frequency tracking is 10ms for GPS L1 signal to avoid the data bit transition for channels with data modulation. Substituting equations (3.17) into equation (4.9) (see derivation in Appendix B), we can obtain

$$1-state:\Delta\varpi_k=\Delta\omega_k+\frac{v_k-v_{k-1}}{T} \tag{4.10}$$

$$2-state:\Delta\varpi_k=\Delta\omega_k+\frac{T}{2}\Delta\dot{\omega}_k+\frac{v_k-v_{k-1}}{T}. \tag{4.11}$$

Denote the vector $\hat{\mathbf{x}}_k$ as the local estimation of $\mathbf{x}_k$ and $u_k = (v_k - v_{k-1})/T$, the frequency discriminator output $\Delta\varpi_k$ can be formulated as

$$\Delta\varpi_k = \mathbf{H}_F(\mathbf{x}_k - \hat{\mathbf{x}}_k) + u_k \tag{4.12}$$

where u_k is a non-white frequency measurement noise and $\mathbf{H}_F$ is the frequency tracking loop measurement matrix with the frequency forms:

$$1 - state : \mathbf{H}_F = 1 \tag{4.13}$$

$$2 - state : \mathbf{H}_F = \begin{bmatrix} 1 & \frac{T}{2} \end{bmatrix}. \tag{4.14}$$

4.2 Generalized Frequency Tracking Loop Design

Denote $\varpi_k \triangleq \bar{\varpi} + u_k \triangleq \mathbf{H}_F\mathbf{x}_k + u_k$ as the system input and $\hat{\varpi}_k \triangleq \mathbf{H}_F\hat{\mathbf{x}}_k$ as the system output in frequency tracking loop. The block diagram of the generalized frequency tracking loop is shown as Fig. 4.1.

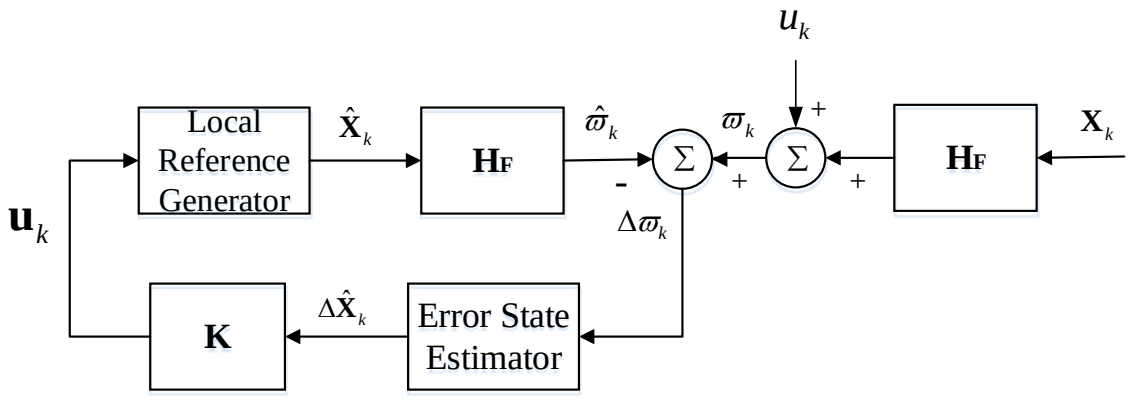

Figure 4.1: Generalized frequency tracking loop architecture

Similar to the state space design for phase tracking loop in Chapter 3, the local reference generator in frequency tracking loop is controlled by the controller $\mathbf{u}_k$:

$$\hat{\mathbf{x}}_{k+1} = \mathbf{A}_F\hat{\mathbf{x}}_k + \mathbf{B}\mathbf{u}_k. \tag{4.15}$$

$\mathbf{u}_k$ is designed by adopting the state feedback strategy as

$$\mathbf{u}_k = \mathbf{K}\Delta\mathbf{x}_k \tag{4.16}$$

And a state estimator need to be constructed based on the measurement $\Delta\varpi_k$ as the true state information is not available:

$$\Delta\hat{\mathbf{x}}_k = \mathbf{A}_F\Delta\hat{\mathbf{x}}_{k-1} - \mathbf{B}\mathbf{u}_{k-1} + \mathbf{L}\left(\Delta\varpi_k - \mathbf{H}_F(\mathbf{A}_F\Delta\hat{\mathbf{x}}_{k-1} - \mathbf{B}\mathbf{u}_{k-1})\right) \tag{4.17}$$

where $\mathbf{L}$ is the estimator gain matrix in frequency tracking loop.

Following the analysis in Chapter 3, we choose $\mathbf{B} = \mathbf{I}$ and $\mathbf{K} = \mathbf{A_F}$ to simplify the error state estimation in equation (4.17) and the corresponding state estimation can be obtained as

$$\hat{\mathbf{x}}_{k+1} = \mathbf{A}_F\hat{\mathbf{x}}_k + \mathbf{A}_F\mathbf{L}\Delta\varpi_k. \tag{4.18}$$

4.3 Estimator Gain Matrix Design

In generalized phase tracking loop design in Chapter 3, the gain matrices for three filter designs, i.e.,PIF, WF, and KF are analyzed. Under the white Gaussian noise assumption, $\mathbf{L}_{WF}$ and $\mathbf{L}_{KF}$ are both the optimal gain matrix that enables MMSE performance in phase tracking loop. However, the frequency measurement noise u_k in frequency tracking loop is not a white noise. KF is not an optimal filter in the sense of MMSE for a FLL, although it has been used in FLL design in [30], and it is also too complicated to obtain the closed-form $\mathbf{L}_{WF}$ for a FLL. Since the PIF is a model-free design approach that is immune to the noise characteristic, we only consider the PIF design in the generalized frequency tracking loop analysis and the gain matrix for a PIF is obtained by mapping the PIF-based frequency tracking loop into the state space architecture through the equivalent closed-loop transfer function discussed in Chapter 2.

The 1- and 2-state forms for $\mathbf{L}$ are:

$$\begin{aligned} &1-state: \mathbf{L} = \alpha \\ &2-state: \mathbf{L} = \begin{bmatrix} \alpha & \beta \end{bmatrix}^{\mathrm{T}}. \end{aligned} \tag{4.19}$$

The corresponding closed-loop transfer function between output $\hat{\varpi}_k$ and input ϖ_k in

the generalized frequency tracking loop is:

$$Y(z) = \frac{\hat{\varpi}_k}{\varpi_k} = \frac{\mathbf{H}_F(z\mathbf{I} - \mathbf{A}_F)^{-1}\mathbf{A}_F\mathbf{L}}{1 + \mathbf{H}_F(z\mathbf{I} - \mathbf{A}_F)^{-1}\mathbf{A}_F\mathbf{L}}. \tag{4.20}$$

with the 1-state and 2-state forms as:

$$1 - state : Y(z) = \frac{\alpha}{z + \alpha - 1} \tag{4.21}$$

$$2 - state : Y(z) = \frac{\left(\alpha + \frac{3T}{2}\beta\right) z - \left(\alpha + \frac{T}{2}\beta\right)}{z^2 + \left(\alpha + \frac{3T}{2}\beta - 2\right) z + \left(-\alpha - \frac{T}{2}\beta + 1\right)} \tag{4.22}$$

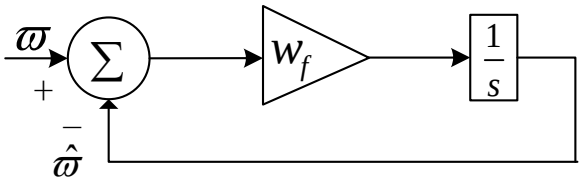

(a)

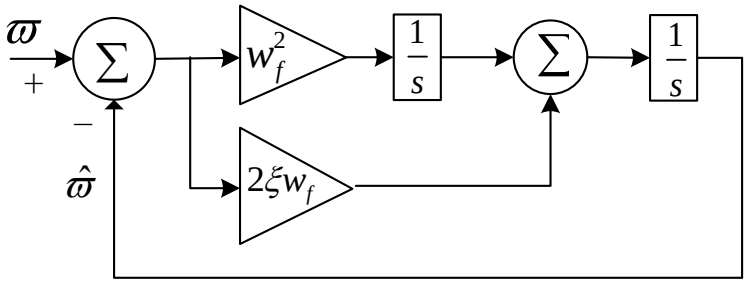

(b)

Figure 4.2: Analog FLL. (a)First-order. (b)Second-order.

The typical methodology to determine the loop gain $\mathbf{L}$ is based on the discretization of an analog FLL with PIF according to the predefined value of noise equivalent bandwidth BW, damping ratio ξ [8]. The structures of first order and second order analog FLL are shown in Fig.4.2. The closed-loop transfer function of the analog FLL in Fig.4.2 can be

obtained as:

$$1-state: H(s) = \frac{\hat{\varpi}}{\varpi} = \frac{w_f}{s + w_f} \tag{4.23}$$

$$2-state: H(s) = \frac{\hat{\varpi}}{\varpi} = \frac{2\xi w_f s + w_f^2}{s^2 + 2\xi w_f s + w_f^2} \tag{4.24}$$

where w_f is the natural frequency in frequency tracking loop and can be calculated with predefined value of BW as shown in Table 2.1.

By using the forward Euler transformation $s = (z-1)/T$, we discretize equations (4.23) and (4.24) from the s-domain to the z-domain and obtain equations (4.25) and (4.26), respectively.

$$1-state: H(z) = \frac{w_f T}{z + w_f T - 1} \tag{4.25}$$

$$2-state: H(z) = \frac{2\xi w_f T z + w_f^2 T^2 - 2\xi w_n T}{z^2 + (2\xi w_f T - 2) z + \left(w_f^2 T^2 - 2\xi w_f T + 1\right)}. \tag{4.26}$$

Comparing the closed loop transfer functions of generalized frequency tracking loop in equations (4.21) and (4.22) with that of the analog FLL in equations (4.25) and (4.26), the gain matrix $\mathbf{L}$ for 1-state and 2-state generalized frequency tracking loops can be obtained as

$$1-state: \mathbf{L} = w_f T \tag{4.27}$$

$$2-state: \mathbf{L} = \begin{bmatrix} 2\xi w_f T - \frac{3}{2} w_f^2 T^2 \\ w_f^2 T \end{bmatrix}. \tag{4.28}$$

Note that the PIF design presented here is based on predefined empirical values of loop parameters. It does not provide the rigorous design process for the loop parameters under different signal conditions, especially in harsh environments where the signal is both weak and on a highly dynamic platform. The performance analysis and optimization for the generalized frequency tracking loop design will be presented next.

4.4 Performance Analysis

In this section, we derive the closed-form expressions of the frequency tracking error covariance matrix and dynamic steady stress error for the generalized frequency tracking loop.

4.4.1 Estimation error variance

Denote $\mathbf{P}_{k+1}$ as the tracking error covariance matrix at $k+1^{th}$ epoch which can be expressed as follows

$$\mathbf{P}_{k+1} = E\left[\left(\mathbf{x}_{k+1} - \hat{\mathbf{x}}_{k+1}\right)\left(\mathbf{x}_{k+1} - \hat{\mathbf{x}}_{k+1}\right)^{\mathrm{T}}\right]. \tag{4.29}$$

Substituting the received and local generated signal in equations (4.1), and (4.18) into (4.29), we have (see derivation in Appendix C)

$$\begin{aligned}\mathbf{P}_{k+1} = \mathbf{A}_F\left(\mathbf{I} - \mathbf{L}\mathbf{H}_F\right)\mathbf{P}_k(\mathbf{I} - \mathbf{L}\mathbf{H}_F)^{\mathrm{T}}\mathbf{A}_F^{\mathrm{T}} + \mathbf{Q}_F + 2\mathbf{A}_F\mathbf{L}\frac{\mathbf{R}}{T^2}(\mathbf{A}_F\mathbf{L})^{\mathrm{T}} \\ -\mathbf{A}_F\left(\mathbf{I} - \mathbf{L}\mathbf{H}_F\right)\mathbf{G}_k(\mathbf{A}_F\mathbf{L})^{\mathrm{T}} - \mathbf{A}_F\mathbf{L}\mathbf{G}_k^{\mathrm{T}}(\mathbf{I} - \mathbf{L}\mathbf{H}_F)^{\mathrm{T}}\mathbf{A}_F^{\mathrm{T}}\end{aligned} \tag{4.30}$$

where $\mathbf{G}_k = E\left[\Delta\mathbf{x}_k {u_k}^T\right]$ and $\mathbf{G}_k^{\mathrm{T}} = E\left[u_k \Delta\mathbf{x}_k{}^T\right]$ represent the correlation between the error state and non-white measurement noise.

At steady state, $\mathbf{P}_{k+1} = \mathbf{P}_k = \mathbf{P}_Y$ and $\mathbf{G}_{k+1} = \mathbf{G}_k = \mathbf{G}_Y$ as (see derivation in Appendix C):

$$\mathbf{G}_Y = \frac{\mathbf{A}_F\mathbf{L}}{T^2}\sigma_v^2 \tag{4.31}$$

and

$$\begin{aligned}\mathbf{P}_Y = \mathbf{A}_F\left(\mathbf{I} - \mathbf{L}\mathbf{H}_F\right)\mathbf{P}_k(\mathbf{I} - \mathbf{L}\mathbf{H}_F)^{\mathrm{T}}\mathbf{A}_F^{\mathrm{T}} + \mathbf{Q}_F + 2\mathbf{A}_F\mathbf{L}(\mathbf{A}_F\mathbf{L})^{\mathrm{T}}\frac{\sigma_v^2}{T^2} \\ -\mathbf{A}_F\left(\mathbf{I} - \mathbf{L}\mathbf{H}_F\right)\mathbf{A}_F\mathbf{L}(\mathbf{A}_F\mathbf{L})^{\mathrm{T}}\frac{\sigma_v^2}{T^2} - \mathbf{A}_F\mathbf{L}(\mathbf{A}_F\mathbf{L})^{\mathrm{T}}(\mathbf{I} - \mathbf{L}\mathbf{H}_F)^{\mathrm{T}}\mathbf{A}_F^{\mathrm{T}}\frac{\sigma_v^2}{T^2}.\end{aligned} \tag{4.32}$$

Denote $\mathbf{p}_{\bar{\omega}}$ as the overall average frequency error variance, we can get:

$$\mathbf{p}_{\bar{\omega}} = \mathbf{H}_F E\left[\left(\mathbf{x}_{k+1} - \hat{\mathbf{x}}_{k+1}\right)\left(\mathbf{x}_{k+1} - \hat{\mathbf{x}}_{k+1}\right)^{\mathrm{T}}\right]\mathbf{H}_F^{\mathrm{T}} = \mathbf{H}_F\mathbf{P}_Y\mathbf{H}_F^{\mathrm{T}}. \tag{4.33}$$

Substituting equation (4.32) into (4.33), it can be seen that $\mathbf{p}_{\bar{\omega}}$ is again related to system characteristics, such as oscillator error, platform dynamics, signal C/N_0, and signal frequency f_L. Like equation (3.64), equation (4.33) also provides a quantitative relationship

between the frequency tracking accuracy and design parameters, such as T or BW.

4.4.2 Dynamic stress steady state error

When the platform velocity or acceleration changes, a steady state error will occur in both the 1-state or 2-state frequency tracking loops. To reflect this change, similar to [72], we add an input dynamic vector to the system model and obtain

$$\mathbf{x}_{k+1} = \mathbf{A}\mathbf{x}_k + \mathbf{n}_k + \mathbf{M}\mathbf{d}_k \tag{4.34}$$

where $\mathbf{d}_k$ represents the user's LOS acceleration a_k in the 1-state frequency tracking loop or LOS jerk j_k in the 2-state frequency tracking loop

$$1 - state : \mathbf{d}_k = a_k(m/s^2) \tag{4.35}$$

$$2 - state : \mathbf{d}_k = j_k(m/s^3). \tag{4.36}$$

$\mathbf{M}$ for frequency tracking has the corresponding forms:

$$\begin{aligned} 1 - state &: \mathbf{M}_F = \frac{2\pi f_L T}{c} \\ 2 - state &: \mathbf{M}_F = \left[\begin{array}{cc} \frac{2\pi f_L}{c}\frac{T^2}{2} & \frac{2\pi f_L T}{c} \end{array} \right]^{\mathrm{T}}. \end{aligned} \tag{4.37}$$

Denote $\mathbf{e}_Y = \lim\limits_{k\to\infty} E\left(\mathbf{x}_{k+1} - \hat{\mathbf{x}}_{k+1}\right)$ as the frequency dynamic stress steady-state error when k approaches to infinity, we have

$$\mathbf{e}_Y = [\mathbf{I} - \mathbf{A_F}\left(\mathbf{I} - \mathbf{L}\mathbf{H_F}\right)]^{-1}\mathbf{M}_F\mathbf{d}_k. \tag{4.38}$$

Hence, the overall dynamic stress frequency error can be expressed as

$$\mathbf{e}_{\bar{\omega}} = \lim_{k\to\infty} E\left(\bar{\varpi}_{k+1} - \hat{\varpi}_{k+1}\right) = \mathbf{H}_F e_Y = \mathbf{H}_F[\mathbf{I} - \mathbf{A}_F\left(\mathbf{I} - \mathbf{L}\mathbf{H}_F\right)]^{-1}\mathbf{M}_F\mathbf{d}_k. \tag{4.39}$$

$\mathbf{e}_{\bar{\omega}}$ also dependent on platform dynamics and signal frequency f_L. Equation (4.39) also provides the quantitative relationship between the dynamic stress error and design parameters, such as T or BW.

4.4.3 The 3-sigma rule

In traditional FLL design, a conservative rule of thumb is usually applied to determine the tracking threshold of FLL, which requires that the 3-sigma frequency jitter must not exceed one-fourth of the frequency pull-in range of the FLL discriminator [8]. Therefore, for the two-quadrant arctangent and four-quadrant frequency discriminators in data and pilot channels, the tracking error should satisfy the following conditions respectively [8]:

$$\sigma_{FLL} = \sqrt{\mathbf{p}_{\bar{\omega}}} + \frac{\mathbf{e}_{\bar{\omega}}}{3} \leq \frac{1}{24T}(Hz) \text{ or } \frac{1}{12T}(Hz) \tag{4.40}$$

Equation (4.40) can be applied to characterize the admissible range of the loop parameters such as T or BW for tracking loop design implementation under various operating situations, with varying signal strength, platform dynamics, and oscillator qualities. The maximum value of T is 10ms in GPS data channel to avoid the data bit transition. Equation (4.40) shows that as the value of T increases from 1ms to 10ms, the threshold for the pilot channel decreases from 83.3Hz to 8.33Hz. A shorter integration time is also preferred because the threshold decreases as the value of T increases. The further improvement of the frequency tracking performance that minimize $\mathbf{p}_{\bar{\omega}}$ will be discussed in the following section.

4.5 Optimization: Minimum Average Frequency Tracking Error Variance Criteria

Similar to the case with phase tracking loop, the minimum frequency tracking error variance for a frequency tracking loop could be achieved if the appropriate value of gain matrix $\mathbf{L}$ is selected for each specified signal strength and receiver platform scenario. The objective of optimization for generalized frequency tracking loop is to determine system parameters that minimize the value of $\mathbf{p}_{\bar{\omega}}$ for the generalized frequency tracking loop design. For a frequency tracking loop operating on a data channel, at least two integrated and dump samples must be taken between data bit transitions, navigation data rate limits the length of the integration time in frequency tracking loop and the maximum value of T for GPS L1 signal frequency tracking is 10ms. Even for pilot channel, a shorter integration time is also preferred in a FLL because the threshold decreases as the value of T increases. Hence, two cases that $T = 1ms$ and $10ms$ are considered for frequency tracking loop optimization and

the corresponding optimal parameter, BW_{opt}, will be analyzed.

4.5.1 1-state frequency tracking loop

Substituting $\mathbf{A}_F$, $\mathbf{H}_F$, $\mathbf{Q}_F$, $\mathbf{R}$ and $\mathbf{L}$ into equation (4.33), we can get:

$$\mathbf{p}_{\bar{\omega}} = \frac{(2\pi f_L)^2 T q_\omega + 2\sigma_v^2/T^2\alpha^3}{2\alpha - \alpha^2}. \tag{4.41}$$

The extreme values of the function are the points where the partial derivatives are zero. We take a derivative with respect to α and obtain:

$$\frac{d\mathbf{p}_{\bar{\omega}}}{d\alpha} = \frac{-2\sigma_v^2/T^2\alpha^4 + 8\sigma_v^2/T^2\alpha^3 + 2(2\pi f_L)^2 T q_\omega(\alpha - 1)}{\alpha^2(\alpha - 2)^2} \tag{4.42}$$

The derivative becomes zero when

$$-2\sigma_v^2/T^2\alpha^4 + 8\sigma_v^2/T^2\alpha^3 + 2(2\pi f_L)^2 T q_\omega(\alpha - 1) = 0. \tag{4.43}$$

Let $b = (2\pi f_L)^2 T^3 q_\omega/\sigma_v^2$, then $\alpha^4 - 4\alpha^3 - b\alpha + b = 0$. The solution that minimizes the value of $\mathbf{p}_{\bar{\omega}}$ is (see derivation in Appendix D)

$$\alpha_{opt} = 1 + \frac{1}{2}\sqrt{4 + \sqrt[3]{b^2 + 16b}} - \frac{1}{2}\sqrt{8 - \sqrt[3]{b^2 + 16b} + \frac{2b + 16}{\sqrt{4 + \sqrt[3]{b^2 + 16b}}}}. \tag{4.44}$$

According to the relationship between α and BW in equation (4.27) and Table 2.1, we can obtain the optimal value of BW_{opt} as:

$$1 - state : BW_{opt} = \frac{\alpha_{opt}}{4T}. \tag{4.45}$$

4.5.2 2-state frequency tracking loop

Due to the complexity involved in obtaining the analytical solutions of BW_{opt} for the 2-state case, the numerical solutions are provided here instead. The following scenarios are considered: $C/N_0 = 10 \sim 44$dB-Hz and $q_a = 0.1, 1, 10, 100, 1000 m^2/s^5$ in the receiver with LQO and HQO. T is set at 1ms and 10ms, and the maximum value of $BW \cdot T$ is 0.5. To calculate the optimal values of BW_{opt} for various signal scenarios, we obtain the minimum

value of $\mathbf{p}_{\bar{\omega}min}$ over the search space of $BW \cdot T$ from 0.0001 to 0.5, and C/N_0 from 10dB-Hz to 44dB-Hz for each specified dynamics. Then, the corresponding values of BW_{opt} can be obtained by dividing the optimal product $BW \cdot T$ that minimizing $\mathbf{p}_{\bar{\omega}}$ by $T = 1ms$ or $T = 10ms$ accordingly. As an example, the values of BW_{opt} and $\sqrt{\mathbf{p}_{\bar{\omega}min}}$ for the 2-state frequency tracking loops with $T = 1ms$ and $10ms$ under different dynamics are plotted in Fig. 4.3 and 4.4, respectively. Besides, the solutions in 1-state frequency tracking loops with $T = 1ms$ and $10ms$ under static ($q_a = 0m^2/s^5$) are also plotted in Fig. 4.3 and 4.4 for comparison purpose.

For $T = 1ms$, Fig. 4.3(a) shows the following:

i). BW_{opt} increases as C/N_0 decreases.

ii). For a static receiver, BW_{opt} for the receiver with a LQO is larger than that of the receiver with a HQO. This is because the system modelling error, and therefore, the frequency tracking error due to the noise is larger for the LQO than for HQO. A larger bandwidth is therefore needed for the receiver with LQO. However, for a receiver on a higher dynamic platform, the oscillator noise effect is less important and can even be neglected. Thus BW_{opt} overlaps for the LQO and HQO for highly dynamic case.

iii). As the platform dynamics increase, BW_{opt} also increases, indicating that the FLL needs a wider bandwidth to handle the higher dynamics.

Fig. 4.3(b) shows that:

i). $\sqrt{\mathbf{p}_{\bar{\omega}min}}$ decreases as C/N_0 increases.

ii). $\sqrt{\mathbf{p}_{\bar{\omega}min}}$ is slightly larger for LQO than for HQO for the static scenario. The oscillator noise effect in FLL becomes less important when the dynamic is increased. The frequency tracking error differences between the receivers with LQO and HQO are smaller than 2Hz when $C/N_0 = 10$dB-Hz and under a static condition for both $T = 1$ms and 10ms in Fig. 4.3(b) and Fig. 4.4(b). While under the same signal strength and static condition, the phase tracking error difference between the receivers with LQO and HQO is $\sim 30°$, as shown in Fig.3.10. Hence, the difference between LQO and HQO is negligible for all scenarios in a frequency tracking loop, while for a phase frequency tracking is less affected by the oscillator noise and more robust than carrier phase tracking.

iii). $\sqrt{\mathbf{p}_{\bar{\omega}min}}$ increases as receiver dynamic increases. This is because for a more dynamic signal, a larger loop bandwidth is used to handle the higher dynamics, which results in a reduced tracking accuracy.

A similar trend is presented in Fig. 4.4 for $T = 10ms$. Comparing Fig. 4.3 and Fig. 4.4,

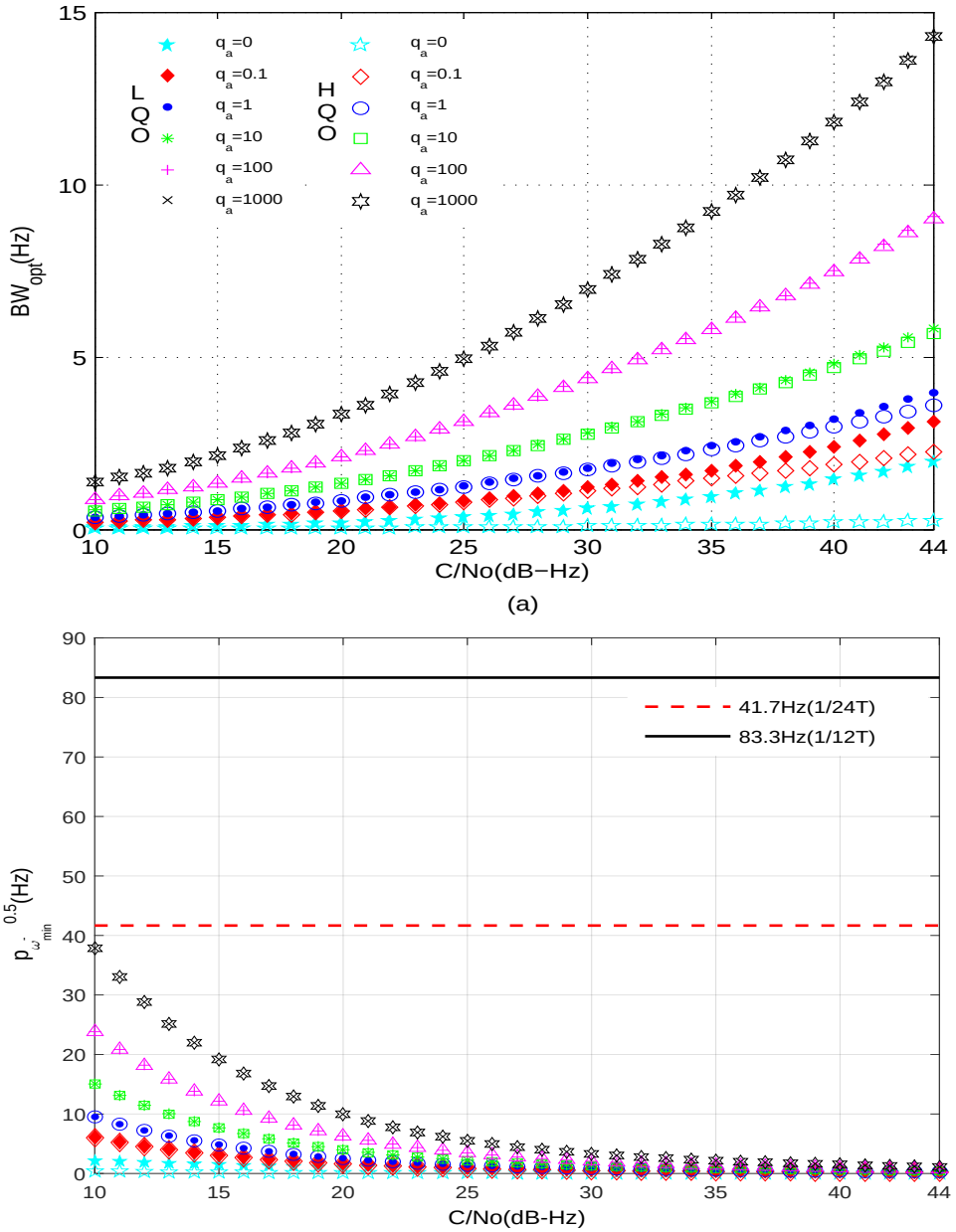

Figure 4.3: BW_{opt} and $\sqrt{\mathbf{p}_{\bar{\omega}min}}$ versus C/N_0 for static, low, and high signal dynamics, and both high and low receiver oscillator qualities in the PIF-based frequency tracking loop with $T = 1ms$

the frequency tracking errors for $T = 1ms$ and 10ms are ∼38Hz and ∼10Hz, respectively when $C/N_0 = 10$dB-Hz and $q_a = 1000m^2/s^5$, indicating that with a longer integration time,

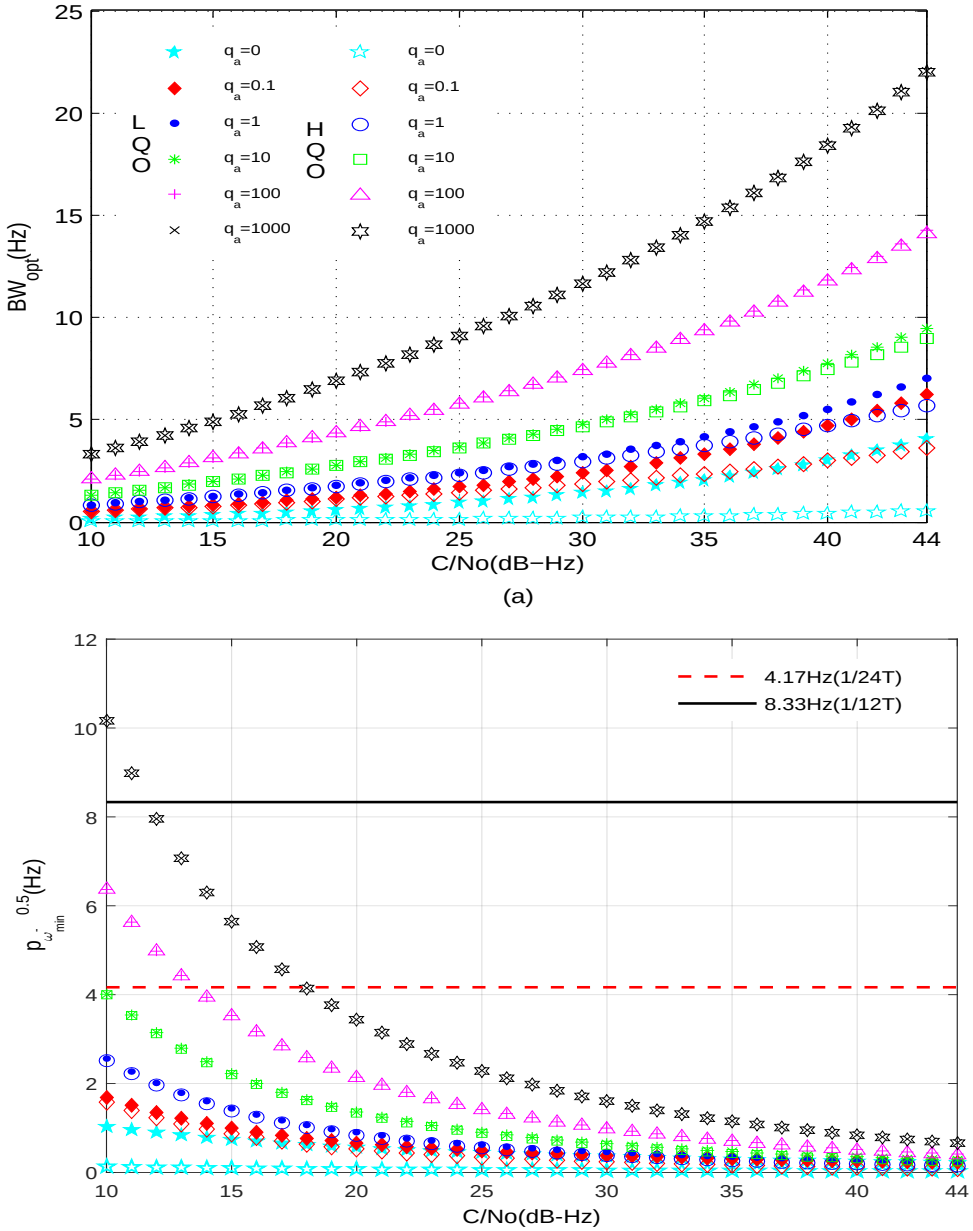

Figure 4.4: BW_{opt} and $\sqrt{\mathbf{p}_{\bar{\omega}min}}$ versus C/N_0 for static, low, and high signal dynamics, and both high and low receiver oscillator qualities in the PIF-based frequency tracking loop with $T = 10ms$

a frequency tracking loop achieves better tracking accuracy. This observation is consistent with that for a phase tracking loop in Chapter 3. However, a frequency tracking loop

takes more risk in increasing T than a phase tracking loop, because the frequency tracking threshold decreases when T increases, as shown by the dash red lines in Fig. 4.3 and Fig. 4.4. Even for a pilot channel without data modulation, T should be relative small to ensure the frequency tracking ability.

Table 4.1: Theoretical frequency tracking loop tracking sensitivities with thresholds of $\frac{1}{24T}$ (data channel) and $\frac{1}{12T}$ (pilot channel) for static, low, and high signal dynamics, both high and low receiver oscillator qualities, and optimal frequency tracking loop designs (unit: dB-Hz)

$q_a(m^2/s^5)$	LQO		HQO	
	$T = 1ms$	$T = 10ms$	$T = 1ms$	$T = 10ms$
0	$< 0/< 0$	$< 0/< 0$	$< 0/< 0$	$< 0/< 0$
0.1	$< 0/< 0$	$3/< 0$	$< 0/< 0$	$3/< 0$
1	$< 0/< 0$	$7/1$	$< 0/< 0$	$7/2$
10	$3/< 0$	$10/5$	$3/< 0$	$10/5$
100	$6/1$	$14/8$	$7/1$	$14/9$
1000	$10/5$	$18/12$	$10/5$	$18/12$

Note: < 0 represents the theoretical sensitivity is at least 0dB-Hz;
**/* represent the corresponding frequency tracking loop sensitivity with respect to $\frac{1}{24T}(Hz)/\frac{1}{12T}(Hz)$ threshold.*

The theoretical tracking sensitivities of the generalized frequency tracking loops with $T = 1ms$ and $10ms$ and their corresponding BW_{opt} are summarized in Table 4.1. It shows that:

i). As dynamic increases, the tracking sensitivity decreases.

ii). The tracking sensitivity in frequency tracking loop with $T = 10ms$ is worse than that with $T = 1ms$ due to the frequency tracking loop threshold being inversely proportional to the integration time, although the tracking accuracy is better with the greater integration time.

iii). The frequency tracking loop tracking sensitivity difference between receivers with LQO and HQO is negligible.

iv). There is a 5dB to 6dB improvement in pilot channels over data channels, which is consistent with the conclusions in phase tracking loop, as well as reference [8].

v). Comparing Table 4.1 and Table 3.1, it can be noted that tracking sensitivity in frequency tracking loops is much better than in phase tracking loops. The tracking sensitivity limit in a frequency tracking loop is at least 0dB-Hz, which is 6dB better than that

of a phase tracking loop, indicating that the frequency tracking is more robust than carrier phase tracking under weak signal conditions.

vi). Table 4.1 shows the theoretical sensitivity in the frequency tracking loop. It is based on the assumptions of perfect frequency synchronization. However, in practice, large frequency error probably occurred in frequency tracking loop which may degrades the frequency tracking performance and results in worse tracking sensitivity.

Similar to phase tracking loop, the relationships between BW_{opt} and C/N_0 in 2-state frequency tracking loops with $T = 1ms$ and $10ms$ are formulated as:

$$BW_{opt} = b_3(C/N_0)^{\mu_3}(Hz) \tag{4.46}$$

by using the curve fitting for practical implementations. The parameters b_3 and μ_3 that listed in Table 4.2 for various signal dynamics and receiver oscillator qualities are computed through simulations. Table 4.2 shows that there is only a slight difference between LQO and HQO in low dynamic scenario, while in highly dynamic scenario this difference between LQO and HQO is negligible. Equations (4.45) and (4.46) together with b_3 and μ_3 provide the optimal designs in the generalized frequency tracking loop under diverse dynamic and weak signal scenarios.

Table 4.2: BW_{opt} parameter values for low and high signal dynamics, and both high and low receiver oscillator qualities in 2-state PIF-based frequency tracking loop design

$q_a(m^2/s^5)$	Oscillator quality	$T = 1ms$		$T = 10ms$	
		b_3	μ_3	b_3	μ_3
0.1	LQO	0.133	0.314	0.298	0.30
	HQO	0.167	0.264	0.397	0.22
1	LQO	0.246	0.279	0.556	0.25
	HQO	0.263	0.264	0.628	0.22
10	LQO	0.420	0.264	1.023	0.22
	HQO				
100	LQO	0.659	0.265	1.57	0.22
	HQO				
1000	LQO	1.049	0.264	2.46	0.22
	HQO				

4.6 Adaptive Frequency Tracking Process

Similar to phase tracking loop, based on the estimations of C/N_0 and q_a, the adaptive tuning scheme for a frequency tracking loop can be operated by the following steps, as shown in algorithm 2:

1) Initialization. The tracking loop is initialized with Doppler frequency, carrier phase, and C/N_0 estimations from the acquisition process. In this initial stage, the frequency tracking loop is operating with a 1ms integration time and large loop bandwidth values (for example $BW \geq 50$Hz) are adopted to ensure fast convergence to the steady state.

2) Optimal tracking. Setting the integration time T as 1ms or 10ms, we also assume that the data is wiped off when $T > 1ms$ on the data channel. BW_{opt} is obtained according to knowledge of C/N_0 and q_a estimations through equations (4.45) or (4.46). The corresponding loop gain $\mathbf{L}$ is calculated and used to update the frequency state estimation in the frequency tracking loop. The results will be used to generate T ms carrier signals for correlation with incoming signals, calculate the frequency discriminator, and estimate the signal C/N_0 for preparation of the next tracking iteration.

3) Update. The loop parameters computed from 2) are updated when a new C/N_0 estimation is obtained in the new epoch. Otherwise, keep the value of BW unchanged until C/N_0 is updated.

The adaptive frequency tracking loop adjusts the value $\mathbf{L}$ in each iteration to achieve the theoretical MMSE frequency tracking performance. Similar to the adaptive phase tracking algorithm, in a fading environment, this algorithm may not work if the fading is faster than the C/N_0 estimation time interval. Although the tracking sensitivity for frequency tracking loop is close to 0dB-Hz in previous analysis, the adaptive tracking algorithm tracking performance is actually restricted by the C/N_0 estimation accuracy for real implementation. Hence, without a better C/N_0 estimator that can estimate the signal C/N_0 below 17dB-Hz level, this algorithm may not work as well.

Algorithm 2 Adaptive frequency tracking algorithm

1: **Initialization**:
2: Set $T = 1$ms and calculate the frequency error $\Delta\varpi_k$ from the frequency discriminator once per 1ms;
3: Set $BW = 50Hz$ to make the tracking loop fast convergent to steady-state;
4: Obtain the value of C/N_0 estimation, c/n_0, through the SNR estimator;
5: **Optimal tracking**:
6: Set $T = 1ms$ or $T = 10ms$;
7: Set $BW = BW_{opt}$, where $BW_{opt} = b_3(c/n_0)^{\mu_3}$ if $q_a \neq 0m^2/s^5$, or $BW_{opt} = \alpha_{opt}/T$ if $q_a = 0m^2/s^5$;
8: Calculate the loop gain matrix $\mathbf{L}$;
9: Calculate the frequency error $\Delta\varpi_k$ from the frequency discriminator once per Tms;
10: Estimate the state $\hat{\mathbf{x}}_{k+1} = \mathbf{A}_F\hat{\mathbf{x}}_k + \mathbf{A}_F\mathbf{L}\Delta\varpi_k$ once per Tms;
11: Generate Tms carrier signals for correlation and estimate the signal C/N_0;
12: **Update**:
13: ***if*** c/n_0 is not changed ***then***
14: go to line 9;
15: ***else***
16: go to line 7;
17: ***endif***

Chapter 5

Simulation Results[4]

Simulations are presented in this chapter to verify our theoretical derivations and to evaluate the performance of adaptive tracking schemes with optimal design in both the phase and frequency tracking loops.

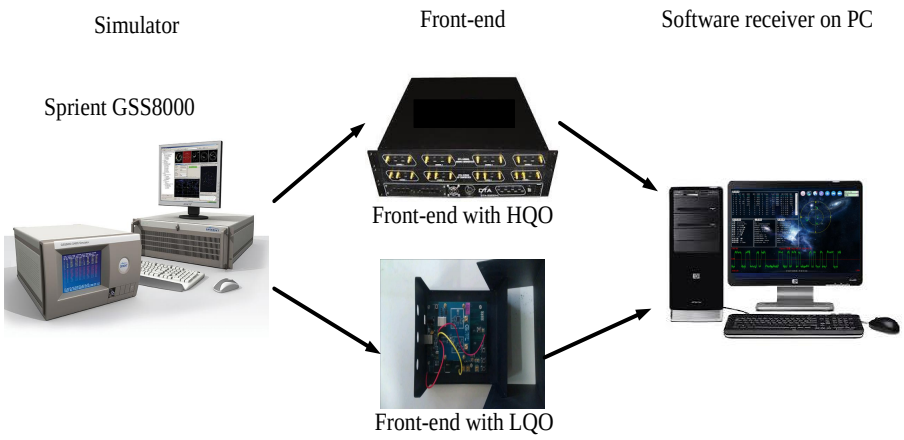

Figure 5.1: Simulation data collection and algorithm performance set-up

The simulation set-up is shown as Fig.5.1, we use spirent GSS8000 simulator to generate the GPS L1 signals. Since the oscillator quality impacts the tracking performance, we use two RF front-ends: one is a low cost front-end with LQO, while the other is a high cost front-end with a HQO, to sample the data. Then we test the tracking algorithms on the software

[4]Chapter 5 is simulation part of our paper "R. Yang, Y.Morton, KV Ling, and EK Poh, *Generalized GNSS Signal Carrier Tracking: Part II: Optimization and Implementation*, accepted by IEEE Transactions on Aerospace and Electronic Systems, January 2017"

receiver platform in a computer. The h-parameters are set as $h_0 = 1 \times 10^{-21}(s^2/\text{Hz})$, $h_{-2} = 2 \times 10^{-20}(1/\text{Hz})$ for the receiver front-end with LQO, and $h_0 = 6.4 \times 10^{-26}(s^2/\text{Hz})$, $h_{-2} = 4.3 \times 10^{-23}(1/\text{Hz})$ for the receiver front-end with HQO, respectively. These values are similar to typical values that can be found in [4, 18].

5.1 Verification of Theoretical Derivations

Dynamic signals with nominal strength are conducted to validate the theoretical prediction of dynamic stress error (Eq (3.72),(4.39)) and tracking accuracy (Eq (3.64),(4.33)) for the phase and frequency tracking loops. In this scenario, the receiver is assumed to move with a certain acceleration, as shown in Fig.5.2. In the first 38 seconds, the receiver is static, then it starts moving to the east with an acceleration of $50m/s^2$ for 10 seconds. After this, it slows down with an acceleration of -50 m/s^2 for 10 seconds and remains stationary from 58 seconds until 100 seconds. 5 satellites are visible during the time period and C/N_0 of all the satellites are set at 46dB-Hz. The RF front-end with LQO collects the data with an IF at 4.309MHz, sampling frequency at 12MHz, and stored with 1-bit resolution for post-processing.

5.1.1 Discriminator output

In phase tracking loop, the variance and mean of the phase discriminator output $\Delta\theta_k$ (see equation (3.17)) can be written as

$$\mathbf{p}_\theta = E\left[\left(\theta_{k+1} - \hat{\theta}_{k+1}\right)^2\right] = E\left[\left(\bar{\theta}_{k+1} - \hat{\theta}_{k+1}\right)^2\right] + \sigma_v^2 = \mathbf{p}_{\bar{\theta}} + \mathbf{R} \tag{5.1}$$

$$\mathbf{e}_\theta = E\left(\theta_{k+1} - \hat{\theta}_{k+1}\right) = E\left(\bar{\theta}_{k+1} + v_{k+1} - \hat{\theta}_{k+1}\right) = \mathbf{e}_{\bar{\theta}}. \tag{5.2}$$

If an accurate estimation of the received signal C/N_0 can be obtained, the variance of the measurement noise term $\mathbf{R}$ can be accurately estimated and removed. The average phase error covariance $\mathbf{p}_{\bar{\theta}}$ can then be computed from equation (5.1). This can be used to verify the theoretical average phase error variance in equation (3.64). According to equation (5.2), the measured mean value of phase discriminator output can be directly used to verify the theoretical mean estimation in equation (3.72) since they are mathematically equivalent. In the following subsections, we denote $\tilde{\mathbf{p}}_{\bar{\theta}}$ and $\tilde{\mathbf{e}}_{\bar{\theta}}$ as the measured values of $\mathbf{p}_{\bar{\theta}}$ and $\mathbf{e}_{\bar{\theta}}$ from

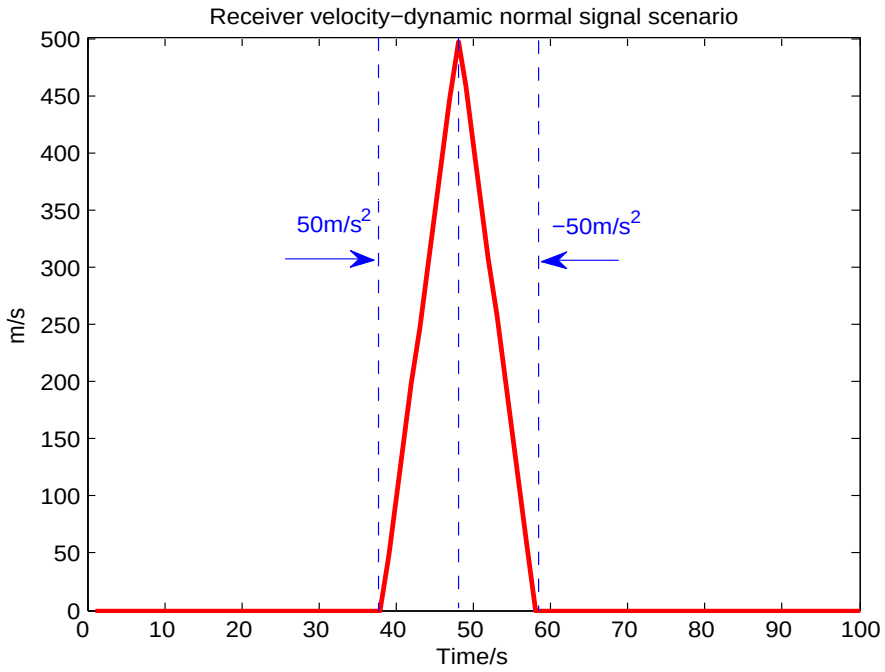

Figure 5.2: Simulated generated receiver platform velocity under normal signal strength condition.

the discriminator output through equations (5.1) and (5.2) and $\hat{\mathbf{p}}_{\bar{\theta}}$ and $\hat{\mathbf{e}}_{\bar{\theta}}$ as the estimated values of $\mathbf{p}_{\bar{\theta}}$ and $\mathbf{e}_{\bar{\theta}}$ from equations (3.64) and (3.72).

Similarly, the variance and mean of the frequency discriminator output $\Delta\varpi_k$ (see equation (4.9)) can be written as

$$\begin{aligned}\mathbf{p}_{\omega} &= E\left[(\varpi_{k+1}-\hat{\varpi}_{k+1})^2\right] = E\left[(\mathbf{H}_F\Delta\mathbf{x}_k+u_k)^2\right]\\ &= \mathbf{H}_F\mathbf{P}_Y\mathbf{H}_F^{\mathrm{T}} + 2\frac{\mathbf{R}}{T^2} + \mathbf{H}_F\mathbf{G}_Y + \mathbf{G}_Y^{\mathrm{T}}\mathbf{H}_F^{\mathrm{T}}\\ &= \mathbf{p}_{\bar{\omega}} + 2\frac{\sigma_v^2}{T^2} + \mathbf{H}_F\mathbf{A}_F\mathbf{L}\frac{\sigma_v^2}{T^2} + (\mathbf{A}_F\mathbf{L})^{\mathrm{T}}\mathbf{H}_F^{\mathrm{T}}\frac{\sigma_v^2}{T^2}\end{aligned} \tag{5.3}$$

$$\mathbf{e}_{\omega} = E\left(\varpi_{k+1}-\hat{\varpi}_{k+1}\right) = E\left(\bar{\varpi}_{k+1}+u_{k+1}-\hat{\varpi}_{k+1}\right) = \mathbf{e}_{\bar{\omega}}. \tag{5.4}$$

Based on the accurate signal C/N_0 estimation, the average frequency error covariance $\mathbf{p}_{\bar{\omega}}$ can then be computed from equation (5.3). Equation (5.4) shows that the measured mean value of frequency discriminator output can be directly used to verify the theoretical mean estimation in equation (4.39) since they are mathematically equivalent. In the following

subsections, we denote $\tilde{\mathbf{p}}_{\bar{\omega}}$ and $\tilde{\mathbf{e}}_{\bar{\omega}}$ as the measured values of $\mathbf{p}_{\bar{\omega}}$ and $\mathbf{e}_{\bar{\omega}}$ from the frequency discriminator output through equations (5.3) and (5.4) and $\hat{\mathbf{p}}_{\bar{\omega}}$ and $\hat{\mathbf{e}}_{\bar{\omega}}$ as the estimated values of $\mathbf{p}_{\bar{\omega}}$ and $\mathbf{e}_{\bar{\omega}}$ from equations (4.33) and (4.39).

5.1.2 Simulation verification

1). Phase tracking loop: The 2-state and 3-state phase tracking loops with $\mathbf{L}_{PIF}$, $\mathbf{L}_{WF}$ and $\mathbf{L}_{KF}$ are tested. The integration time is $1ms$, the value of BN for $\mathbf{L}_{PIF}$ is set at 50Hz and the value of q_a in 3-state tracking loop is set as $50m^2/s^5$. To validate our theoretical analysis in a dynamic situation, the measured and theoretical estimated values of $\mathbf{e}_{\bar{\theta}}$ and $\mathbf{p}_{\bar{\theta}}$ for these 5 satellites signals are listed in Table 5.1 and Table 5.2.

Table 5.1: Validation of analytic equations (3.64) and (3.72) in 2-state phase tracking loop for various LOS accelerations when $C/N_0 = 46$dB-Hz

PRN/$a(m/s^2)$	$\mathbf{L}_{PIF}(BN = 50Hz, T = 1ms)$		$\mathbf{L}_{WF}/\mathbf{L}_{KF}(T = 1ms)$	
	Measured/Theoretical $\tilde{\mathbf{e}}_{\bar{\theta}}/\hat{\mathbf{e}}_{\bar{\theta}}(^\circ)$	Measured/Theoretical $\sqrt{\tilde{\mathbf{p}}_{\bar{\theta}}}/\sqrt{\hat{\mathbf{p}}_{\bar{\theta}}}(^\circ)$	Measured/Theoretical $\tilde{\mathbf{e}}_{\bar{\theta}}/\hat{\mathbf{e}}_{\bar{\theta}}(^\circ)$	Measured/Theoretical $\sqrt{\tilde{\mathbf{p}}_{\bar{\theta}}}/\sqrt{\hat{\mathbf{p}}_{\bar{\theta}}}(^\circ)$
6/ -37.3	-7.9/-7.9	2.6/2.2	–/-59.5	–/1.9
10/ -48.2	-10.2/-10.2	2.4/2.2	–/-76.9	–/1.9
12/ -20.9	-4.4/ -4.4	2.6/2.2	-32.9/ -33.5	2.3/1.9
13/ -4.9	-1.0/ -1.0	2.5/2.2	-7.7/ -7.8	2.1/1.9
23/ 8.2	1.7/1.7	2.7/2.2	12.8/13.1	2.6/1.9

Note: –represents unavailable measurements due to the loss of lock;

Table 5.2: Validation of analytic equations (3.64) and (3.72) in 3-state phase tracking loop for various LOS accelerations when $C/N_0 = 46$dB-Hz

PRN/$a(m/s^2)$	$\mathbf{L}_{PIF}(BN = 50Hz, T = 1ms)$		$\mathbf{L}_{WF}/\mathbf{L}_{KF}(q_a = 50m^2/s^5, T = 1ms)$	
	Measured/Theoretical $\tilde{\mathbf{e}}_{\bar{\theta}}/\hat{\mathbf{e}}_{\bar{\theta}}(^\circ)$	Measured/Theoretical $\sqrt{\tilde{\mathbf{p}}_{\bar{\theta}}}/\sqrt{\hat{\mathbf{p}}_{\bar{\theta}}}(^\circ)$	Measured/Theoretical $\tilde{\mathbf{e}}_{\bar{\theta}}/\hat{\mathbf{e}}_{\bar{\theta}}(^\circ)$	Measured/Theoretical $\sqrt{\tilde{\mathbf{p}}_{\bar{\theta}}}/\sqrt{\hat{\mathbf{p}}_{\bar{\theta}}}(^\circ)$
6/ -37.3	-1.4e-5/0	2.6/2.4	-5.0e-4/0	2.5/2.2
10/ -48.2	-3.0e-5/0	2.4/2.4	-6.0e-4/0	2.4/2.2
12/ -20.9	1.9e-5/0	2.6/2.4	-2.3e-3/0	2.5/2.2
13/ -4.9	1.2e-5/0	2.5/2.4	-1.7e-3/0	2.4/2.2
23/ 8.2	2.3e-5/0	2.8/2.4	-2.9e-3/0	2.6/2.2

As can be observed in Table 5.1, the LOS accelerations of PRN 12 and PRN 23 are

about $-20.9m/s^2$ and $8.2m/s^2$, and the values of $\tilde{\mathbf{e}}_{\bar{\theta}}$ in the 2-state phase tracking loop with $\mathbf{L}_{PIF}$ are -4.4° and 1.7°, respectively. This indicates that a larger magnitude of LOS acceleration is associated with a larger steady state phase error. It can also be observed that the values of $\tilde{\mathbf{e}}_{\bar{\theta}}$ of PRN 12 and PRN 23 in the tracking loop with $\mathbf{L}_{WF}/\mathbf{L}_{KF}$ are about -32.9° and 12.8°, respectively, much larger than that of the PIF-based tracking loop. In some cases such as PRN 6 and PRN 10, the 2-state phase tracking loop with $\mathbf{L}_{WF}$ and $\mathbf{L}_{KF}$ even lost lock due to the large dynamics. That's because $\mathbf{L}_{WF}$ and $\mathbf{L}_{KF}$ are designed with MMSE criterion; the equivalent bandwidth is too narrow to be effective in tracking the high dynamic signals. Since $\mathbf{L}_{PIF}$ is designed with predefined value of BN; thus, the loop can handle the dynamic error if BN is sufficiently large (50Hz in this case). However, the dynamic stress error $\tilde{\mathbf{e}}_{\bar{\theta}}$ can be effectively eliminated by the 3-state tracking loop, as can be seen in Table 5.2. Furthermore, the values of $\sqrt{\tilde{\mathbf{p}}_{\bar{\theta}}}$ are similar for the 3-state and the 2-state cases. As a result, excluding the cases with loss of lock, the measured values, i.e., $\tilde{\mathbf{e}}_{\bar{\theta}}$ and $\tilde{\mathbf{p}}_{\bar{\theta}}$ agree with the estimated values, i.e., $\hat{\mathbf{e}}_{\bar{\theta}}$ and $\hat{\mathbf{p}}_{\bar{\theta}}$ which validates our theoretical derivations of analytic equations (3.64) and (3.72) in phase tracking loop.

2). Frequency tracking loop: The 1-state and 2-state PIF-based frequency tracking loops with $T = 1ms$ and $BW = 50$Hz are tested. To validate our theoretical analysis in a dynamic situation, the measured and theoretical estimated values of $\mathbf{e}_{\bar{\omega}}$ and $\mathbf{p}_{\bar{\omega}}$ for these 5 satellites signals are listed in Table 5.3.

Table 5.3: Validation of analytic equations (4.33) and (4.39) in 1-state and 2-state frequency tracking loops for various LOS accelerations when $C/N_0 = 46$dB-Hz

PRN/$a(m/s^2)$	1-state($BW = 50Hz, T = 1ms$)		2-state($BW = 50Hz, T = 1ms$)	
	Measured/Theoretical $\tilde{\mathbf{e}}_{\bar{\omega}}/\hat{\mathbf{e}}_{\bar{\omega}}$(Hz)	Measured/Theoretical $\sqrt{\tilde{\mathbf{p}}_{\bar{\omega}}}/\sqrt{\hat{\mathbf{p}}_{\bar{\omega}}}$(Hz)	Measured/Theoretical $\tilde{\mathbf{e}}_{\bar{\omega}}/\hat{\mathbf{e}}_{\bar{\omega}}$(Hz)	Measured/Theoretical $\sqrt{\tilde{\mathbf{p}}_{\bar{\omega}}}/\sqrt{\hat{\mathbf{p}}_{\bar{\omega}}}$(Hz)
6/ -37.3	-20.7/-20.5	5.0/3.8	6.4e-4/0	4.7/2.5
10/ -48.2	-27.1/-26.5	4.7/3.8	1.6e-3/0	3.8/2.5
12/ -20.9	-11.7/-11.5	4.8/3.8	-2.7e-5/0	3.7/2.5
13/ -4.9	-2.7/-2.7	4.2/3.8	-3.8e-4/0	4.6/2.5
23/ 8.2	4.6/4.5	5.1/3.8	-5.6e-4/0	4.8/2.5

As can be observed in Table 5.3, the values of $\tilde{\mathbf{e}}_{\bar{\omega}}$ in the 1-state frequency tracking loop for PRN 12 and PRN 23 satellite signals are $-11.7m/s^2$ and $4.6m/s^2$, respectively. This indicates that a larger magnitude of LOS acceleration is associated with a larger steady state

frequency error in frequency tracking loop which is similar to phase tracking loop. While, this dynamic stress error can be effectively eliminated in higher order frequency tracking loop, such as 2-state frequency tracking loop, where the bias due to receiver dynamics are estimated. Besides, the values of $\tilde{\mathbf{e}}_{\bar{\omega}}$ and $\tilde{\mathbf{p}}_{\bar{\omega}}$ agree with the estimated values, i.e., $\hat{\mathbf{e}}_{\bar{\omega}}$ and $\hat{\mathbf{p}}_{\bar{\omega}}$ which validates our theoretical derivations of analytic equations (4.33) and (4.39) in frequency tracking loop.

5.2 Simulation Results of adaptive phase/frequency tracking scheme

Two scenarios, the static weak signals and dynamic weak signals, are conducted to verify our theoretical optimization analysis and to evaluate the performance of the proposed adaptive phase and frequency tracking loops in the presence of thermal noise, oscillator noise, and receiver platform dynamics.

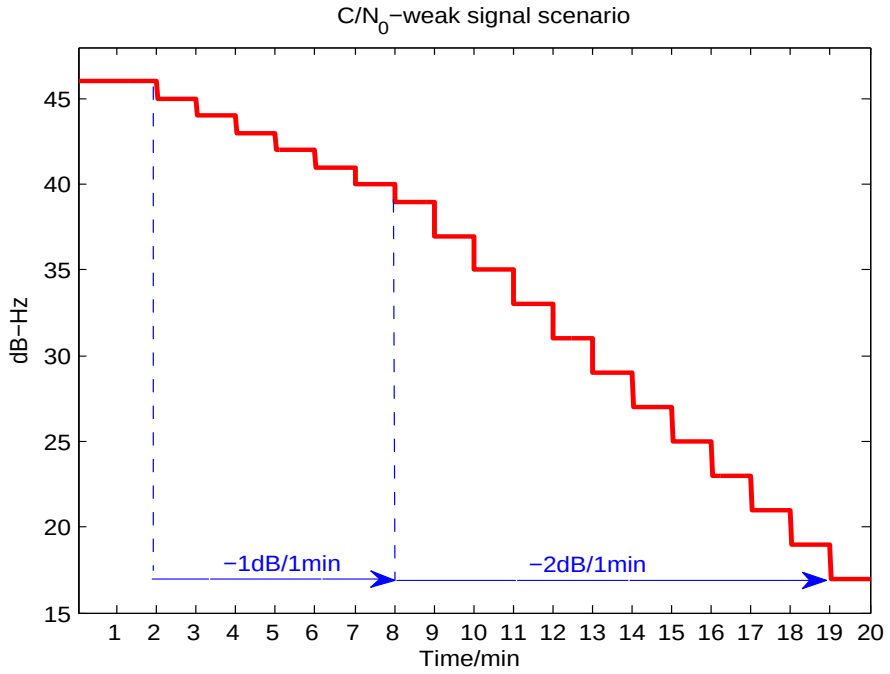

Figure 5.3: Simulated generated signal C/N_0 under static condition.

5.2.1 Static weak signal scenario

In this scenario, the receiver is assumed to be statically located at (N39°, W82°). 8 channels are simulated and the signal C/N_0 for these 8 channels are set as 46dB-Hz for two minutes, then the signal power is decreased 1dB per minute for 6 minutes, then at 2dB per minute rate until the maximum attenuation of 29dB is reached as shown in Fig.5.3. The RF front-end with HQO down-converts the input signal to baseband with IF of 0MHz, sampled at 100MHz, and stored with 16-bit resolution for post-processing. Additionally, a NovAtel receiver was also connected to the simulator to record data simultaneously with the RF front-end for the purpose of comparison.

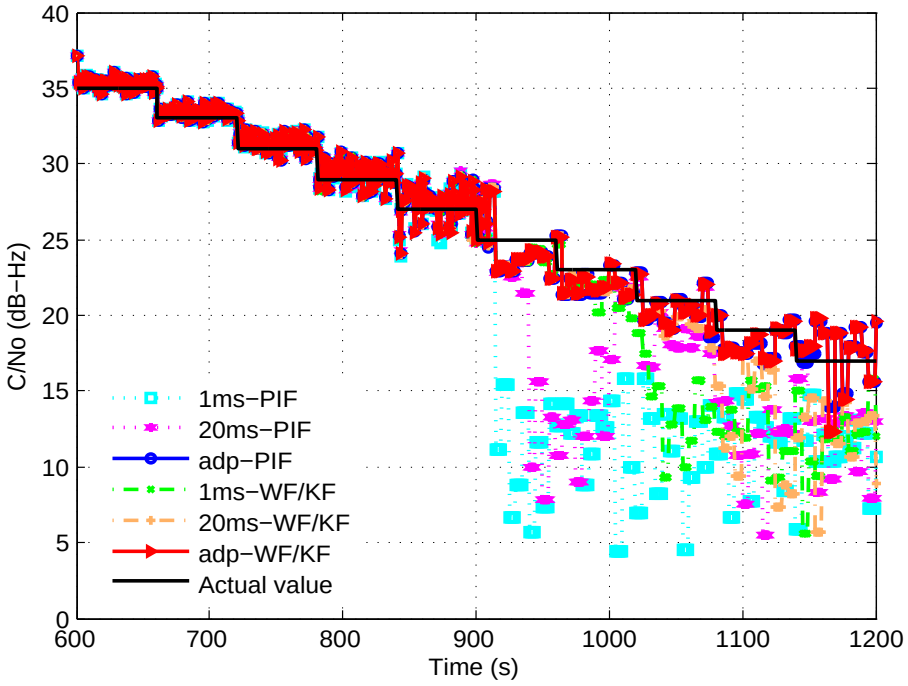

Figure 5.4: C/N_0 estimations variation in 2-state phase tracking loops for PRN 19 satellite signal after 600s ($C/N_0 < 35$dB-Hz). The estimated C/N_0 is used to tune T_{opt} and BN_{opt} in adaptive phase tracking loops as well as measurement noise covariance matrix $\mathbf{R}$ in WF/KF-based phase tracking loops.

1). Adaptive phase tracking loop scheme: Three different types of 2-states phase tracking loops are evaluated for static weak signals. They are:

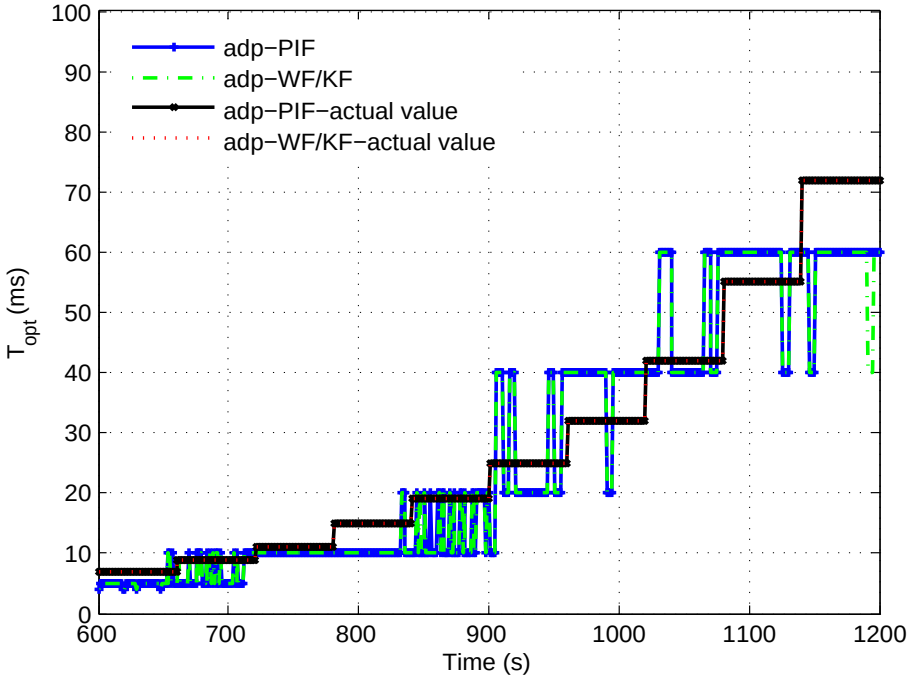

Figure 5.5: The variation of T_{opt} with C/N_0 in 2-state adaptive PIF- and WF/KF-based phase tracking loops.

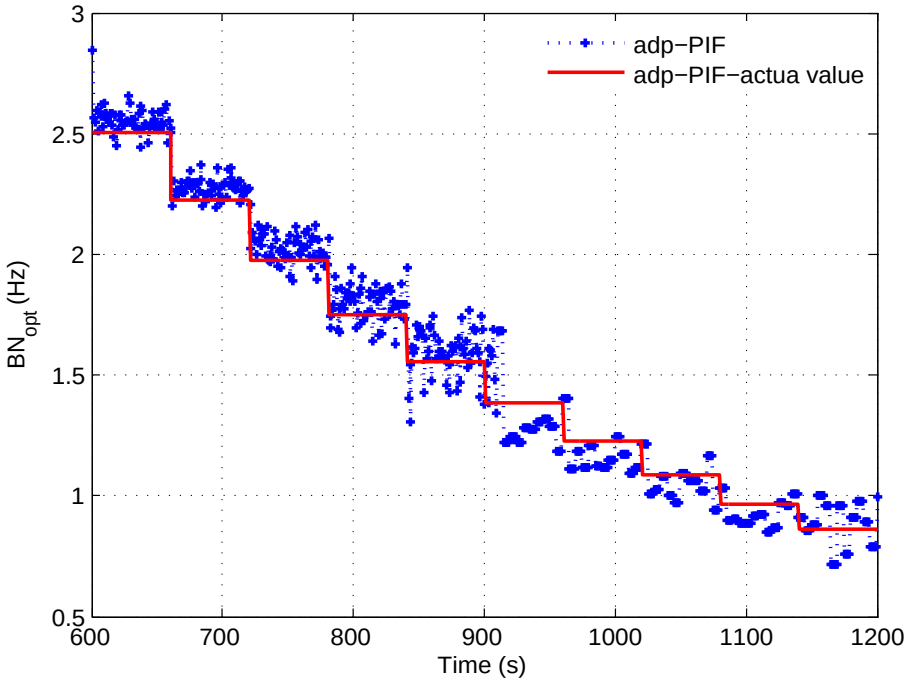

Figure 5.6: The variation of BN_{opt} with C/N_0 in 2-state adaptive PIF-based phase tracking loop.

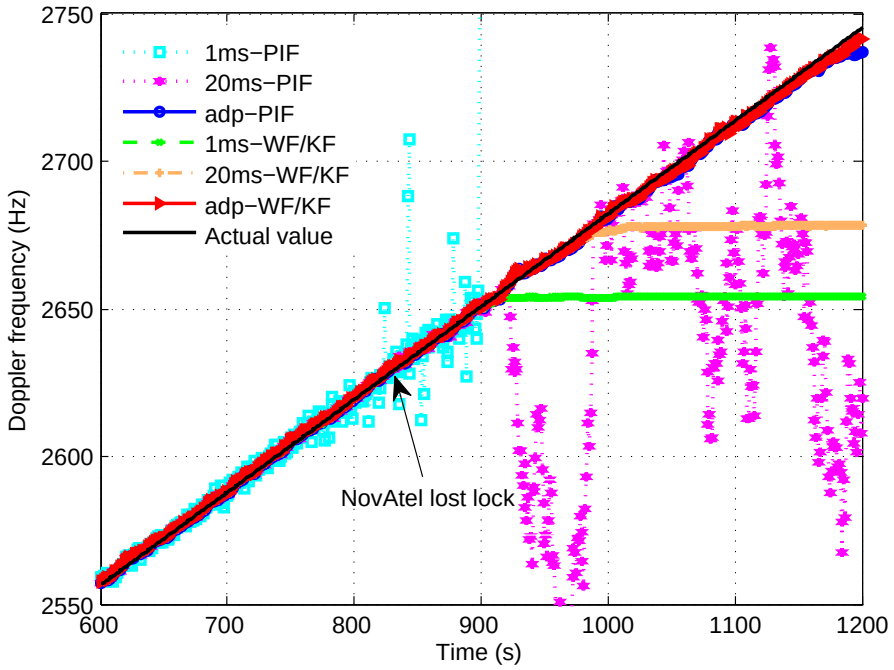

Figure 5.7: Doppler frequency estimations in the 2-state phase tracking loops for PRN 19 satellite signal after 600s ($C/N_0 < 35$dB-Hz) under static weak signal condition. The proposed adaptive phase tracking loops are able to maintain tracking throughout this very challenging time period while other phase tracking loops lose lock gradually when the signal strength decreases with time.

i). A PIF-based phase tracking loop with 1ms and 20ms integration time and 50Hz and 15Hz noise equivalent bandwidth in transit state and steady state, respectively.

ii). A WF/KF-based phase tracking loop with with 1ms and 20ms integration time.

iii). The proposed adaptive PIF and WF/KF-based phase tracking loop with T_{opt} or BN_{opt} according to equations (3.75) and (3.76) and Table 3.2 for HQO and $q_a = 0m^2/s^5$ since this static weak signal is sampled by front-end with HQO.

Using the PRN 19 for illustration, the tracking results using the 2-state phase tracking loops with $\mathbf{L}_{PIF}$, $\mathbf{L}_{WF}$ and $\mathbf{L}_{KF}$ implementations are plotted in Fig.5.4-5.7. The C/N_0 is estimated based on the variance summing method [104], where the C/N_0 was initially measured once at 1Hz rate with 1ms averaging times. Starting at 900s the signal strength is too weak to be measured accurately, 20ms averaging times are used and C/N_0 is estimated for every 5s. From Fig.5.4, we can observe that the estimations of C/N_0 in the adaptive phase tracking loops generally follow the real signal strength variation. The mismatches between estimated and actual C/N_0 in the other phase tracking loops is most likely due to the large frequency tracking errors. Fig.5.5 shows that the values of T_{opt} used in the adaptive PIF- and KF-based phase tracking loops are adaptively increased as the real time estimated C/N_0 decreased. The maximum value of T for adaptive PIF- and KF-based phase tracking loops is $\sim$ 60ms when the estimated C/N_0 is at 17dB-Hz level. This is 10ms shorter than the actual value of T_{opt} obtained from the actual C/N_0 according to equation (3.75). An accurate estimation of C/N_0 is difficult to achieve for weak signals, but the error in C/N_0 does not appear to critically impact optimization results of T_{opt}. Fig.5.6 shows that the values of BN_{opt} used in the adaptive PIF-based phase tracking loop is adaptively decreased as the real time estimated C/N_0 decreases. The minimum value of BN for adaptive PIF-based phase tracking loop is between 0.6Hz and 1Hz when the estimated C/N_0 is at 17dB-Hz level, which is quite close to the theoretical value of BN_{opt} ($\sim$ 0.8Hz) obtained from the actual C/N_0 according to equation (3.76).

From Fig.5.7 we can see that for FL-FT algorithms, the PIF-based phase tracking loop with $T = 1ms$ can maintain lock until 900s when the signal C/N_0 drops to about 25dB-Hz. However, a 1ms integration time is too short for the weak signal tracking after about 900s. By increasing the integration time to 20ms, the PIF-based phase tracking loop has a slight advantage over its 1ms implementation, but still loses lock at about 920s. This indicates that without properly designed filter parameters, the noise rejection caused by increasing the integration time may not be effective. For AL-FT algorithms, the phase

tracking loop with WF/KF is slightly better because the loop gain $\mathbf{L}_{WF}/\mathbf{L}_{KF}$ is adjusted according to the signal strength. The WF/KF-based phase tracking loops with $T = 1ms$ and $T = 20ms$ maintain tracking until 920s and 1000s, which are respectively 20s and 80s longer (2dB better) than that in PIF-based phase tracking loops implementations. The adaptive PIF/WF/KF-based phase tracking loops improve the tracking sensitivity by at least 6dB due to their adaptively self-adjusting integration time and gain matrix. An even longer integration time (>40ms) was invoked in the adaptive phase tracking loops to maintain tracking of the weak signal until the end of the data sequence when C/N_0 reached the 17dB-Hz level.

The NovAtel receiver lost lock at an attenuation level of -19dB ($C/N_0 = 27$dB-Hz) at about 840 seconds. The results indicate that the adaptive phase tracking loops outperforms FL-FT and AL-FT algorithms, validating the state space design and optimization analysis for generalized phase tracking loop under weak signal condition for a receiver with HQO.

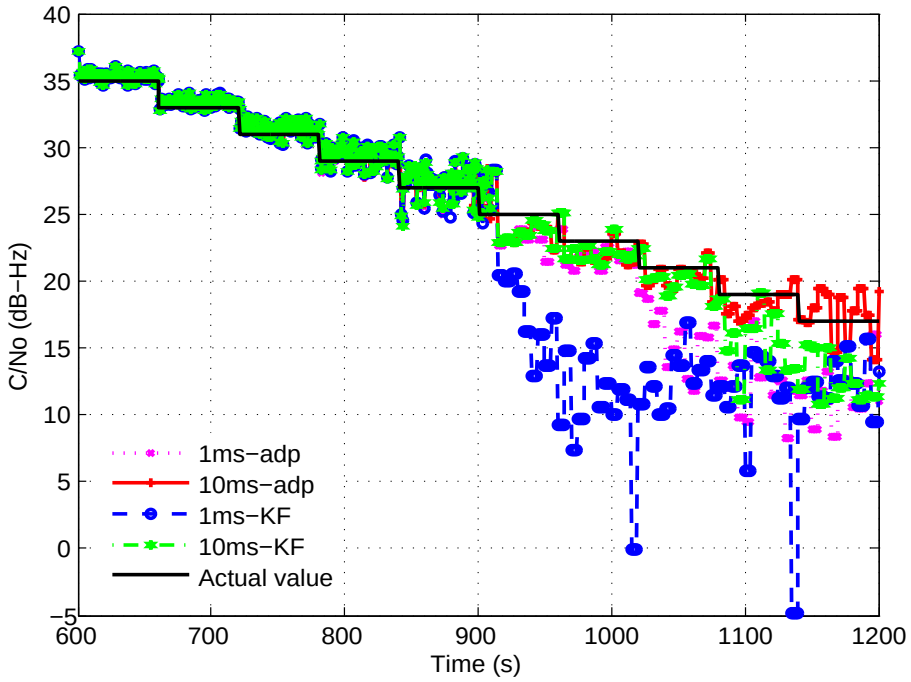

Figure 5.8: C/N_0 estimations variation in 1-state frequency tracking loops for PRN 19 satellite signal after 600s ($C/N_0 < 35$dB-Hz) under static weak signal condition. The estimated C/N_0 is used to tune BW_{opt} in adaptive frequency tracking loops as well as measurement noise covariance matrix $\mathbf{R}$ in KF-based frequency tracking loops.

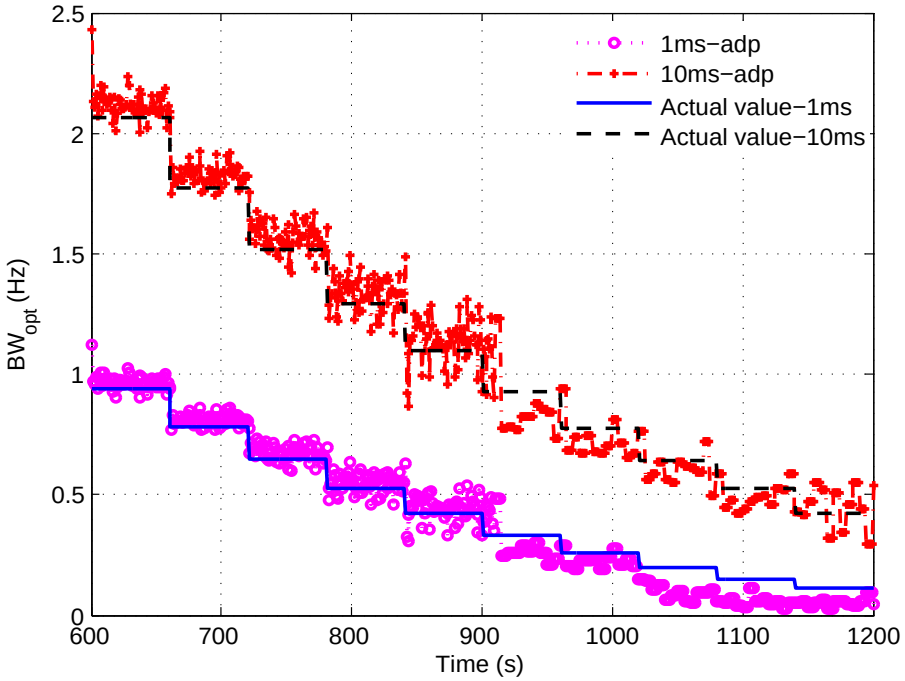

Figure 5.9: The variation of BW_{opt} with C/N_0 in adaptive PIF-based frequency tracking loop.

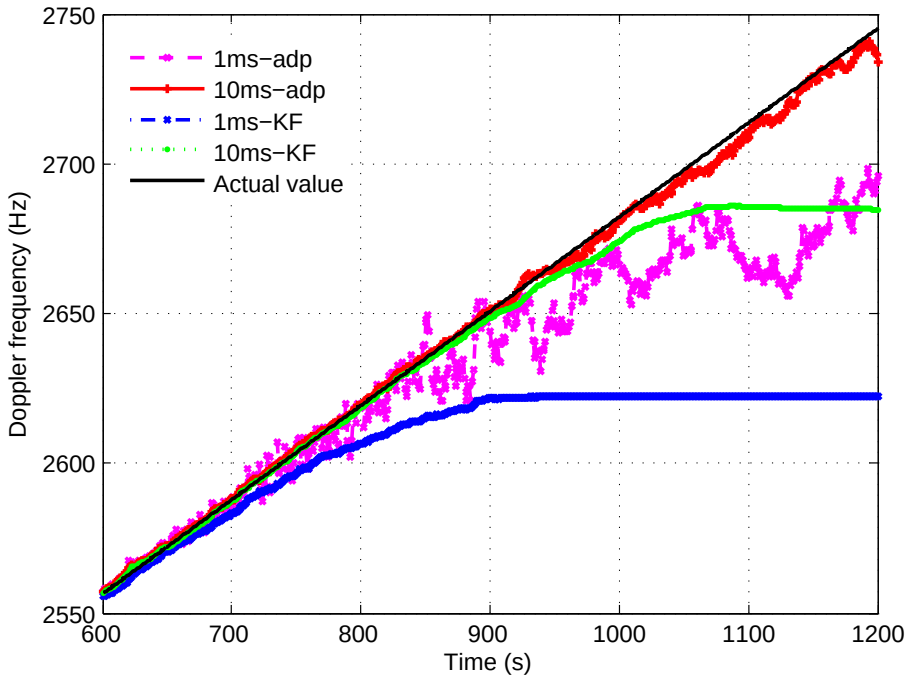

Figure 5.10: Doppler frequency estimations in 1-state frequency tracking loops for PRN 19 satellite signal after 600s ($C/N_0 < 35$dB-Hz) under static weak signal condition. The optimized frequency tracking loops are better than the KF-based frequency tracking loops for both $T = 1ms$ and $10ms$.

2). Adaptive frequency tracking loop scheme: The 1-state adaptive frequency tracking loops with $T = 1ms$ and $10ms$ and the corresponding value of BW_{opt} are adopted to process this static weak signal. The KF-based frequency tracking loops with $T = 1ms$ and $10ms$ in [30] are also shown in the figure. Note that the KF-based frequency tracking loop does not take into consideration of the non-white noise characteristics of frequency estimation noise. It is shown here for comparison purposes.

Using the PRN 19 for illustration, Fig.5.8 shows that the estimations of C/N_0 with $T = 10ms$ follow the real signal strength trend more accurately than other approaches, especially when the signal strength is low. Fig.5.9 shows that BW_{opt} for both $T = 1ms$ and $10ms$ adaptively decreases as C/N_0 decreases, with BW_{opt} being slighter lower for $T = 1ms$ than for $10ms$ especially when the signal is weak. Fig.5.10 shows that as signal strength decreases, the frequency error increases. This trend is particularly obvious for $T = 1ms$ after about 700 seconds (C/N_0=33dB-Hz) in the KF-based frequency tracking loop and 1000 seconds (C/N_0=23dB-Hz) in the adaptive PIF-based frequency tracking loop. This is in disagreement with the theoretical analysis in Table 4.1 which shows that the adaptive frequency tracking loop could track a weak signal as low as 0dB-Hz. This disagreement can be attributed to errors in the assumption C/N_0 estimation. The maximum frequency error in the 1ms frequency tracking loop can be as much as 42Hz as compared to the frequency error threshold. In the real implementation, this large frequency error degrades the C/N_0 estimations. To improve the tracking accuracy and to reduce C/N_0 estimation errors when the signal is weak, longer integration times such as $T = 10ms$ should be used. Using $T = 10ms$, the KF-based frequency tracking loop lost lock at 1000 seconds (C/N_0=23dB-Hz), while the adaptive PIF-based frequency tracking loop maintains tracking through out the time period. The theoretical analysis is based on the rules that 3-sigma frequency jitter should be less than one-forth of the frequency pull-in range of the frequency discriminator. It indeed shows that the theoretical tracking sensitivity is close to 0dB-Hz. However, in the real implementation, the large frequency error degrades the I and Q accumulation energy which affects both the C/N_0 estimation and frequency error measurement. Simulation results show that the frequency tracking results deviate from the theoretical prediction, suggesting that more research is required to bridge the gap.

The better performance of the adaptive PIF-based frequency tracking loop over KF-based frequency tracking loop validates the state space design and optimization analysis for generalized FLL under the static and weak signal condition for a receiver front-end with

HQO. Comparing Fig.5.10 to Fig.5.7, the adaptive frequency tracking loop with $T = 10ms$ is equivalent to the adaptive PIF-based phase tracking loop with a maximum 60ms integration time and better than the KF-based phase tracking loop with $T = 20ms$. It shows that even with shorter integration time, a well-designed frequency tracking loop is superior to or at least equivalent to a well-designed phase tracking loop in weak signal processing.

5.2.2 dynamic weak signal scenario

In this simulation, signal attenuation and dynamics are applied simultaneously, as can be seen in Fig.5.11. For signal attenuation, the signal power starts at the nominal 46dB-Hz level and was decreased by 1dB per 5s starting at 20s. The maximum attenuation reaches 20dB at $t = 120$s and maintained at this level for 60s, followed by a recovery period with 1dB per 5s until it reaches back to the nominal level. For signal dynamics simulation, the receiver is static in the first 20s, then it starts moving to the east with an acceleration of $50m/s^2$ for 100s. When $t = 120$s, the acceleration is at zero with a negative jerk of $50m/s^3$. After this, the receiver remains at a constant velocity until $t = 180$s, then it slows down with negative acceleration for 100s and stops at $t = 280$s. The RF front-end with LQO collects the data with an IF at 4.309MHz, sampling frequency at 12MHz, and stored in 1-bit resolution for post-processing. Note that this scenario may not be very common in practice, we just want to use to this profile to have a preliminary verification of our adaptive tracking loop performance when the weak signal and high dynamic coincide. The further real data test will be conducted in future.

1). Adaptive phase tracking loop scheme: Three types of 3-states phase tracking loops are evaluated for dynamic weak signal processing. They are:

i). A PIF-based phase tracking loop with 1ms and 20ms integration times. A 50Hz noise equivalent bandwidth is used in both the transit- and steady-state respectively.

ii). A WF/KF-based phase tracking loop with 1ms and 20ms integration times and corresponding q_a values for the dynamic scenarios described above and estimated using equation (3.12).

iii). The proposed adaptive PIF and WF/KF-based phase tracking loop with T_{opt} or BN_{opt} computed according to equations (3.75) and (3.76) and Table 3.2 for the case of $q_a = 10m^2/s^5$ and a receiver with LQO.

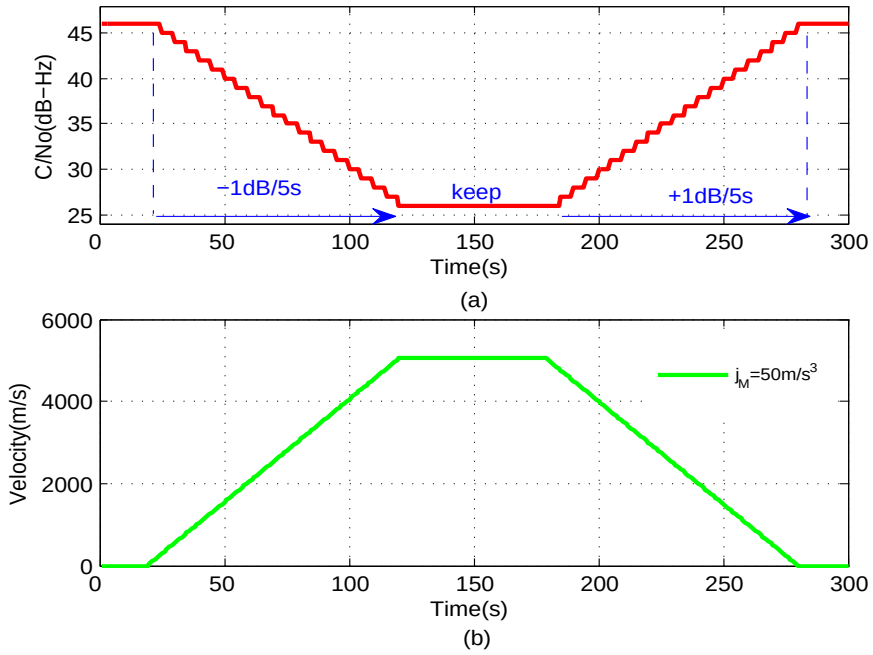

Figure 5.11: The signal C/N_0 and platform velocity in dynamic weak signal scenario. (a). The variation of signal C/N_0; (b). The variation of platform dynamics with maximum jerk of $\pm 50 m/s^3$.

Fig.5.12 shows that the estimated C/N_0 in all three adaptive phase tracking loops in general follows the real signal strength variations. The mismatch between estimated and real C/N_0 in all non-adaptive phase tracking loops is most likely due to the large frequency tracking errors.

Fig.5.13 and 5.14 show that the values of T_{opt} and BN_{opt} in the adaptive phase tracking loops are automatically tuned according to C/N_0 estimations, although there are some discrepancies between the theoretically computed T_{opt} and the actual T_{opt} according to equations (3.75) and (3.76) adopted by the tuning process. For example, the theoretical T_{opt} is 7ms and 8ms for the PIF- and WF-based adaptive phase tracking loops respectively when C/N_0 is 26dB-Hz. In the real implementation, T_{opt} is at about $10ms$ due to an inaccurate C/N_0 estimation when the signal is weak. Fig.5.13 shows that the minimum value of BN for adaptive PIF-based phase tracking loop is between 11Hz and 15Hz in real implementations, which is quite close to the theoretical value of BN_{opt} ($\sim$ 12Hz) obtained based on the actual C/N_0. Hence, the error in the C/N_0 estimation does not appear to

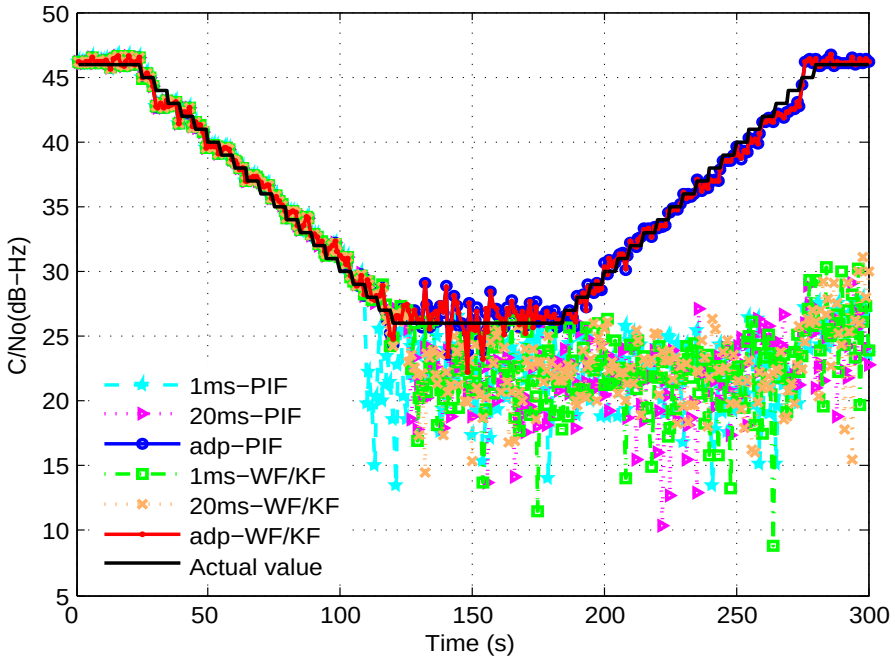

Figure 5.12: C/N_0 estimations variation in 3-state phase tracking loops for PRN 14 satellite signal under dynamic weak signal condition. The estimated C/N_0 is used to tune T_{opt} and BN_{opt} in adaptive phase tracking loops as well as measurement noise covariance matrix $\mathbf{R}$ in WF/KF-based phase tracking loops.

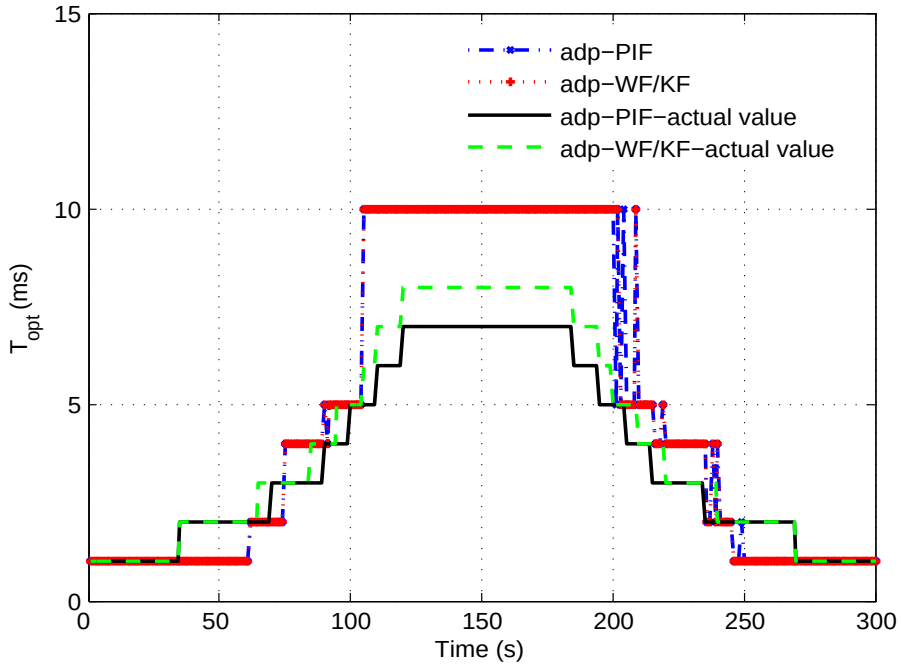

Figure 5.13: The variation of T_{opt} with signal C/N_0 in 3-state adaptive PIF- and WF/KF-based phase tracking loops.

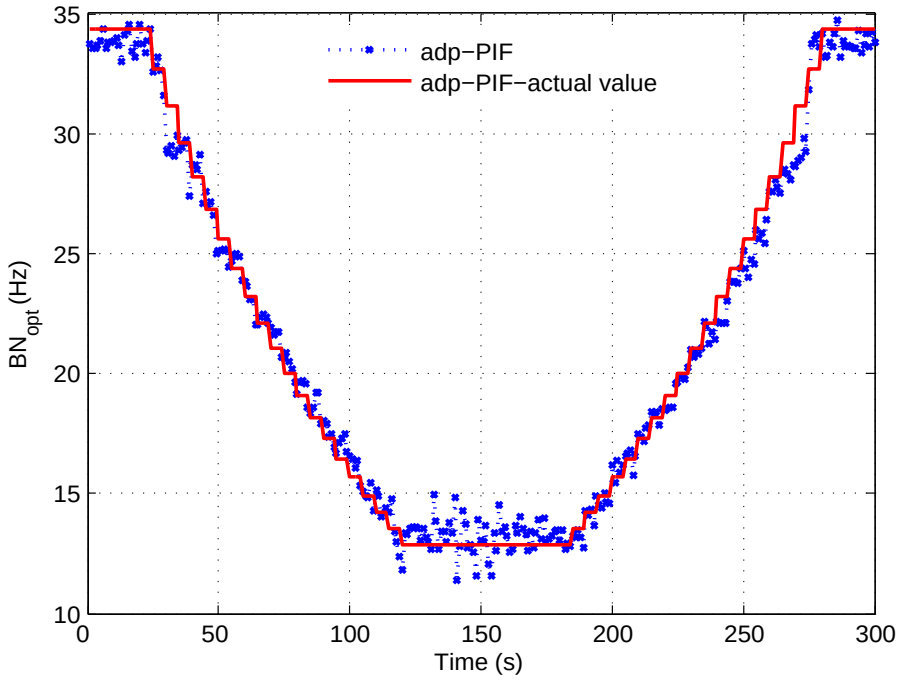

Figure 5.14: The variation of BN_{opt} with signal C/N_0 in 3-state adaptive PIF-based phase tracking loop.

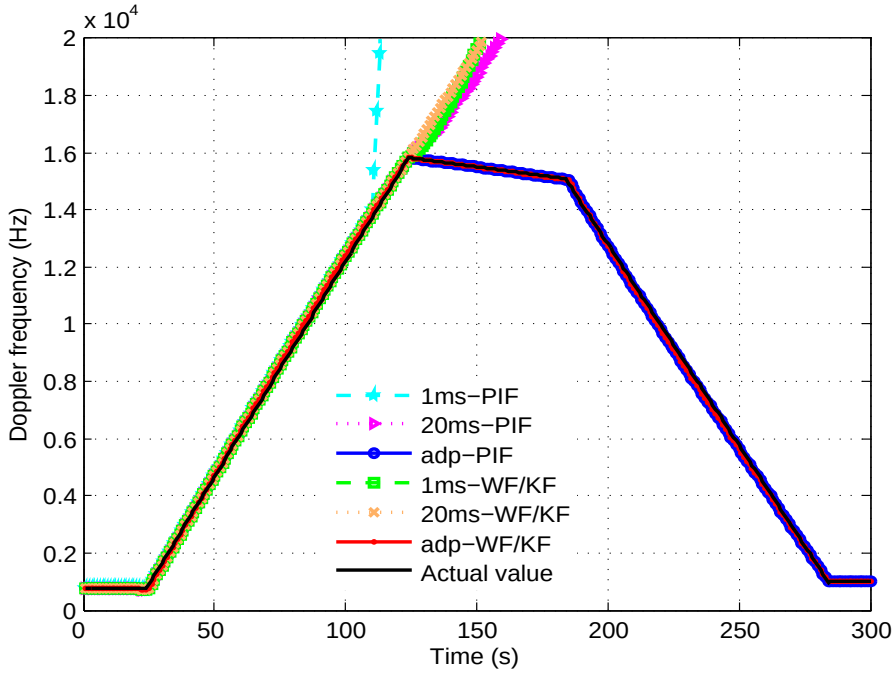

Figure 5.15: Doppler frequency estimations in 3-state phase tracking loops for PRN 14 satellite signal under dynamic weak signal condition. Only the proposed adaptive phase tracking loops are able to maintain tracking while others have lost lock.

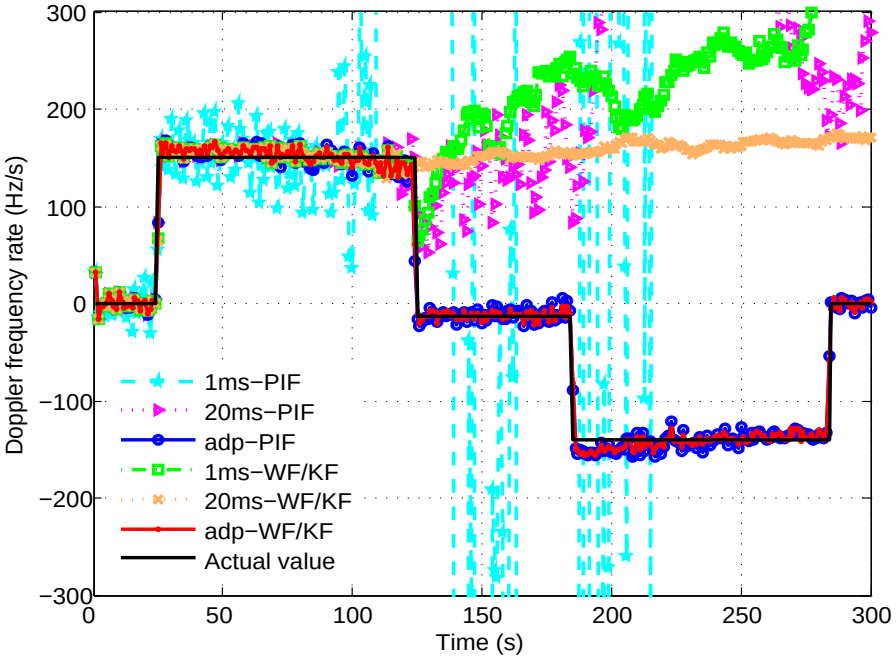

Figure 5.16: Doppler frequency rate estimations in 3-state phase tracking loops for PRN 14 satellite signal under dynamic weak signal condition. Only the Doppler frequency rate estimations in the proposed adaptive phase tracking loops the generally follow the signal dynamic, while others have diverged after 120s.

critically impact the optimization results for T_{opt} and BN_{opt}.

Fig.5.15 shows the Doppler frequency estimations of the 3-state phase tracking loops, where the maximum changes of Doppler frequency are about 15000Hz during acceleration from 20s to 120s and -14000Hz during deceleration from 180s to 280s. A loss-of-lock occurs in the PIF-based PLL with $T = 1ms$ at about 110s. Using a longer time integration, such as $T = 20ms$ enables the PIF-based phase tracking loop to maintain lock for 10s longer (2dB better). The WF/KF-based phase tracking loop with a variable gain demonstrates improved performance. For example, for $T = 1ms$, the WF/KF-based phase tracking loop is about 2dB better than the PIF-based phase tracking loop in tracking sensitivity. This observation shows that WF/KF has the potential to achieve better noise performance due to its narrow equivalent noise bandwidth than the model-free approach PIF. However, the same conclusion doesn't hold any more when jerk starts at 120s. The WF/KF-based phase tracking loop with $T = 20ms$ loses lock almost at the same time with $20ms$ PIF-based phase tracking loop. Since as C/N_0 decreases, the noise equivalent bandwidth in WF/KF-based phase tracking loop decreases. Hence, the narrower noise equivalent bandwidth in WF/KF degrades the dynamic adaptability when dynamic stress occurs. Moreover, longer integration time, such as $T = 20ms$ even makes worse in dynamic signal tracking.

Fig.5.16 shows the estimated Doppler rate. It can be seen that the Doppler rate estimations are consistent with the actual rates for the adaptive schemes, while the estimations from non-adaptive approaches deviate from the true values at different times. The adaptive schemes also accurately estimated the receiver's jerks at 20s, 120s, 180s and 280s.

The superior performance of the adaptive phase tracking loops over FL-FT algorithm and AL-FT algorithm validates the state space design and optimization analysis for generalized phase tracking loop for dynamic weak signals using a receiver with LQO.

2). Adaptive frequency tracking loop scheme: The 2-state adaptive frequency tracking loops with $T = 1ms$ and $10ms$ are adopted to process this dynamic weak signal. KF-based frequency tracking loops with $T = 1ms$ and $10ms$ are also tested for the performance comparison purposes. The values of q_a are set as $1m^2/s^5$ and $10m^2/s^5$ to represent signal dynamics described by equation (3.12) for $T = 1ms$ and $10ms$, respectively.

Fig.5.17 shows that the estimations of C/N_0 in the adaptive frequency tracking loops generally follow the real signal strength variation. The mismatch between the estimated and real C/N_0 in the KF-based frequency tracking loops is most likely due to the large frequency

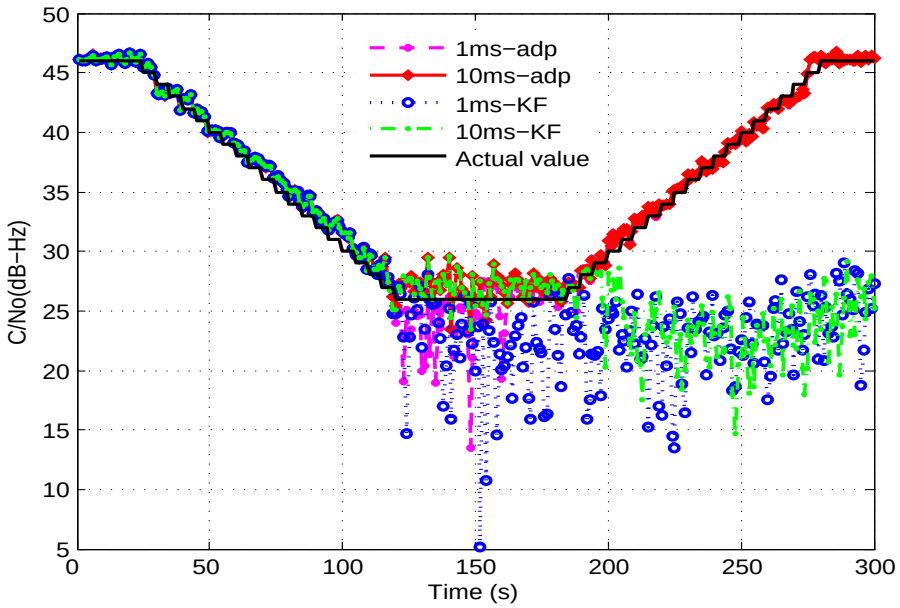

Figure 5.17: C/N_0 estimations in 2-state frequency tracking loops for PRN 14 satellite signal under dynamic weak signal condition. The estimated C/N_0 is used to tune BW_{opt} in adaptive frequency tracking loops as well as measurement noise covariance matrix $\mathbf{R}$ in KF-based frequency tracking loops.

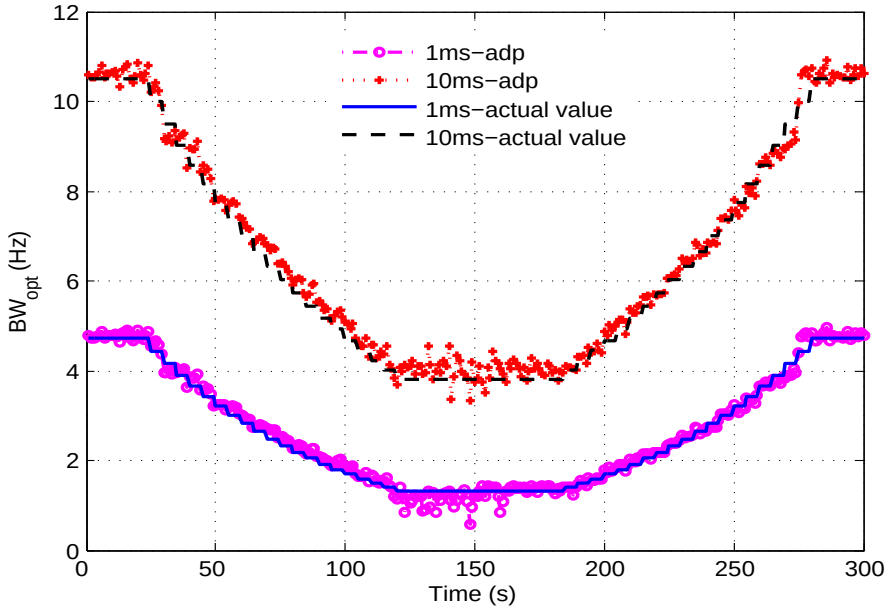

Figure 5.18: The variation of BW_{opt} with C/N_0 in adaptive 2-state PIF-based frequency tracking loops.

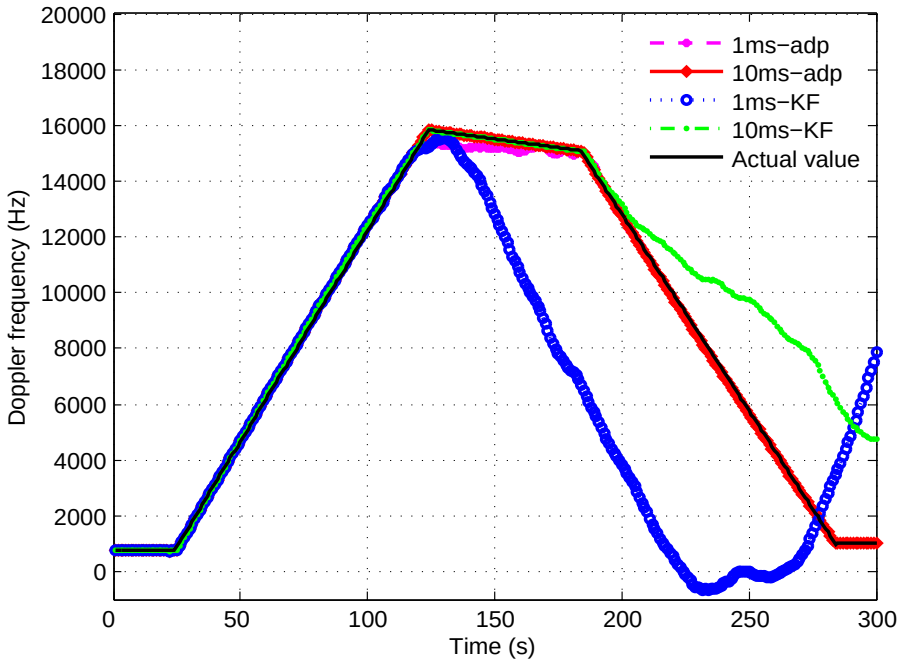

Figure 5.19: Doppler frequency estimations in 2-state frequency tracking loops for PRN 14 satellite signal under dynamic weak signal condition. Only the proposed adaptive frequency tracking loops are able to maintain tracking while KF-based frequency tracking loops with $T = 1ms$ and $10ms$ respectively lost of lock after 120s and 180s.

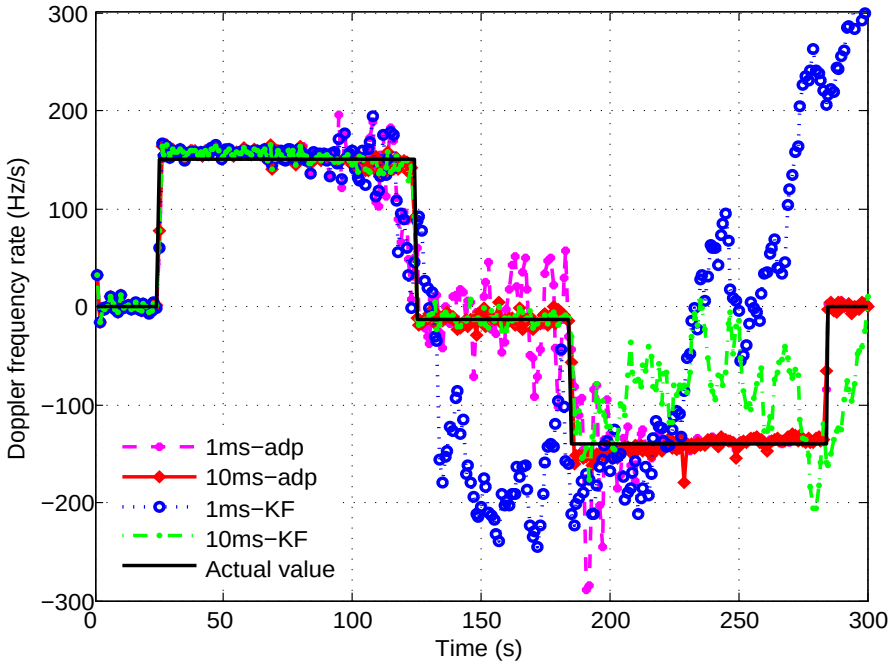

Figure 5.20: Doppler frequency rate estimations in 2-state frequency tracking loops for PRN 14 satellite signal under dynamic weak signal condition. Only the Doppler frequency rate estimations in the proposed adaptive frequency tracking loops the generally follow the signal dynamic while KF-based frequency tracking loops with $T = 1ms$ and $10ms$ respectively diverge after 120s and 180s.

tracking errors. Fig.5.18 shows that the values of BW_{opt} used in the adaptive frequency tracking loops are automatically tuned according to the real time C/N_0 estimations, and these values generally follow the theoretical values that obtained for the actual C/N_0. Again, BW_{opt} with $T = 1ms$ is smaller than that with $T = 10ms$. Fig.5.19 shows the KF-based frequency tracking loops with $T = 1ms$ and $10ms$ lost lock at about 120s and 180s, respectively, while the adaptive frequency tracking loops maintain tracking throughout the time period. However, there are some frequency errors when $T = 1ms$ due to the inaccurate measurements when the signal is weak from 120s to 180s. Fig. 5.20 shows that the Doppler frequency rate estimations in the KF-based frequency tracking loops with $T = 1ms$ and $10ms$ deviate from the truth after 120s and 200s, respectively. The estimations in the adaptive PIF-based frequency tracking loop with $T = 1ms$ follows the signal dynamics in general, but with some disturbance from 80s to 220s when C/N_0 drops to 26dB-Hz. A frequency tracking loop with short integration time may be adequate to satisfy the weak and dynamic signal tracking requirement, but may be at the risk of having a lower tracking accuracy. With a longer integration time, such as $T = 10ms$, the estimations in the adaptive frequency tracking loop are more accurate throughout the time period.

The above results show that the adaptive frequency tracking loop perform better than the KF-based frequency tracking loop for dynamic weak signals using a receiver front end with a LQO. Comparing the Doppler frequency and frequency rate estimations in adaptive PIF-based phase tracking loop in Fig. 5.15-5.16 with that in adaptive PIF-based frequency tracking loop in Fig. 5.19-5.20 for $C/N_0 = 26$dB-Hz shows that the 2-state PIF-based frequency tracking loop with $T = 10ms$ and BW_{opt} at about 4Hz achieves equivalent tracking performance to that of the 3-state PIF-based phase tracking loop with BN_{opt} at about 12Hz and T_{opt} at 10ms . Both tracking loops perform better than the 2-state PIF-based frequency tracking loop with $T = 1ms$ and BW_{opt} at about 1.8Hz.

Chapter 6

Conclusions and Future Work

6.1 Conclusion

In this thesis, we established a generalized carrier tracking loop architecture from a control system perspective. A state space model and state feedback/state estimator design approach for general carrier tracking loop problem were studied. Two generalized carrier tracking loops, namely, the generalized phase tracking loop and the generalized frequency tracking loop, were designed, analyzed, and optimized.

In generalized phase tracking loop design, three traditional filter design methods, i.e., PIF, WF, and KF were presented and unified within the state space framework. The relationships between their corresponding state estimator gain matrices and parameters, such as the integration time, the loop bandwidth, dynamic parameter, and the oscillator h-parameters, were derived. Our analysis demonstrated the well-known fact that WF and KF designs are equivalent under the assumption of white Gaussian noise in the time-invariant linear systems, i.e., the WF state estimator gain is an exact closed form expression for the steady-state KF gain. Based on the MMSE criteria, the phase tracking loop with PIF, WF, and KF were optimized to improve the tracking sensitivity and dynamic responses. For the convenience of actual implementations, the relationships between the optimal integration time, T_{opt} and C/N_0, the optimal phase tracking loop bandwidth, BN_{opt}, and C/N_0 for different dynamics and oscillator qualities were provided to facilitate the phase tracking loop design. The phase tracking sensitivity limits of these tracking loops were obtained in terms of the 3-sigma rule. We demonstrated that if a 2-state model is used in

static environment, the optimized PIF, WF, and KF can be tuned to achieve comparable performance. The maximum tracking sensitivity is limited by the oscillator quality, where the tracking sensitivity limits of the receivers with HQO are as much as 6dB-Hz in pilot channel and 13dB-Hz in data channel, respectively, which are 9dB higher than that of the receivers with LQO. If a 3-state model is used in dynamic environment, the optimized WF and KF are equivalent and slightly better than the optimized PIF. We analytically demonstrated that the tracking sensitivity deteriorates as the platform dynamic increases. These results demonstrated that under the uniform optimization criteria, the phase tracking loop performance is mainly limited by the oscillator quality and platform dynamics, regardless of PIF, WF, or KF design approaches.

In generalized frequency tracking loop design, taking the non-white noise characteristic into account, the PIF design was formulated in the state space framework. Performance metrics, such as frequency tracking error variance and dynamic stress error, were derived to evaluate the performance of frequency tracking loop designs under the effects of thermal noise, oscillator noise, and platform dynamics. Relationships between the optimal frequency tracking loop bandwidth, BW_{opt}, and C/N_0 for different dynamics and integration time were provided to facilitate the frequency tracking loop design. Based on the MMSE criteria, the frequency tracking loop with PIF was optimized to improve the frequency tracking performance. Theoretical analysis showed that the oscillator noise has a minor effect on frequency tracking loop performance and the frequency tracking loop has at least 6dB improvement in tracking sensitivity compared to the phase tracking loop with the same signal dynamics.

Following this theoretical analysis, an adaptive phase tracking scheme and also an adaptive frequency tracking scheme to track weak and high dynamic signals were proposed. Two case studies using simulator to generate signals with high receiver platform dynamics and low signal power were conducted to verify the theoretical analysis, as well as the adaptive tracking schemes. The simulation results confirmed that: (1) the adaptive phase tracking scheme is superior to the traditional PLL; (2) the adaptive frequency tracking scheme is superior to the traditional KF-based FLL; (3) the 1-state adaptive frequency tracking loop with a 10ms integration time achieves almost equivalent tracking performance with the 2-state adaptive phase tracking loop with adaptive integration time (60ms maximum) for C/N_0 as low as 17dB-Hz under the static scenario; (4) the 2-state adaptive frequency tracking loop with a 10ms integration time and BW_{opt} at about 4Hz achieves an equivalent

tracking performance to that of the 3-state PIF-based phase tracking loop with BN_{opt} at about 12Hz and T_{opt} at 10ms. Both tracking loops perform better than the 2-state PIF-based frequency tracking loop with $T = 1ms$ and BW_{opt} at about $\sim$1.8Hz for C/N_0 as low as 26dB-Hz under a maximum $50m/s^3$ jerk dynamic condition. These results validate the effectiveness of optimized loop parameters selection and demonstrate that the adaptive phase tracking and the adaptive frequency tracking schemes can enhance the tracking performance in challenging environments with weak signal and/or dynamic receiver motion.

6.2 Future Work

A number of open questions and unresolved issues, have been identified and further research are suggested here.

1. The performance of the proposed adaptive carrier tracking algorithm depends on good signal C/N_0 estimation. However, in the presence of multipath fading or interference, the C/N_0 estimation may be affected by large signal level fluctuations due to constructive interference. The adaptive filter weighs these unreliable estimates more strongly due to the high C/N_0 and the tracking loop quickly can become unstable. Therefore, to improve the carrier tracking robustness and reliability, robust C/N_0 estimation methodology and improved carrier tracking algorithms to mitigate interference and multipath effects need to be further investigated. Additionally, the C/N_0 estimator is derived under the assumptions of perfect frequency synchronization, data bit aiding and constant signal phase during the observation window. However, in the frequency tracking loop, larger frequency errors may degrade the C/N_0 estimator accuracy which finally deteriorate the tracking performance. A sensitivity experiment that shows how C/N_0 is affected by frequency error is required.

2. The state feedback design analysis in Chapter 3 shows that when $\mathbf{B}$ is chosen as $[0; 1]$ or $[1; 1]$, the control plant effectively corresponds to a single-input NCO, i.e., the rate-only feedback NCO or the phase and rate feedback NCO in traditional PLL design. Furthermore, the state space design framework also enables the multi-input NCO operation, such as $\mathbf{B} = \mathbf{I}$. The selection of $\mathbf{B} = \mathbf{I}$ and $\mathbf{K} = \mathbf{A}$ simplifies the error state estimation and enables us to cast the traditional PLL design to the state space framework. However, from control system design perspective, other possible

B and **K** selections that ensure system controllability and stability can be adopted as well in order to satisfy the specific system performance, such as robustness. The different **B** and **K** selections need to be studied to improve the tracking loop design.

3. The state estimator design analysis in Chapter 3 and Chapter 4 shows that the corresponding state estimator gain matrices are obtained by casting the traditional single-input single-output tracking loop designs, such as PIF- and WF-based PLL and PIF-based FLL, to the state space tracking architecture. It is known that the state space framework is more general and enables the multiple-input multiple-output control system design. Hence, many other filter techniques and estimation approaches, such as LSE [32] and MHE [98] based on the multiple phase error or frequency error measurements, could be used to design the state estimator. Additionally, the combination of the phase and frequency tracking loop, which is known as FLL-assist-PLL, could be designed by using the modelling, design, and optimization techniques presented in this thesis to improve the carrier tracking ability.

4. Optimization analysis in Chapter 3 and Chapter 4 shows that different design approaches can be unified, evaluated, and compared within the general state space framework. The optimized performances in these tracking loops are equivalent and the tracking limits of carrier tracking loop design is ultimately determined by signal models. Accurate model is key to improve the tracking performance of tracking loops. This thesis only considers the simplest case that the measurement noise is white Gaussian noise and assumed to be uncorrelated with the system noise, such as oscillator noise and dynamics. However, the time-correlated clock errors [103] which represent the correlation between measurement noise and process noise, will affect the system performance particularly for longer integration times. Besides, there are various error sources, such as interference [101] and ionospheric scintillation [102], that corrupt and distort carrier measurements in real world applications. In the dynamic scenario, the dynamic stress (g-sensitive) errors or platform vibration-induced errors also have significant influence on the carrier signal. These errors should be considered in the signal models in order to improve the carrier tracking performance.

List of Publications

[1] **R. Yang**, K. V. Ling, E. K. Poh, and Y. Morton, "*Generalized GNSS Signal Carrier Tracking: Part I: Modelling and Analysis*," accepted by IEEE Transactions on Aerospace and Electronic Systems, January, 2017.

[2] **R. Yang**, Y. Morton, K. V. Ling, and E. K. Poh, "*Generalized GNSS Signal Carrier Tracking: Part II: Optimization and Implementation*," accepted by IEEE Transactions on Aerospace and Electronic Systems, January, 2017.

[3] **R. Yang**, Y. Wang, L. Cong, K. V. Ling, and E. K. Poh. "*Integration Time Analysis for High Sensitivity Kalman Filter Based Tracking Loop*," *2015 Pacific PNT, Honolulu, Hawaii*, April 2015.

[4] **R. Yang**, K. V. Ling, and E. K. Poh. "*NCO Models for Tracking Loop Design in GNSS Software Receiver*," *2014 IEEE/ION PLANS, Monterey, California*, May 2014.

[5] **R. Yang**, K. V. Ling, and E. K. Poh. "*Optimal combination of coherent and non-coherent acquisition of weak GNSS signals*," *2013 Pacific PNT, Honolulu, Hawaii*, April 2013.

[6] Y. Wang, **R. Yang**, K. V. Ling, and E. K. Poh, "*Robust Vector Tracking Loop Using Moving Horizon Estimation*," , *2015 Pacific PNT, Honolulu, Hawaii*, April 2015.

Bibliography

[1] William C Stone. *Electromagnetic signal attenuation in construction materials*. US Department of Commerce, National Institute of Standards and Technology, Building and Fire Research Laboratory, 1997.

[2] Gonzalo Seco-Granados, José A López-Salcedo, David Jiménez-Baños, and Gustavo López-Risueño. Challenges in indoor global navigation satellite systems: Unveiling its core features in signal processing. *Signal Processing Magazine, IEEE*, 29(2):108–131, 2012.

[3] James T Curran, Gerard Lachapelle, and Colin C Murphy. Improving the design of frequency lock loops for GNSS receivers. *Aerospace and Electronic Systems, IEEE Transactions on*, 48(1):850–868, 2012.

[4] Cillian ODriscoll, Mark G Petovello, and Gérard Lachapelle. Choosing the coherent integration time for Kalman filter-based carrier-phase tracking of GNSS signals. *GPS solutions*, 15(4):345–356, 2011.

[5] Phillip W Ward. Performance comparisons between FLL, PLL and a novel FLL-assisted-PLL carrier tracking loop under RF interference conditions. In *Proceedings of the 11th International Technical Meeting of the Satellite Division of The Institute of Navigation (ION GPS 1998)*, pages 783–795, 1998.

[6] Pratap Misra and Per Enge. *Global Positioning System: Signals, Measurements and Performance Second Edition*. Lincoln, MA: Ganga-Jamuna Press, 2006.

[7] Daniele Borio. A statistical theory for GNSS signal acquisition. 2008.

[8] Elliott D Kaplan and Christopher J Hegarty. *Understanding GPS: principles and applications*. Artech house, 2005.

[9] James Bao-Yen Tsui. *Fundamentals of Global Positioning System Receivers: A Software Approach, Second Edition*. John Wiley and Sons Ltd, 2005.

[10] Cillian O'Driscoll. *Performance analysis of the parallel acquisition of weak GPS signals*. PhD thesis, 2007.

[11] Fabio Dovis, Gerard Lachapelle, Daniele Borio, and Anna Martinetti. Comparison of standard and generalized post-correlation differentially coherent detection strategies for weak GNSS signal acquisition. Master's thesis, 2009.

[12] Shashank Satyanarayana. *GNSS channel characterization and enhanced weak signal processing*. PhD thesis, University of Calgary, 2011.

[13] Tian Jin, Fangyao Lu, Yang Liu, Honglei Qin, and Xiling Luo. Double differentially coherent pseudorandom noise code acquisition method for code-division multipleaccess system. *Signal Processing, IET*, 7(7):587–597, 2013.

[14] Feng Xu and Yang Gao. A new GNSS acquisition method with signal down sampling in frequency domain. In *Vehicular Technology Conference, 2009. VTC Spring 2009. IEEE 69th*, pages 1–5. IEEE, 2009.

[15] Rong Yang, Keck Voon Ling, and Eng Kee Poh. Optimal combination of coherent and non-coherent acquisition of weak GNSS signals. In *Pacific PNT*, Honolulu, Hawaii, USA, April 2013. ION.

[16] James T Curran. *Weak signal digital GNSS tracking algorithms*. PhD thesis, National University of Ireland, 2010.

[17] Bradford W Parkinson and James J Spilker. *Global Positioning System: Theory and Applications (volume One)*, volume 1. Aiaa, 1996.

[18] JAMES T Curran, GÉRARD Lachapelle, and COLIN C Murphy. Digital GNSS PLL design conditioned on thermal and oscillator phase noise. *Aerospace and Electronic Systems, IEEE Transactions on*, 49(1):687–687, 2013.

[19] Alireza Razavi, Demoz Gebre-Egziabher, and Dennis M Akos. Carrier loop architectures for tracking weak GPS signals. *Aerospace and Electronic Systems, IEEE Transactions on*, 44(2):697–710, 2008.

[20] Pejman Lotfali Kazemi. *Development of new filter and tracking schemes for weak GPS signal tracking*. PhD thesis, University of Calgary, 2010.

[21] Tian Jin and JunXing Ren. Stability analysis of GPS carrier tracking loops by phase margin approach. *GPS solutions*, 17(3):423–431, 2013.

[22] Weihua Zhuang. *Composite GPS receiver modelling, simulations and applications*. PhD thesis, University of New Brunswick, 1993.

[23] SA Stephens and JB Thomas. Controlled-root formulation for digital phase-locked loops. *Aerospace and Electronic Systems, IEEE Transactions on*, 31(1):78–95, 1995.

[24] JB Thomas. An analysis of digital phase-locked loops. 1989.

[25] José A López-Salcedo, Del Peral-Rosado, Gonzalo Seco-Granados, et al. Survey on robust carrier tracking techniques. *Communications Surveys and Tutorials, IEEE*, 16(2):670–688, 2014.

[26] Weihua Zhuang. Performance analysis of GPS carrier phase observable. *Aerospace and Electronic Systems, IEEE Transactions on*, 32(2):754–767, 1996.

[27] Daniele Borio and Gérard Lachapelle. A non-coherent architecture for GNSS digital tracking loops. *annals of telecommunications-annales des télécommunications*, 64(9-10):601–614, 2009.

[28] Daniele Borio, Nadezda Sokolova, and Gérard Lachapelle. Memory discriminators for non-coherent integration in GNSS tracking loops. In *Proc. European Navigation Conf. ENC*, volume 9, 2009.

[29] Cillian ODriscoll and Gérard Lachapelle. Comparison of traditional and Kalman filter based tracking architectures. In *Proceedings of European navigation conference*, pages 3–6, 2009.

[30] Jong-Hoon Won, Dominik Dötterböck, and Bernd Eissfeller. Performance comparison of different forms of Kalman filter approaches for a vector-based GNSS signal tracking loop. *Navigation*, 57(3):185–199, 2010.

[31] Jong-Hoon Won, Thomas Pany, and Bernd Eissfeller. Characteristics of Kalman filters for GNSS signal tracking loop. *Aerospace and Electronic Systems, IEEE Transactions on*, 48(4):3671–3681, 2012.

[32] Brian DO Anderson and John B Moore. *Optimal filtering*. Courier Dover Publications, 2012.

[33] Pejman L Kazemi. Optimum digital filters for GNSS tracking loops. In *Proceedings of international technical meeting of the Satellite Division of the Institute of Navigation (ION GNSS), Savannah, GA*, pages 16–19, 2008.

[34] Del Peral-Rosado, José A López-Salcedo, Gonzalo Seco-Granados, José M López-Almansa, Joaquın Cosmen, et al. Kalman filter-based architecture for robust and high-sensitivity tracking in GNSS receivers. In *Satellite Navigation Technologies and European Workshop on GNSS Signals and Signal Processing (NAVITEC), 2010 5th ESA Workshop on*, pages 1–8. IEEE, 2010.

[35] Xinhua Tang, Gianluca Falco, Emanuela Falletti, and Letizia Lo Presti. Practical implementation and performance assessment of an extended Kalman filter-based signal tracking loop. In *Localization and GNSS (ICL-GNSS), 2013 International Conference on*, pages 1–6. IEEE, 2013.

[36] Nesreen I Ziedan. *GNSS receivers for weak signals*. Artech house, 2006.

[37] Mark L Psiaki and Hee Jung. Extended kalman filter methods for tracking weak GPS signals. In *ION GPS 2002: 15 th International Technical Meeting of the Satellite Division of The Institute of Navigation*, 2002.

[38] Ping Lian, Gérard Lachapelle, and ChangLin Ma. Improving tracking performance of PLL in high dynamics applications. In *ION NTM*, volume 1, pages 042–1, 2005.

[39] Kwang-Hoon Kim, Gyu-In Jee, and Jong-Hwa Song. Carrier tracking loop using the adaptive two-stage Kalman filter for high dynamic situations. *International Journal of Control Automation and Systems*, 6(6):948–953, 2008.

[40] Guo Yao, Wu Wenqi, and He Xiaofeng. High dynamic carrier phase tracking based on adaptive Kalman filtering. In *Control and Decision Conference (CCDC), 2011 Chinese*, pages 1245–1249. IEEE, 2011.

[41] Pedro A Roncagliolo, Cristian E De Blasis, and Carlos H Muravchik. GPS digital tracking loops design for high dynamic launching vehicles. In *Spread Spectrum Techniques and Applications, 2006 IEEE Ninth International Symposium on*, pages 41–45. IEEE, 2006.

[42] Pedro A Roncagliolo, Javier G Garcia, and Carlos H Muravchik. A joint carrier and data estimation scheme for real-time high dynamics GNSS receivers. In *Advanced satellite multimedia systems conference (asma) and the 11th signal processing for space communications workshop (spsc), 2010 5th*, pages 361–368. IEEE, 2010.

[43] S Han, W Wang, X Chen, and W Meng. Design and capability analyze of high dynamic carrier tracking loop based on UKF. In *Proceedings of the 23rd International Technical Meeting of The Satellite Division of the Institute of Navigation (ION GNSS 2010)*, pages 1960–1966, 2010.

[44] Nesreen I Ziedan and James L Garrison. Extended kalman filter-based tracking of weak GPS signals under high dynamic conditions. In *Proceedings of ION GNSS*, volume 2004, pages 20–31. Citeseer, 2004.

[45] Xinlong Wang, Xinchun Ji, Shaojun Feng, and Vincent Calmettes. A high-sensitivity GPS receiver carrier-tracking loop design for high-dynamic applications. *GPS Solutions*, 19(2):225–236, 2015.

[46] S Skone, G Lachapelle, D Yao, W Yu, and R Watson. Investigating the impact of ionospheric scintillation using a GPS software receiver. In *18th Int. Tech. Meeting of the Satellite Division of the US Institute of Navigation*, pages 1126–1137, 2005.

[47] Faisal A Khan, Andrew G Dempster, and Chris Rizos. Projected bandwidth loop-an alternative to adaptive bandwidth loops with reduced complexity. In *Position Location and Navigation Symposium (PLANS), 2010 IEEE/ION*, pages 1147–1153. IEEE, 2010.

[48] Mario Gómez Arias. *Adaptive Kalman Filter-Based Phase-Tracking in GNSS*. BSc thesis, Technische Universität München, 2010.

[49] Jong-Hoon Won and Bernd Eissfeller. A tuning method based on signal-to-noise power ratio for adaptive PLL and its relationship with equivalent noise bandwidth. *IEEE communications letters*, 17(2):393–396, 2013.

[50] Gerd Ascheid and Heinrich Meyr. Cycle slips in phase-locked loops: A tutorial survey. *Communications, IEEE Transactions on*, 30(10):2228–2241, 1982.

[51] James T Curran, Gérard Lachapelle, and Colin C Murphy. An SNR dependent model for the CDMA FLL. *IEEE Transactions on Signal Processing*, 60(3):1522–1527, 2012.

[52] Thomas Pany. *Navigation signal processing for GNSS software receivers*. Artech House, 2010.

[53] Zhe He. *High-Sensitivity GNSS Doppler and Velocity Estimation for Indoor Navigation*. PhD thesis, University of Calgary, 2013.

[54] Daniele Borio, Laura Camoriano, Letizia Lo Presti, and Maurizio Fantino. DTFT-based frequency lock loop for GNSS applications. *IEEE transactions on aerospace and electronic systems*, 44(2):595–612, 2008.

[55] Jong-Hoon Won, Thomas Pany, and Bernd Eissfeller. Iterative maximum likelihood estimators for high-dynamic GNSS signal tracking. *Aerospace and Electronic Systems, IEEE Transactions on*, 48(4):2875–2893, 2012.

[56] S Hinedi. An extended Kalman filter based automatic frequency control loop. 1988.

[57] Victor A Vilnrotter, Sami Hinedi, and Rajendra Kumar. Frequency estimation techniques for high dynamic trajectories. *Aerospace and Electronic Systems, IEEE Transactions on*, 25(4):559–577, 1989.

[58] Jong-Hoon Won, Thomas Pany, and Bernd Eissfeller. Noniterative filter-based maximum likelihood estimators for GNSS signal tracking. *Aerospace and Electronic Systems, IEEE Transactions on*, 48(2):1100–1114, 2012.

[59] Pedro A Roncagliolo and Javier G Garcia. High dynamics and false lock resistant GNSS carrier tracking loops. In *Proceedings of The 20th International Technical Meeting of The Satellite Division of The Institute of Navigation, ION GNSS 2007*, 2007.

[60] Jyh-Ching Juang and Yu-Hsuan Chen. Phase/frequency tracking in a GNSS software receiver. *Selected Topics in Signal Processing, IEEE Journal of*, 3(4):651–660, 2009.

[61] Pejman L Kazemi, Cillian ODriscoll, and Gérard Lachapelle. Digital phase locked loop with frequency rate feedback. In *Proc. ION GNSS*, pages 201–208, 2009.

[62] Pedro A Roncagliolo, Javier G García, and Carlos H Muravchik. Optimized carrier tracking loop design for real-time high-dynamics GNSS receivers. *International Journal of Navigation and Observation*, 2012, 2012.

[63] James J Spilker. Fundamentals of signal tracking theory. *Progress in Astronautics and Aeronautics*, 163:245–328, 1996.

[64] Patrick Henkel, Kaspar Giger, and Christoph Günther. Multifrequency, multisatellite vector phase-locked loop for robust carrier tracking. *Selected Topics in Signal Processing, IEEE Journal of*, 3(4):674–681, 2009.

[65] Stefan Kiesel, Christian Ascher, Daniel Gramm, and Gert F Trommer. GNSS receiver with vector based FLL-assisted PLL carrier tracking loop. *ION GNSS 2008, Proceedings of the Institute of Navigation*, pages 197–203, 2008.

[66] Thomas Pany, Roland Kaniuth, and Bernd Eissfeller. Deep integration of navigation solution and signal processing. In *Proceedings of the 18th International Technical Meeting of the Satellite Division of The Institute of Navigation (ION GNSS 2005)*, pages 1095–1102, 2001.

[67] Thomas Pany and Bernd Eissfeller. Use of a vector delay lock loop receiver for GNSS signal power analysis in bad signal conditions. *Proceedings of IEEE/ION PLANS*, pages 893–903, 2006.

[68] Tao Lin, Cillian ODriscoll, and Gérard Lachapelle. Development of a context-aware vector-based high-sensitivity GNSS software receiver. *Proc. ION ITM*, pages 1043–1055, 2011.

[69] Andrey Soloviev, Frank van Graas, and Sanjeev Gunawardena. Implementation of deeply integrated gps/low-cost imu for reacquisition and tracking of low cnr gps signals. In *Proceedings of the 2004 National Technical Meeting of The Institute of Navigation*, pages 923–935, 2001.

[70] Matthew Lashley and David M Bevly. Analysis of discriminator based vector tracking algorithms. In *Proceedings of the National Technical Meeting of the Institute of Navigation*, pages 570–576, 2007.

[71] M Lashley and DM Bevly. Comparison of traditional tracking loops and vector based loops for weak GPS signals. In *Proceedings of National Techical Meeting ION, San Diego, CA*, page 98, 2008.

[72] Matthew Lashley. *Modeling and performance analysis of GPS vector tracking algorithms*. PhD thesis, Auburn University, 2009.

[73] Matthew Lashley and David M Bevly. Vector delay/frequency lock loop implementation and analysis. *Proceedings of the Institute of Navigation*, 2009.

[74] Matthew Lashley, David M Bevly, and John Y Hung. Performance analysis of vector tracking algorithms for weak GPS signals in high dynamics. *Selected Topics in Signal Processing, IEEE Journal of*, 3(4):661–673, 2009.

[75] Mattew Lashley, David M Bevly, et al. What are vector tracking loops, and what are their benefits and drawbacks? *GNSS Solutions Column, Inside GNSS*, 4(3):16–21, 2009.

[76] Matthew Lashley, David M Bevly, and John Y Hung. A valid comparison of vector and scalar tracking loops. In *Position Location and Navigation Symposium (PLANS), 2010 IEEE/ION*, pages 464–474. IEEE, 2010.

[77] Matthew Lashley and David M Bevly. Comparison in the performance of the vector delay/frequency lock loop and equivalent scalar tracking loops in dense foliage and urban canyon. In *Proceedings of the 24th International Technical Meeting of The Satellite Division of the Institute of Navigation (ION GNSS 2011)*, page 1786, 2011.

[78] Jong-Hoon Won and Bernd Eissfeller. Effectiveness analysis of vector-tracking-loop in signal fading environment. In *Satellite Navigation Technologies and European Workshop on GNSS Signals and Signal Processing (NAVITEC), 2010 5th ESA Workshop on*, pages 1–6. IEEE, 2010.

[79] Kwang-Hoon Kim, Gyu-In Jee, and Sung-Hyuck Im. Adaptive vector-tracking loop for low-quality GPS signals. *International Journal of Control, Automation and Systems*, 9(4):709–715, 2011.

[80] Susmita Bhattacharyya and Demoz Gebre-Egziabher. Development and validation of parametric models for vector tracking loops. *Navigation*, 57(4):275–295, 2010.

[81] Susmita Bhattacharyya and Demoz Gebre-Egziabher. Vector loop RAIM in nominal and GNSS-stressed environments. *Aerospace and Electronic Systems, IEEE Transactions on*, 50(2):1249–1268, 2014.

[82] Susmita Bhattacharyya and Demoz Gebre-Egziabher. Integrity monitoring with vector GNSS receivers. *Aerospace and Electronic Systems, IEEE Transactions on*, 50(4):2779–2793, 2014.

[83] Yang Wang, Rong Yang, Keck Voon Ling, and Eng Kee Poh. Robust vector tracking loop using moving horizon estimation. In *Pacific PNT*, Honolulu, Hawaii, USA, April 2015. ION.

[84] Katsuhiko Ogata and Yanjuan Yang. *Modern control engineering*. Prentice-Hall Englewood Cliffs, 1970.

[85] AK Steiner and G Kirchengast. Error analysis for GNSS radio occultation data based on ensembles of profiles from end-to-end simulations. *Journal of Geophysical Research: Atmospheres*, 110(D15), 2005.

[86] S Sokolovskiy, Y-H Kuo, C Rocken, WS Schreiner, D Hunt, and RA Anthes. Monitoring the atmospheric boundary layer by GPS radio occultation signals recorded in the open-loop mode. *Geophysical research letters*, 33(12), 2006.

[87] CO Ao, GA Hajj, TK Meehan, D Dong, BA Iijima, AJ Mannucci, and ER Kursinski. Rising and setting GPS occultations by use of open-loop tracking. *Journal of Geophysical Research: Atmospheres*, 114(D4), 2009.

[88] E Cardellach, F Fabra, O Nogués-Correig, S Oliveras, S Ribó, and A Rius. GNSS-R ground-based and airborne campaigns for ocean, land, ice, and snow techniques: Application to the GOLD-RTR data sets. *Radio Science*, 46(6), 2011.

[89] Frank van Graas, Andrey Soloviev, Maarten Uijt de Haag, Sandjeev Gunawardena, and Michael Braasch. Comparison of two approaches for GNSS receiver algorithms: batch processing and sequential processing considerations. In *Proceedings of the 18th International Technical Meeting of the Satellite Division of The Institute of Navigation (ION GNSS 2005), Long Beach*, pages 200–211, 2005.

[90] Frank Van Graas, Andrey Soloviev, De Haag, Maarten Uijt, and Sanjeev Gunawardena. Closed-loop sequential signal processing and open-loop batch processing approaches for GNSS receiver design. *Selected Topics in Signal Processing, IEEE Journal of*, 3(4):571–586, 2009.

[91] Esther Anyaegbu. A frequency domain quasi-open loop tracking loop for GNSS receivers. In *Proceedings of the 19th International Technical Meeting of the Satellite Division of The Institute of Navigation (ION GNSS 2006)*, pages 790–798, 2006.

[92] Muhammad Tahir, Letizia Lo Presti, and Maurizio Fantino. A novel quasi open loop frequency estimator for GNSS signal tracking. In *Position Location and Navigation Symposium (PLANS), 2012 IEEE/ION*, pages 952–960. IEEE, 2012.

[93] Georges Stienne, Serge Reboul, Jean-Bernard Choquel, and Mohammed Benjelloun. Circular data processing tools applied to a phase open loop architecture for multi-channels signals tracking. In *Position Location and Navigation Symposium (PLANS), 2012 IEEE/ION*, pages 633–642. IEEE, 2012.

[94] Georges Stienne, Serge Reboul, Monir Azmani, Jean-Bernard Choquel, and Mohammed Benjelloun. GNSS dataless signal tracking with a delay semi-open loop and a phase open loop. *Signal Processing*, 93(5):1192–1209, 2013.

[95] Kunlun Yan, Nesreen I Ziedan, Hongping Zhang, Wenfei Guo, Xiaoji Niu, and Jingnan Liu. Weak GPS signal tracking using FFT discriminator in open loop receiver. *GPS Solutions*, pages 1–13, 2014.

[96] Muhammad Tahir, Letizia Lo Presti, and Maurizio Fantino. Characterizing different open loop fine frequency estimation methods for gnss receivers. 2012.

[97] Katsuhiko Ogata. *Discrete-time control systems*, volume 2. Prentice Hall Englewood Cliffs, NJ, 1995.

[98] KV Ling and KW Lim. Receding horizon recursive state estimation. *Automatic Control, IEEE Transactions on*, 44(9):1750–1753, 1999.

[99] Mark L Psiaki and Hee Jung. Extended Kalman filter methods for tracking weak GPS signals. In *Proceedings of the 15th International Technical Meeting of the Satellite Division of The Institute of Navigation (ION GPS 2002)*, pages 2539–2553, 2002.

[100] Yaakov Bar-Shalom, X Rong Li, and Thiagalingam Kirubarajan. *Estimation with applications to tracking and navigation: theory algorithms and software*. John Wiley and Sons Ltd, 2004.

[101] RJ Landry and A Renard. Analysis of potential interference sources and assessment of present solutions for GPS/GNSS receivers. *4th Saint-Petersburg on INS*, pages 1–13, 1997.

[102] Yu Jiao, Yu T Morton, Steven Taylor, and Wouter Pelgrum. Characterization of high-latitude ionospheric scintillation of GPS signals. *Radio Science*, 48(6):698–708, 2013.

[103] Mark G Petovello, Kyle OKeefe, Gérard Lachapelle, and M Elizabeth Cannon. Consideration of time-correlated errors in a Kalman filter applicable to GNSS. *Journal of Geodesy*, 83(1):51–56, 2009.

[104] Mohammad S Sharawi, Dennis M Akos, and Daniel N Aloi. GPS C/N_0 estimation in the presence of interference and limited quantization levels. *Aerospace and Electronic Systems, IEEE Transactions on*, 43(1):227–238, 2007.

[105] Emanuela Falletti, Marco Pin, and Letizia Lo Presti. Low complexity carrier-to-noise ratio estimators for GNSS digital receivers. *Aerospace and Electronic Systems, IEEE Transactions on*, 47(1):420–437, 2011.

[106] Shashank Satyanarayana, Daniele Borio, and Gérard Lachapelle. C/N_0 estimation: design criteria and reliability analysis under global navigation satellite system (GNSS) weak signal scenarios. *IET Radar, Sonar & Navigation*, 6(2):81–89, 2012.

[107] Ara Patapoutian. On phase-locked loops and Kalman filters. *Communications, IEEE Transactions on*, 47(5):670–672, 1999.

Appendix A

Wiener filter transfer function derivation

For the 2-state model, the z transformation of the auto-correlation function of the input signal $\bar{\theta}_k$ can be expressed as

$$S_{\bar{\theta}2}(z) = \frac{\frac{T^2}{4} z(z+1)^2 \sigma_\omega^2 - 4z(z-1)^2 \sigma_\varphi^2}{(z-1)^4}. \tag{A.1}$$

From equation (3.13), we obtain

$$S_\theta(z) = S_{\bar{\theta}}(z) + \sigma_v^2. \tag{A.2}$$

Using spectral factorization [107],

$$S_\theta(z) = Y(z) Y\left(z^{-1}\right) \tag{A.3}$$

We obtain:

$$Y_2(z) = \sigma_v \frac{(z-z_0)(z-z_1)}{(z-1)^2}. \tag{A.4}$$

Since z_0 and z_1 should be real numbers or complex conjugates, they have to take the following values:

$$z_i = \frac{\left(\gamma_i - \sqrt{\gamma_i^2 - 4}\right)}{2}, i = 0, 1 \tag{A.5}$$

where

$$\gamma_i = 2 + \left(\frac{\sigma_a^2}{2}\right) + (-1)^i \sqrt{\left(\frac{\sigma_a^2}{2}\right)^2 - \sigma_b^2}, i = 0, 1 \tag{A.6}$$

and

$$\begin{cases} \sigma_a^2 = \dfrac{\sigma_\varphi^2}{\sigma_v^2} - \dfrac{T^2}{4}\dfrac{\sigma_\omega^2}{\sigma_v^2} \\ \sigma_b^2 = T^2 \dfrac{\sigma_\omega^2}{\sigma_v^2}. \end{cases} \tag{A.7}$$

Then, we could obtain the 2-state WF transfer function

$$H_{WF2}(z) = \frac{\left[\frac{S_{\tilde{\theta}2}(z)}{Y_2(z^{-1})}\right]_+}{Y_2(z)} = 1 - \frac{\sigma_v}{Y_2(z)} = \frac{(2 - z_0 - z_1)z + z_0 z_1 - 1}{z^2 - (z_0 + z_1)z + z_0 z_1}. \tag{A.8}$$

Similarly, z transformation of the auto-correlation functions of input signal θ_k for 3-state model can be written as

$$S_{\theta 3}(z) = \sigma_v^2 \frac{\left(\begin{array}{l} z^6 - \left(6 + \frac{T^2}{3}\frac{\sigma_{\dot{\omega}\varphi}^2}{\sigma_v^2} + \frac{T^4}{36}\frac{\sigma_{\dot{\omega}}^2}{\sigma_v^2} + \frac{\sigma_\varphi^2}{\sigma_v^2} - \frac{T^2}{4}\frac{\sigma_\omega^2}{\sigma_v^2}\right) z^5 + \left(15 + 4\frac{\sigma_\varphi^2}{\sigma_v^2} - \frac{2T^4}{9}\frac{\sigma_{\dot{\omega}}^2}{\sigma_v^2} - \frac{2T^2}{3}\frac{\sigma_{\dot{\omega}\varphi}^2}{\sigma_v^2}\right) z^4 \\ - \left(20 + 6\frac{\sigma_\varphi^2}{\sigma_v^2} + \frac{T^4}{2}\frac{\sigma_{\dot{\omega}}^2}{\sigma_v^2} + \frac{T^2}{2}\frac{\sigma_\omega^2}{\sigma_v^2} - 2T^2\frac{\sigma_{\dot{\omega}\varphi}^2}{\sigma_v^2}\right) z^3 + \left(15 + 4\frac{\sigma_\varphi^2}{\sigma_v^2} - \frac{2T^4}{9}\frac{\sigma_{\dot{\omega}}^2}{\sigma_v^2} - \frac{2T^2}{3}\frac{\sigma_{\dot{\omega}\varphi}^2}{\sigma_v^2}\right) z^2 + \\ - \left(6 + \frac{T^2}{3}\frac{\sigma_{\dot{\omega}\varphi}^2}{\sigma_v^2} + \frac{T^4}{36}\frac{\sigma_{\dot{\omega}}^2}{\sigma_v^2} + \frac{\sigma_\varphi^2}{\sigma_v^2} - \frac{T^2}{4}\frac{\sigma_\omega^2}{\sigma_v^2}\right) z + 1 \end{array} \right)}{(z-1)^6}. \tag{A.9}$$

According to equation (A.3), S_θ should be expressed as the following form

$$S_\theta(z) = \sigma_v^2 \frac{(z - z_0)(z - z_1)(z - z_2)\left(z - \frac{1}{z_0}\right)\left(z - \frac{1}{z_1}\right)\left(z - \frac{1}{z_2}\right)}{(z-1)^6}. \tag{A.10}$$

Thus, $Y(z)$ can be written as

$$Y(z) = \sigma_v \frac{(z - z_0)(z - z_1)(z - z_2)}{(z-1)^3}. \tag{A.11}$$

Expanding equation (A.10), we obtain

$$S_\theta(z) = \sigma_v^2 \frac{\left\{ \begin{array}{l} \left(z^2 - \left(z_0 + \frac{1}{z_0}\right) z + 1\right) \cdot \left(z^2 - \left(z_1 + \frac{1}{z_1}\right) z + 1\right) \\ \cdot \left(z^2 - \left(z_2 + \frac{1}{z_2}\right) z + 1\right) \end{array} \right\}}{(z-1)^6}. \tag{A.12}$$

Denoting r_0, r_1 and r_2 as

$$\begin{cases} r_0 = \left(z_0 + \dfrac{1}{z_0}\right) \\ r_1 = \left(z_1 + \dfrac{1}{z_1}\right) \\ r_2 = \left(z_2 + \dfrac{1}{z_2}\right) \end{cases} \tag{A.13}$$

and by solving the quadratic equation, the roots of S_θ can be obtained as

$$z_i = \frac{r_i \pm \sqrt{{r_i}^2 - 4}}{2}, i \in \{0, 1, 2\}. \tag{A.14}$$

Among these 6 roots, only three of them are located inside the unit circle and the rest are located outside the unit circle. Their locations depend on r_i and r_i and can be solved by the following steps.

First, we substitute r_i into S_θ to obtain:

$$\begin{aligned} S_\theta(z) &= \sigma_v^2 \frac{(z^2 - r_0 z + 1)(z^2 - r_1 z + 1)(z^2 - r_2 z + 1)}{(z-1)^6} \\ &= \sigma_v^2 \frac{\left\{ \begin{array}{l} z^6 - (r_0 + r_1 + r_2) z^5 + (r_0 r_1 + r_1 r_2 + r_0 r_2 + 3) z^4 \\ - (r_0 r_1 r_2 + 2(r_0 + r_1 + r_2)) z^3 \\ + (r_0 r_1 + r_1 r_2 + r_0 r_2 + 3) z^2 - (r_0 + r_1 + r_2) z + 1 \end{array} \right\}}{(z-1)^6}. \end{aligned} \tag{A.15}$$

Then, by comparing the above equation to equation (A.9), we have

$$\begin{cases} r_0 + r_1 + r_2 = 6 + \dfrac{T^2}{3}\dfrac{\sigma_{\dot\omega\varphi}^2}{\sigma_v^2} + \dfrac{T^4}{36}\dfrac{\sigma_{\dot\omega}^2}{\sigma_v^2} + \dfrac{\sigma_\varphi^2}{\sigma_v^2} - \dfrac{T^2}{4}\dfrac{\sigma_\omega^2}{\sigma_v^2} \\ r_0 r_1 + r_1 r_2 + r_0 r = 12 + 4\dfrac{\sigma_\varphi^2}{\sigma_v^2} - \dfrac{2T^4}{9}\dfrac{\sigma_{\dot\omega}^2}{\sigma_v^2} - \dfrac{2T^2}{3}\dfrac{\sigma_{\dot\omega\varphi}^2}{\sigma_v^2} \\ r_0 r_1 r_2 = 8 + 4\dfrac{\sigma_\varphi^2}{\sigma_v^2} + \dfrac{4T^4}{9}\dfrac{\sigma_{\dot\omega}^2}{\sigma_v^2} + T^2\dfrac{\sigma_\omega^2}{\sigma_v^2} - \dfrac{8T^2}{3}\dfrac{\sigma_{\dot\omega\varphi}^2}{\sigma_v^2}. \end{cases} \tag{A.16}$$

The above three equations indicate that r_0, r_1 and r_2 are the three roots of $(z+r_0)(z+r_1)(z+r_2)=0$. To solve this cubic equation the Cardano's Formula is applied and r_i can be expressed in the following forms

$$r_0 = 2 + x + \sqrt[3]{y+\sqrt{y^2+m^3}} + \sqrt[3]{y-\sqrt{y^2+m^3}} \tag{A.17}$$

$$r_1 = 2 + x + \frac{-1+\sqrt{3}j}{2}\sqrt[3]{y+\sqrt{y^2+m^3}} + \frac{-1-\sqrt{3}j}{2}\sqrt[3]{y-\sqrt{y^2+m^3}} \tag{A.18}$$

$$r_2 = 2 + x + \frac{-1-\sqrt{3}j}{2}\sqrt[3]{y+\sqrt{y^2+m^3}} + \frac{-1+\sqrt{3}j}{2}\sqrt[3]{y-\sqrt{y^2+m^3}}. \tag{A.19}$$

Then we have

$$\begin{cases} r_0+r_1+r_2 = 6+3x \\ r_0r_1+r_1r_2+r_0r_2 = 12+12x+3x^2+3m \\ r_0r_1r_2 = 8+12x+2y+6x^2+x^3+3xm+6m. \end{cases} \tag{A.20}$$

Comparing equation (A.20) to equation (A.16), x, y and m can be determined as below

$$\begin{cases} x = d/3 \\ y = 2d + \frac{1}{27}d^3 - f + \frac{2}{3}d^2 - \frac{1}{6}df + \frac{1}{2}g \\ m = (3f - 12d - d^2)/9 \end{cases} \tag{A.21}$$

with

$$\begin{cases} d = \frac{T^2}{3}\frac{\sigma^2_{\dot{\omega}\varphi}}{\sigma^2_v} + \frac{T^4}{36}\frac{\sigma^2_{\dot{\omega}}}{\sigma^2_v} + \frac{\sigma^2_\varphi}{\sigma^2_v} - \frac{T^2}{4}\frac{\sigma^2_\omega}{\sigma^2_v} \\ g = 4\frac{\sigma^2_\varphi}{\sigma^2_v} + \frac{4T^4}{9}\frac{\sigma^2_{\dot{\omega}}}{\sigma^2_v} + T^2\frac{\sigma^2_\omega}{\sigma^2_v} - \frac{8T^2}{3}\frac{\sigma^2_{\dot{\omega}\varphi}}{\sigma^2_v} \\ f = 4\frac{\sigma^2_\varphi}{\sigma^2_v} - \frac{2T^4}{9}\frac{\sigma^2_{\dot{\omega}}}{\sigma^2_v} - \frac{2T^2}{3}\frac{\sigma^2_{\dot{\omega}\varphi}}{\sigma^2_v}. \end{cases} \tag{A.22}$$

Finally, z_0, z_1 and z_2 are solved and can be written as

$$z_i = \frac{r_i \pm \sqrt{r_i^2-4}}{2}, i = 0,1,2 \tag{A.23}$$

Equation (A.23) has 6 roots due to the additional parameter q_a's effect on the roots' locations. Among the 6 roots, only three of them are located inside the unit circle and the rest are located outside circle. To keep the loop stable, z_0, z_1 and z_2 should be the roots

inside or on the unit circle.

Then, we could obtain the 3-state WF transfer function

$$\begin{aligned} H_{WF3}(z) &= \frac{\left[\frac{S_{\bar{\theta}3}(z)}{Y_3(z^{-1})}\right]_+}{Y_3(z)} \\ &= 1 - \frac{\sigma_v}{Y_3(z)} \\ &= \frac{(3 - z_0 - z_1 - z_2)\, z^2 + (z_0 z_1 + z_0 z_2 + z_1 z_2 - 3)\, z + 1 - z_0 z_1 z_2}{z^3 + (-z_0 - z_1 - z_2)\, z^2 + (z_0 z_1 + z_0 z_2 + z_1 z_2)\, z - z_0 z_1 z_2}. \end{aligned} \tag{A.24}$$

Appendix B

Frequency Measurement Derivation

According to equations (3.14) and (3.17) ,

$$\begin{aligned}\Delta\theta_{k+1} - \Delta\theta_k &= \frac{T}{2}\Delta\omega_{k+1} + \Delta\varphi_{k+1} + v_{k+1} - \frac{T}{2}\Delta\omega_k - \Delta\varphi_k - v_k \\ &= \frac{T}{2}\Delta\omega_{k+1} + T\Delta\omega_k + \Delta\varphi_k + v_{k+1} - \frac{T}{2}\Delta\omega_k - \Delta\varphi_k - v_k \\ &= \frac{T}{2}\left(\Delta\omega_{k+1} + \Delta\omega_k\right) + v_{k+1} - v_k\end{aligned} \tag{B.1}$$

Assuming that the frequency error will not change by a significant amount over one sample period, we have

$$\Delta\theta_{k+1} - \Delta\theta_k \approx T\Delta\omega_{k+1} + v_{k+1} - v_k \tag{B.2}$$

Similarly, according to equations (3.15) and (3.17),

$$\begin{aligned}\Delta\theta_{k+1} - \Delta\theta_k &= \frac{T^2}{6}\Delta\dot{\omega}_{k+1} + \frac{T}{2}\Delta\omega_{k+1} + \Delta\varphi_{k+1} + v_{k+1} - \frac{T^2}{6}\Delta\dot{\omega}_k - \frac{T}{2}\Delta\omega_k - \Delta\varphi_k - v_k \\ &= \frac{T^2}{6}\Delta\dot{\omega}_{k+1} + \frac{T}{2}\Delta\omega_{k+1} + \frac{T^2}{2}\Delta\dot{\omega}_k + T\Delta\omega_k + \Delta\varphi_k + v_{k+1} \\ &\quad - \frac{T^2}{6}\Delta\dot{\omega}_k - \frac{T}{2}\Delta\omega_k - \Delta\varphi_k - v_k \\ &= \left(\frac{T^2}{6}\Delta\dot{\omega}_{k+1} + \frac{T^2}{2}\Delta\dot{\omega}_k - \frac{T^2}{6}\Delta\dot{\omega}_k\right) + \frac{T}{2}\left(\Delta\omega_{k+1} + \Delta\omega_k\right) + v_{k+1} - v_k\end{aligned} \tag{B.3}$$

Again, assuming that the frequency error and frequency rate error will not change by a significant amount over one sample period, we have

$$\Delta\theta_{k+1} - \Delta\theta_k \approx \frac{T^2}{2}\Delta\dot{\omega}_{k+1} + T\Delta\omega_{k+1} + v_{k+1} - v_k \tag{B.4}$$

Appendix C

Frequency Tracking Error Covariance Matrix Derivation

Substituting the received and local generated signal in equations (4.1), (4.12) and (4.18) into the equation (4.29), we have

$$\begin{aligned}
\mathbf{P}_{k+1} &= E\left[\left(\mathbf{x}_{k+1}-\hat{\mathbf{x}}_{k+1}\right)\left(\mathbf{x}_{k+1}-\hat{\mathbf{x}}_{k+1}\right)^{\mathrm{T}}\right] \\
&= E\left[\left(\mathbf{A}_F\mathbf{x}_k+\mathbf{n}_k-\mathbf{A}_F\hat{\mathbf{x}}_k-\mathbf{A}_F\mathbf{L}\Delta\varpi_k\right)\left(\mathbf{A}_F\mathbf{x}_k+\mathbf{n}_k-\mathbf{A}_F\hat{\mathbf{x}}_k-\mathbf{A}_F\mathbf{L}\Delta\varpi_k\right)^{\mathrm{T}}\right] \\
&= E\begin{bmatrix} \left(\mathbf{A}_F\Delta\mathbf{x}_k+\mathbf{n}_k-\mathbf{A}_F\mathbf{L}\left(\mathbf{H}_F\Delta\mathbf{x}_k+u_k\right)\right) \\ \left(\mathbf{A}_F\Delta\mathbf{x}_k+\mathbf{n}_k-\mathbf{A}_F\mathbf{L}\left(\mathbf{H}_F\Delta\mathbf{x}_k+u_k\right)\right)^{\mathrm{T}} \end{bmatrix} \\
&= \mathbf{A}_F\left(\mathbf{I}-\mathbf{L}\mathbf{H}_F\right)E\left[\Delta\mathbf{x}_k\Delta\mathbf{x}_k{}^{\mathrm{T}}\right]\left(\mathbf{I}-\mathbf{L}\mathbf{H}_F\right)^{\mathrm{T}}\mathbf{A}_F^{\mathrm{T}}+2\mathbf{A}_F\mathbf{L}(\mathbf{A}_F\mathbf{L})^{\mathrm{T}}\frac{\sigma_v^2}{T^2} \\
&+ \mathbf{Q}_F-\mathbf{A}_F\left(\mathbf{I}-\mathbf{L}\mathbf{H}_F\right)E\left[\Delta\mathbf{x}_k u_k{}^{\mathrm{T}}\right]\left(\mathbf{A}_F\mathbf{L}\right)^{\mathrm{T}}-\mathbf{A}_F\mathbf{L}E\left[u_k\Delta\mathbf{x}_k{}^{\mathrm{T}}\right]\left(\mathbf{I}-\mathbf{L}\mathbf{H}_F\right)^{\mathrm{T}}\mathbf{A}_F^{\mathrm{T}}
\end{aligned} \tag{C.1}$$

Let $\mathbf{G}_k$ represents the correlation between the error state and non-white measurement noise, we have $\mathbf{G}_k = E\left[\Delta\mathbf{x}_k u_k{}^{\mathrm{T}}\right]$ and $\mathbf{G}_k^T = E\left[u_k\Delta\mathbf{x}_k{}^{\mathrm{T}}\right]$. When k approaches infinity,

$\mathbf{G}_{k+1} = \mathbf{G}_k = \mathbf{G}_Y$ is in steady state. We expand $\mathbf{G}_Y$ as following steps

$$\begin{aligned}
\mathbf{G}_Y &= E\left[\Delta\mathbf{x}_k {u_k}^{\mathrm{T}}\right] \\
&= E\left[-(\mathbf{A}_F\hat{\mathbf{x}}_{k-1} + \mathbf{A}_F\mathbf{L}\Delta\varpi_{k-1})\,\frac{(v_k - v_{k-1})^{\mathrm{T}}}{T}\right] \\
&= E\left[-\mathbf{A}_F\mathbf{L}\frac{(v_{k-1} - v_{k-2})}{T}\,\frac{(v_k - v_{k-1})^{\mathrm{T}}}{T}\right] \\
&= \mathbf{A}_F\mathbf{L}\frac{\sigma_v^2}{T^2}
\end{aligned} \tag{C.2}$$

Finally, we can obtain

$$\begin{aligned}
\mathbf{P}_Y &= \mathbf{A}_F\left(\mathbf{I} - \mathbf{L}\mathbf{H}_F\right)\mathbf{P}_Y(\mathbf{I} - \mathbf{L}\mathbf{H}_F)^{\mathrm{T}}\mathbf{A}_F^{\mathrm{T}} + \mathbf{Q}_F + 2\mathbf{A}_F\mathbf{L}(\mathbf{A}_F\mathbf{L})^{\mathrm{T}}\frac{\sigma_v^2}{T^2} \\
&\quad + \mathbf{A}_F\left(\mathbf{I} - \mathbf{L}\mathbf{H}_F\right)\mathbf{G}_Y(\mathbf{A}_F\mathbf{L})^{\mathrm{T}} + \mathbf{A}_F\mathbf{L}\mathbf{G}_Y^{\mathrm{T}}(\mathbf{I} - \mathbf{L}\mathbf{H}_F)^{\mathrm{T}}\mathbf{A}_F^{\mathrm{T}} \\
&= \mathbf{A}_F\left(\mathbf{I} - \mathbf{L}\mathbf{H}_F\right)\mathbf{P}_Y(\mathbf{I} - \mathbf{L}\mathbf{H}_F)^{\mathrm{T}}\mathbf{A}_F^{\mathrm{T}} + \mathbf{Q}_F + 2\mathbf{A}_F\mathbf{L}(\mathbf{A}_F\mathbf{L})^{\mathrm{T}}\frac{\sigma_v^2}{T^2} \\
&\quad - \mathbf{A}_F\left(\mathbf{I} - \mathbf{L}\mathbf{H}_F\right)\mathbf{A}\mathbf{L}(\mathbf{A}_F\mathbf{L})^{\mathrm{T}}\frac{\sigma_v^2}{T^2} - \mathbf{A}_F\mathbf{L}(\mathbf{A}_F\mathbf{L})^{\mathrm{T}}(\mathbf{I} - \mathbf{L}\mathbf{H}_F)^{\mathrm{T}}\mathbf{A}_F^{\mathrm{T}}\frac{\sigma_v^2}{T^2}
\end{aligned} \tag{C.3}$$

Appendix D

Optimal solution of 1-state frequency tracking loop

To solve the quartic equation $\alpha^4 - 4\alpha^3 - b\alpha + b = 0$, we denote $\alpha = x + 1$ to eliminate the term α^3 in this quartic equation and then we have

$$x^4 + 6x^2 - (b+8)x - 3 = 0. \tag{D.1}$$

Applying the Ferrari's solution, the four solutions of the above equation can be obtained as

$$x_1 = \frac{1}{2}\sqrt{4 + \sqrt[3]{b^2+16b}} - \frac{1}{2}\sqrt{8 - \sqrt[3]{b^2+16b} + \frac{2b+16}{\sqrt{4+\sqrt[3]{b^2+16b}}}} \tag{D.2}$$

$$x_2 = \frac{1}{2}\sqrt{4 + \sqrt[3]{b^2+16b}} + \frac{1}{2}\sqrt{8 - \sqrt[3]{b^2+16b} + \frac{2b+16}{\sqrt{4+\sqrt[3]{b^2+16b}}}} \tag{D.3}$$

$$x_3 = -\frac{1}{2}\sqrt{4 + \sqrt[3]{b^2+16b}} - \frac{1}{2}\sqrt{8 - \sqrt[3]{b^2+16b} - \frac{2b+16}{\sqrt{4+\sqrt[3]{b^2+16b}}}} \tag{D.4}$$

$$x_4 = -\frac{1}{2}\sqrt{4 + \sqrt[3]{b^2+16b}} + \frac{1}{2}\sqrt{8 - \sqrt[3]{b^2+16b} - \frac{2b+16}{\sqrt{4+\sqrt[3]{b^2+16b}}}} \tag{D.5}$$

The corresponding solutions of α can be obtained through the relation $\alpha = x + 1$. It is noted that the tracking error variance $\mathbf{p}_{\bar{\omega}}$ should be always positive. The condition that

$0 < \alpha < 2$ should be satisfied. Hence, the optimal value of α that minimizes $\mathbf{p}_{\bar{\omega}}$ is

$$\alpha_{opt} = 1 + \frac{1}{2}\sqrt{4 + \sqrt[3]{b^2 + 16b}} - \frac{1}{2}\sqrt{8 - \sqrt[3]{b^2 + 16b} + \frac{2b + 16}{\sqrt{4 + \sqrt[3]{b^2 + 16b}}}}. \tag{D.6}$$